ALMA MATER STUDIORUM
UNIVERSITÀ DI BOLOGNA

DEPARTMENT OF PHYSICS AND ASTRONOMY "A. RIGHI"

SECOND CYCLE DEGREE

PHYSICS

Production of light anti-nuclei in high-energy pp and ep collisions: a coalescence-based approach

Supervisor
Prof. Francesca Bellini

Co-supervisor
Dott. Francesco Noferini

Defended by
Niccolò Ciavarelli

Graduation Session 03/2026

Academic Year 2024/2025

Abstract

This thesis presents a study of light (anti)nucleus production in high-energy collisions, focusing on the interplay between coalescence and nucleon–nucleon (N–N) interactions. The formation of loosely bound states such as (anti)deuterons and (anti)helium nuclei is a rare process that requires correlated (anti)nucleons in the final state. A consistent modelling of this process must therefore account for both bound-state formation and final-state interactions, which modify two-particle distributions and influence the probability of clustering.

A model is developed and coupled through an afterburner to the Monte Carlo event generator PYTHIA8 to simulate proton–proton and electron–proton collisions. Two complementary implementations of the coalescence mechanism are presented: a wave-function-based formalism and a Wigner-function approach, where in both cases the coalescence probability is computed. Within the same framework, N–N interactions are incorporated through a semiclassical energy-conservation prescription, and the model is extended iteratively to describe nuclei and antinuclei up to $A = 4$.

The model is applied to pp collisions at $\sqrt{s} = 13.6$ TeV, where transverse-momentum spectra and the coalescence parameters B_2 and B_3 are compared to ALICE measurements. A grid-based χ^2 minimisation is performed to constrain the source and deuteron size parameters. The result of the model is further compared to ZEUS data in ep collisions and used to provide predictions for the future Electron–Ion Collider, including yields and B_2 distributions within the ePIC dRICH acceptance.

Contents

List of Figures

List of Tables

Introduction

The formation mechanism of light nuclei and antinuclei in high-energy collisions is still not fully understood while it could offer insights to characterize nuclear matter under extreme conditions as well as to interpret potential dark-matter signals in indirect searches in cosmic ray. In hadronic interactions, (anti)nucleus production is strongly suppressed with respect to (anti)proton production, and the formation of a loosely-bound nuclear cluster requires specific final-state correlations among nucleons. For this reason, measurements of light (anti)nuclei at accelerators provide a unique benchmark for the microscopic formation mechanism, and are tightly connected to femtoscopic observables that probe the space–time structure of the emitting source. A quantitative description of these phenomena must simultaneously address two complementary aspects: nucleon–nucleon (N–N) interactions, which modify two-particle distributions without producing a bound state, and binding (modelled via coalescence), which instead converts correlated nucleon pairs into composite nuclei. Developing a model able to treat both effects consistently is therefore essential not only to reproduce single-particle yields, but also to interpret correlation functions and the depletion of low-k^* pairs induced by bound-state formation.

The goal of this thesis is to implement a model that can be coupled through an afterburner to an event generator (in this work PYTHIA8) and that treats the formation of bound states via coalescence and N–N interactions within a unified approach. The model is developed in two equivalent formalisms: a wave function–based description, where the coalescence probability is obtained from the scalar product between a Gaussian source wave function and the nuclear bound-state wave function, and a Wigner function formalism, where both the source and the bound state are described in phase space and the coalescence probability is computed through their overlap. Within the same framework, N–N interactions are implemented through a semiclassical energy-conservation treatment. The model is then extended iteratively to form nuclei and antinuclei up to $A = 4$, including the treatment of photon emission associated with the transition from the initial two-body system to the final bound state.

After establishing the model, its applications are presented for proton–proton (pp) and electron–proton (ep) collisions in configurations relevant for the Large Hadron Collider (LHC), Hadron-Electron Ring Accelerator (HERA), and the future Electron–Ion Collider (EIC). In pp collisions at $\sqrt{s} = 13.6$ TeV, transverse-momentum spectra of $\overline{p}$, $\overline{D}$, $\overline{T}$, $^{3}\overline{\mathrm{He}}$, and $^{4}\overline{\mathrm{He}}$ are compared to ALICE measurements, and the coalescence parameters B_2 and B_3 are extracted. In addition, the associated photon production from (anti)deuteron formation is investigated, highlighting how γ–$\bar{d}$ kinematics can be exploited to reconstruct the pre-coalescence $\bar{p}$–$\bar{n}$ relative-momentum distribution. Finally, the interplay between coalescence and final-state interactions is studied through two-particle correlation functions $C(k^*)$, quantifying the suppression of low-k^* nucleon pairs when coalescence is enabled and discussing its implications for correlation measurements involving light nuclei.

In ep collisions, the framework is first tested against ZEUS results at $\sqrt{s} = 318$ GeV through the comparison of simulated B_2 distributions for D and $\overline{D}$. Building on this validation, predictions are provided for the EIC configuration, including pseudorapidity-dependent yields of deuterons and antideuterons and the corresponding B_2 distributions within the acceptance of the future ePIC dual RICH (dRICH) detector for different photon-virtuality selections. In this way, the present work establishes a coherent description of light-(anti)nucleus formation across different collision systems and kinematic regimes, providing a quantitative link between coalescence, nucleon correlations, and experimental observables.

Chapter 1

Light (anti)Nuclei Production Models

The experimental discovery of antimatter and Antinuclei produced in proton–nucleus collision experiments established that bound systems of antinucleons can be formed under suitable conditions. Today, light nuclei and antinuclei produced in high-energy collisions are considered probes of weakly bound objects emerging from a source, making their production sensitive to nucleon correlations and to the space–time extent of the emission region.

This chapter first provides a historical overview of the fundamental milestones in antimatter and antinuclei research. It then introduces the strong interaction and nucleon–nucleon potentials, which form the theoretical backbone of the production models presented thereafter. The production of (anti)nuclei in high-energy interactions is discussed within the frameworks of statistical hadronisation and coalescence approaches, with particular emphasis on the coalescence picture and its dependence on the source size. Finally, the femtoscopic determination of the nucleon source is outlined, illustrating how two-particle correlations constrain the emission region relevant for bound-state formation.

1.1 Historical overview

The existence of antimatter has been established since the 1930s, although its possibility had been discussed for more than three decades prior to its experimental discovery. The term *antimatter* was introduced in 1898 by Arthur Schuster in a letter to *Nature* [1], where he speculated about a hypothetical form of matter characterized by negative gravitational interaction and capable of annihilating ordinary matter. Schuster's ideas reflected the scientific context of the time, when classical electrodynamics and statistical mechanics dominated the theoretical description of physical phenomena, and questions about gravitational effects at the atomic scale were actively debated.

The modern theoretical foundation of antimatter is due to Paul Adrien Maurice Dirac [2]. In the mid-1920s, efforts to reconcile quantum mechanics with special relativity led to the formulation of the Klein–Gordon equation [3], which extended Schrödinger's non-relativistic framework by incorporating Einstein's relativistic energy–momentum relation. While successful in describing spin–0 particles, this equation exhibited several conceptual problems, most notably the presence of negative energy solutions and the inability to consistently describe particles with half-integer spin. These issues remained unresolved for several years and challenged the standard probabilistic interpretation of quantum mechanics.

In 1928, Dirac provided a decisive breakthrough by formulating a relativistically consistent wave equation for fermions [3]. His approach naturally incorporated spin and yielded both positive- and negative-energy solutions while maintaining a positive-definite probability density. Unlike earlier formulations, the negative-energy states could not be dismissed and were required for mathematical completeness. Dirac initially interpreted these states through what later became known as the "Dirac sea," an idea that implied the existence of particles identical in mass but opposite in electric charge to ordinary fermions.

At first, Dirac speculated that the proton might play the role of the electron's antiparticle, but this hypothesis was quickly ruled out due to the large mass difference. Shortly thereafter, Robert Oppenheimer and Hermann Weyl demonstrated that the antiparticle of the electron must have a mass comparable to that of the electron itself. This led to the prediction of the antielectron, later called the positron, marking the first concrete theoretical anticipation of antimatter as a fundamental component of nature.

The discovery of the positron

The positron was discovered in 1932 by Carl David Anderson [4]. Using a cloud chamber immersed in a magnetic field, Anderson observed a positively charged cosmic-ray particle with a mass compatible with that of the electron. The characteristics of the track ruled out a proton interpretation, providing the first experimental evidence for the positron.

The discovery of the antiproton

In 1955, Owen Chamberlain and Emilio Segrè observed the antiproton at the Berkeley National Laboratory [5]. Using the Bevatron accelerator, 6.2 GeV protons were collided with a fixed copper target, producing particles that were analyzed with magnetic elements, scintillators, and Cherenkov detectors. Among the products, a small number of negatively charged particles with a mass compatible with that of the proton were identified, providing the first experimental evidence for the antiproton. The production rate was extremely low, with an antiproton-to-pion ratio of about $1/44000$.

The discovery of the antideuteron

The discovery of the antiproton following that of the positron had a profound impact on particle physics, demonstrating that antiparticle counterparts exist for both leptons and hadrons. This result strongly supported the hypothesis of more complex forms of antimatter, including antinuclei, and motivated intense experimental activity. At the same time, the study of antimatter became closely connected to fundamental symmetry tests, particularly CPT invariance, which gained further relevance after the observation of parity and CP violation [6]. In this context, the search for bound states of antinucleons, such as the antideuteron, emerged as a natural next step.

The first artificial production of antinuclei was achieved independently in 1965 by a group led by Antonino Zichichi at CERN using the Proton Synchrotron (PS) [7], and by a group led by Leon Ledermann and Samuel C. C. Ting at Brookhaven National Laboratory using the Alternating Gradient Synchrotron (AGS) [8, 9]. At CERN, 19.2 GeV/c protons were collided with a beryllium target, and negatively charged particles with a mass compatible with that of the deuteron were identified. A clear candidate signal was observed as a peak in the mass spectrum measured by the electrostatic separator (Fig. 1.1), corresponding to an antideuteron. The measured antideuteron-to-pion ratio was of the order of 8×10^{-9}. A similar observation was reported at Brookhaven, where antideuteron candidates with a mass of about 1.86 GeV/c^2 were detected in proton–beryllium collisions. Searches for heavier antinuclei, such as antitritons, were also performed, but no signals were observed in those early experiments.

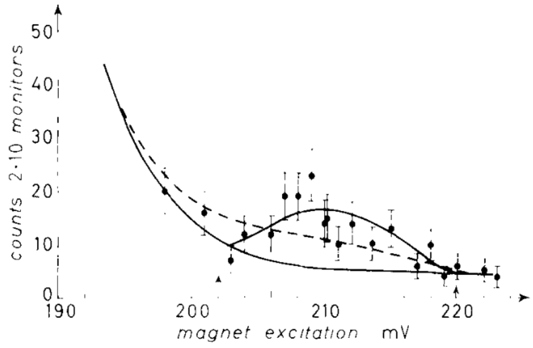

Figure 1.1: The antideuteron signal as a peak measured by the electrostatic separator [7]

The discovery of A = 3 antinuclei

The first antinuclei with $A = 3$ were discovered a few years later. In 1970, the first antihelium-3 ($^3\overline{\mathrm{He}}$) nuclei were produced using the U-70 accelerator at Serpukhov, Russia [10]. The U-70 synchrotron was able to accelerate protons up to 76 GeV, and proton beams of 70 GeV were made to collide with an aluminium target, above the estimated production threshold for $^3\overline{\mathrm{He}}$ and antitritium. Five $^3\overline{\mathrm{He}}$ candidates were identified among 2.4×10^{11} measured particles, with mass and charge compatible with the expected values. In 1974, the group at Serpukhov led by N. K. Vishnevsky discovered the antitriton, observing the first four candidates [11]. After these results, the discovery of new antinuclei produced at proton accelerators in pA collisions reached a stall. Nevertheless, the study of antinuclei production mechanisms remained of great interest.

The discovery of the anti-alpha particle

At the end of the 1970s, it became clear that a significant increase in production yields was required to further study the properties of antimatter. The technological limitations of fixed-target experiments prevented improvements by orders of magnitude, motivating, in the early 1980s, the upgrade of major proton accelerators such as the AGS and the PS to enable heavy-ion acceleration. At the AGS, gold–gold (Au–Au) collisions were achieved at a center-of-mass energy per nucleon pair of $\sqrt{s_{\mathrm{NN}}} = 4.8$ GeV, while the PS enabled lead–lead (Pb–Pb) collisions at $\sqrt{s_{\mathrm{NN}}} = 17$ GeV. Further studies were carried out by the NA49 experiment at CERN in Pb–Pb collisions at $\sqrt{s_{\mathrm{NN}}} = 17.2$ GeV [12], marking an important phase in the development of heavy-ion collision physics and allowing the observation of new states of matter such as quark–gluon plasma (QGP).
At the beginning of the 2000s, the Relativistic Heavy Ion Collider (RHIC [13]) at BNL started operations with the BRAHMS, PHENIX, PHOBOS, and STAR experiments. Heavy-ion collisions were performed up to $\sqrt{s_{\mathrm{NN}}} = 200$ GeV. While the primary goal of the RHIC physics programme was the study of the quark–gluon plasma [14, 15], the experiments also led to important discoveries in antimatter physics. In particular, the STAR Collaboration observed antideuteron and antihelium-3 production in $\sqrt{s_{\mathrm{NN}}} = 130$ GeV [16], and reported the first observation of antinuclei with $A = 4$, (antihelium-4), produced in Au–Au collisions at $\sqrt{s_{\mathrm{NN}}} = 200$ GeV [17]. These results confirmed the exponential suppression of light (anti)nuclei yields with increasing baryonic number, extending earlier observations up to $A = 4$.

Antinuclei from pp collisions

At the beginning of the 1970s, the search for hadrons heavier than protons produced in pp collisions was mainly carried out at CERN at the Intersecting Storage Rings (ISR) [18, 19], the world's first hadron collider. There, the antideuteron production cross section

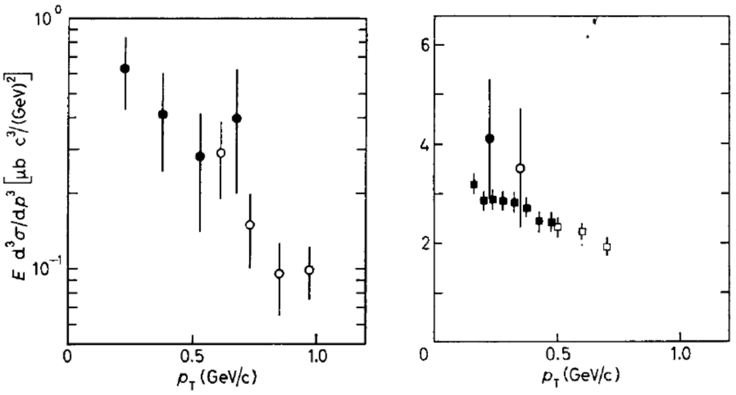

Figure 1.2: (Left) Invariant differential cross sections for antideuteron production in proton–proton collisions at $\sqrt{s} = 45\ \mathrm{GeV}$, with statistical uncertainties only. The filled symbols correspond to data taken at $\sqrt{s} = 53\ \mathrm{GeV}$ at the ISR. (Right) The deuteron–to–antideuteron ratio (circles) compared with the square of the proton–to–antiproton ratio (squares), evaluated at half the transverse momentum (p_T/A, with A = 2), for both ISR energies [18, 19].

was measured in pp collisions at $\sqrt{s} = 45$ and 53 GeV at low transverse momentum. These measurements, shown in Fig. 1.2, suffered from large statistical uncertainties and led to an antideuteron-to-deuteron ratio of about 3–5, indicating a clear dominance of matter over antimatter production at these energies. In 2009, the energy frontier was reached with the start of the Large Hadron Collider (LHC), operating in pp collisions at center-of-mass energies from $\sqrt{s} = 900$ GeV up to 13.6 TeV. Thanks to the large integrated luminosities and advanced detector systems, the ALICE experiment performed an extensive program of measurements of light (anti)nuclei production in different collision systems and energies. In particular, ALICE measured the transverse-momentum spectra of deuterons and antideuterons in inelastic pp collisions over a wide energy range [20], enabling precise tests of the antimatter-to-matter balance at LHC energies. The measured antinucleus-to-nucleus ratios were found to approach unity as the collision energy increases, in agreement with expectations and with the behavior observed for antibaryon-to-baryon ratios [21]. More recently, ALICE extended these studies to heavier antinuclei, measuring (anti)helium production in several collision systems, including pp collisions at $\sqrt{s} = 7$ and 13 TeV [22], as well as p–Pb and heavy-ion collisions [23, 24, 25, 26]. These measurements represent the most comprehensive set of light antinuclei results obtained at collider experiments and provide a benchmark for comparisons with earlier low-energy measurements.

1.2 Strong interaction

The strong interaction, described by Quantum ChromoDynamics (QCD) [27], is a key component of the Standard Model and governs quarks and gluons, the only particles carrying color charge. This chapter provides a brief introduction to QCD followed by a discussion of the nucleon–nucleon interaction.

1.2.1 Quantum Chromodynamics in the Standard Model

Quarks exist in six flavors and three color charges (red, green, blue). Each quark is a spin-$1/2$ fermion described by the spinor field ψ_c^f, where f denotes the flavor and c the color, while gluons are the eight spin-1 gauge fields mediating the strong interaction. Quantum Chromodynamics (QCD) is the non-abelian gauge theory based on the symmetry group $SU(3)_c$ [27]. Because the group is non-abelian, colored states cannot be isolated: quarks are confined inside color-neutral hadrons. The free quark Lagrangian is

$$\mathcal{L}_0 = \sum_{f=1}^{6} \sum_{C=r,g,b} \overline{\psi}_c^f (i\gamma^\mu \partial_\mu - m_0^f) \psi_c^f. \tag{1.1}$$

Requiring local $SU(3)_c$ invariance replaces the derivative ∂_μ with the covariant derivative

$$D_\mu = \partial_\mu + i g_s A_\mu, \tag{1.2}$$

where $\alpha_s = g_s^2/(4\pi)$ is the strong coupling constant and A_μ are the eight gluon fields. These fields transform as

$$A^\mu \rightarrow A^{\mu'} = U(x) A^\mu U^{-1}(x) + \frac{i}{g_s} [\partial^\mu U(x)] U^{-1}(x), \tag{1.3}$$

with $U(x)$ a unitary matrix in $SU(3)_c$.
The gluon field-strength tensor is defined via

$$[D_\mu, D_\nu] = i g_s F_{\mu\nu}, \tag{1.4}$$

allowing one to write the full QCD Lagrangian:

$$\mathcal{L}_{\mathrm{QCD}} = \sum_{f=1}^{6} \sum_{C=r,g,b} \overline{\psi}_c^f (i\gamma^\mu D_\mu - m_0^f) \psi_c^f - \frac{1}{4} \sum_{a=1}^{8} F_{\mu\nu}^a F^{a\,\mu\nu}. \tag{1.5}$$

This expression contains both quark–gluon and gluon–gluon interaction terms, the latter reflecting gluon self-interaction, visible in Fig. 1.3.
Vacuum polarization induces screening by quark loops and anti-screening by gluon loops,

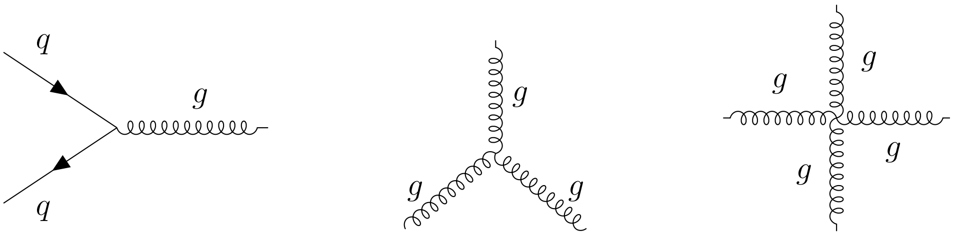

Figure 1.3: QCD basic Feynman vertices.: quark–gluon, three-gluon, and four-gluon.

leading to confinement at large distances and to asymptotic freedom [28] at short distances. The scale dependence of the strong coupling α_s [29] is shown schematically in Fig.1.4. At low quadri-momentum transfer (Q), $\alpha_s \approx 1$, making perturbation theory ineffective; in this regime lattice QCD is required. At higher Q, perturbative QCD becomes applicable, and for energies above $O(100\text{ GeV})$ quarks and gluons behave as nearly free, forming a deconfined state of matter [30].

The $SU(3)_c$ invariance ensures conservation of color charge, while the additional $U(1)$ and $SU(2)$ symmetries of the strong sector imply, respectively, fermion number conservation and strong isospin conservation (restricted to up and down quarks).

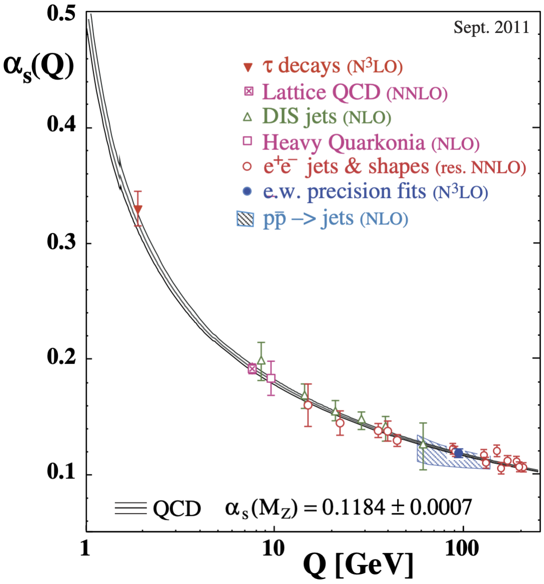

Figure 1.4: The strong coupling α_s is shown as a function of the energy scale Q, with all values calculated at the energy equivalent to the Z-boson mass [29].

1.2.2 Nucleon–Nucleon interaction

Quarks are the elementary constituents of nucleons, namely protons (up–up–down) and neutrons (up–down–down). Deriving the nuclear force directly from quark and gluon dynamics is extremely difficult and requires large computational resources. At low energies, the nuclear force can be interpreted as a residual color interaction among quarks and is therefore studied within non-perturbative QCD, typically through lattice QCD or effective field theory approaches [31, 32].

In nuclear physics, the properties of the nucleon–nucleon (N–N) interaction can be summarized as follows:

- At short distances, the strong interaction becomes stronger than the Coulomb force, allowing it to overcome the repulsion between protons within a nucleus.
- The strong interaction is short-ranged: at distances comparable to atomic scales the nuclear force becomes negligible, leaving the Coulomb force as the relevant interaction.
- Colorless particles, such as electrons, do not experience the strong force.
- The N-N interaction exhibits isospin symmetry, meaning it is independent of whether the nucleon is a proton or a neutron.
- The N–N interaction depends on the spin configuration of the nucleons involved (triplet or singlet state).
- A repulsive component of the potential is required at very short distances to maintain an average separation between nucleons. This term must be non-central to ensure the non-conservation of orbital angular momentum.

These characteristics must be incorporated into the Hamiltonian and into the Schrödinger equation when modeling nuclear structure.

Deuteron

The simplest two–nucleon system that admits an analytic quantum–mechanical solution is the deuteron (d or $^2\mathrm{H}$), composed of one proton and one neutron. These nucleons interact through the strong force and do not experience Coulomb repulsion nor Pauli blocking. By comparing model predictions with experimental observations, the main features of the nuclear force can be tested.

In a first approximation, the interaction between the two nucleons can be described by a square–well potential of depth V_0 and range R, as shown in Fig. 1.5. A bound state exists only if the potential depth exceeds the kinetic energy of the pair. Using

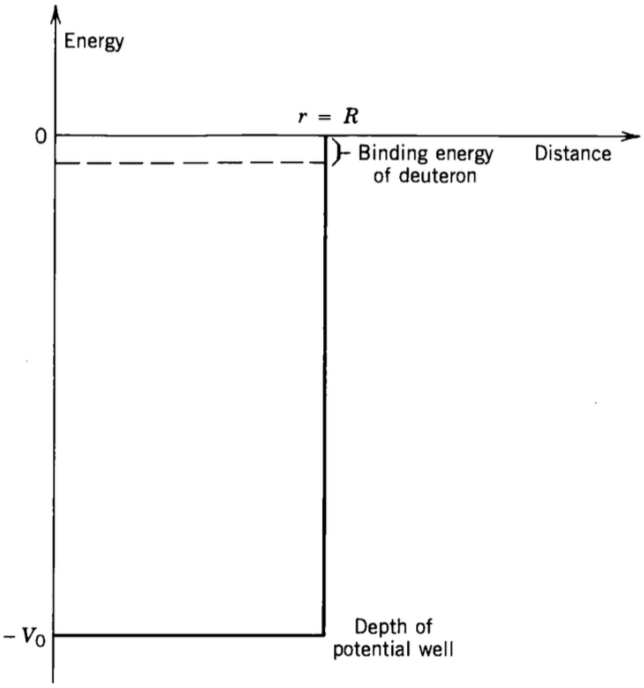

Figure 1.5: Square–well potential used to model the deuteron, with depth V_0 and range R. The bound-state energy corresponds to the deuteron binding energy [33].

$R \approx 2.1\,\mathrm{fm}$, consistent with the charge radius of the deuteron (visible in Tab. 1.1), and μ as the reduced mass of the proton–neutron system, the condition becomes

$$V_0 > E_{\mathrm{kin}} = \frac{\hbar^2\pi^2}{8\mu c^2 R} = 23.1\,\mathrm{MeV}. \tag{1.6}$$

The ground–state binding energy obtained from this model is

$$E_{\mathrm{BE}} = E_{\mathrm{kin}} - V_0 = -2.2\,\mathrm{MeV}. \tag{1.7}$$

This value agrees well with the precise experimental determination [34], obtained from the mass difference between proton (p), neutron (n), and deuteron (d):

$$E_{\mathrm{BE}} = [m(p) + m(n) - m(d)] \approx 2.224575 \pm 0.00004\,\mathrm{MeV}. \tag{1.8}$$

The square–well potential is written as

$$V(r) = \begin{cases} -V_0 & r < R, \\ 0 & r > R, \end{cases} \tag{1.9}$$

where r is the relative coordinate of the two nucleons.
The Schrödinger equation for the system is

$$\left(-\frac{\hbar^2}{2\mu}\frac{1}{r^2}\frac{\partial}{\partial r}\left(r^2\frac{\partial}{\partial r}\right) + \frac{\hat{L}^2}{2\mu r^2} + V_{\mathrm{nucl}}(r)\right)\Psi_{n,l,m}(r,\theta,\phi) = E_n\Psi_{n,l,m}(r,\theta,\phi), \tag{1.10}$$

where $\mu = \frac{m_p m_n}{m_p + m_n}$ is the reduced mass, $\hat{L}^2$ is the angular momentum operator, $V_{\mathrm{nucl}}(r)$ is the nuclear potential of Eq. 1.9, and $\Psi_{n,l,m}$ is the two–body wave function in spherical coordinates.
The ground state of the deuteron corresponds to orbital angular momentum $l = 0$. No excited bound states exist, because any excitation energy would break the system into a free proton and a free neutron.
Since the problem is central, the Schrödinger equation separates into radial and angular parts. The angular solutions are the spherical harmonics:

$$\hat{L}^2 Y_l^m(\theta,\phi) = \hbar^2 l(l+1) Y_l^m(\theta,\phi). \tag{1.11}$$

For $l = 0$, the radial equation is

$$\left[-\frac{\hbar^2}{2\mu}\frac{1}{r}\frac{\partial^2}{\partial r^2} + V_{\mathrm{nucl}}(r)\right] u_0(r) = E_0\, u_0(r), \tag{1.12}$$

whose solutions are

$$u_0(r) = A\sin(k_1 r) + B\cos(k_1 r), \qquad 0 < r < R,$$

$$u_0(r) = Ce^{-k_2 r} + De^{k_2 r}, \qquad r > R,$$

with

$$k_1 = \sqrt{2m(V_0 + E)/\hbar^2}, \qquad k_2 = \sqrt{-2mE/\hbar^2}.$$

The constants A, B, C, and D follow from the boundary conditions requiring continuity of $u(r)$ and $\partial_r u(r)$.
Spin interactions must also be considered, contributing a spin–dependent term to the potential. The total angular momentum is

$$\vec{I} = \vec{L} + \vec{S}_n + \vec{S}_p + \vec{L} \cdot \vec{S}, \tag{1.13}$$

where $\vec{S}_n$ and $\vec{S}_p$ are the neutron and proton spins (each $1/2$), $\vec{L}$ is the orbital angular momentum (zero for $l = 0$), and $\vec{L}\vec{S}$ is the spin–orbit term. In principle, the total spin can form a singlet state ($I = 0$) or a triplet state ($I = 1$). The deuteron is observed exclusively in the triplet configuration, which corresponds to the lower energy state.

1.2.3 Argonne ν_{18}

Many nucleon–nucleon interaction potentials have been developed with the primary goal of reproducing the experimentally measured nucleon–nucleon scattering observables, in particular the phase shifts extracted from elastic scattering data. Among these, one of the most successful phenomenological models is the Argonne ν_{18} potential [35], a high-quality nonrelativistic and explicitly charge-dependent N–N potential. It consists of a charge-independent part (Argonne ν_{14}), supplemented by additional charge-dependent and charge-asymmetric operators, together with the electromagnetic interaction. The latter accounts for long-range contributions such as Coulomb, Darwin–Foldy (a small relativistic correction related to the finite mass of the nucleon), vacuum polarization, and magnetic moment terms. The resulting potential is local and is constructed directly in coordinate space, without separating the interaction into partial-wave components.

The parameters of the Argonne ν_{18} potential were obtained by a direct fit to the Nijmegen N–N scattering database, reproducing proton–neutron elastic scattering data with a reduced chi-square $\chi^2 \sim 1$ for laboratory energies up to 350 MeV [35]. In this framework, the quality of a potential is assessed by its ability to reproduce the experimental phase shifts in all relevant partial waves, which encode the angular-momentum- and spin-dependent structure of the interaction. The agreement between the Argonne ν_{18} predictions and the experimental phase-shift analyses for np, pp, and nn scattering, compared with other interaction models, is shown in Fig. 1.6.

Beyond scattering observables, the Argonne ν_{18} interaction provides an accurate description of bound nuclear systems. In particular, it predicts the internal structure of

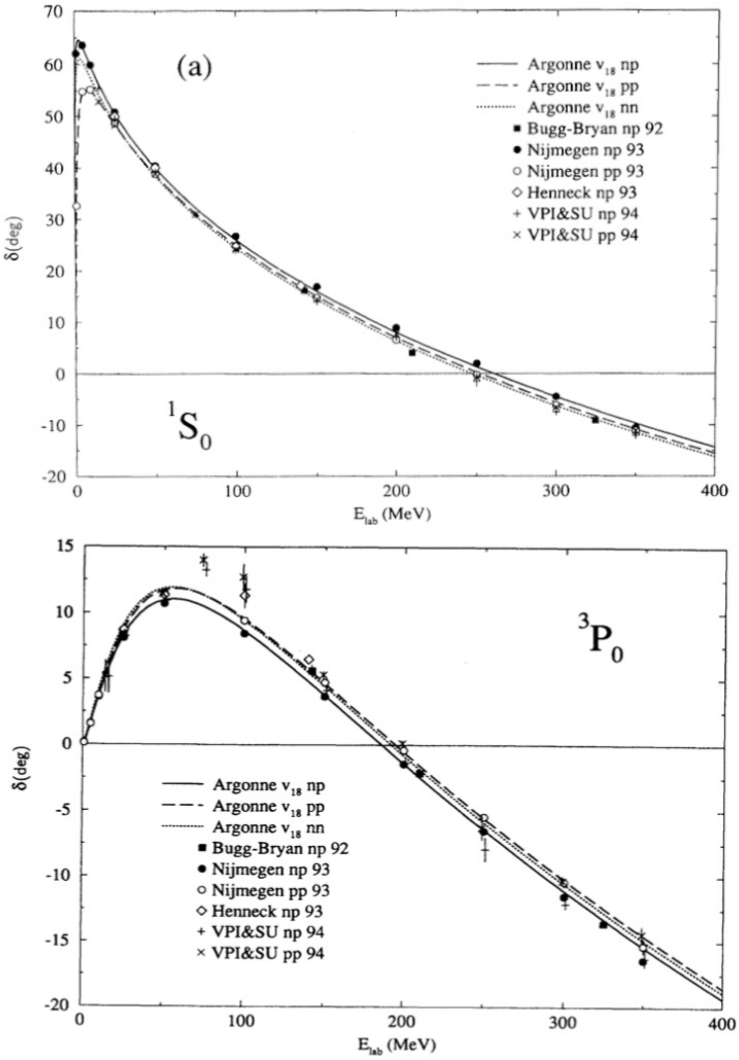

Figure 1.6: Comparison of phase shifts in the $^1S_0$ and $^3P_0$ channels for np, pp, and nn scattering from the Nijmegen database with fits obtained using the charge-dependent Argonne ν_{18} interaction [35].

the deuteron through the radial wave functions of its dominant S-state and admixture D-state components, $u(r)/r$ and $w(r)/r$, respectively, shown in Fig. 1.7. These wave functions reflect the tensor component of the nuclear force and are essential for a quantitative description of deuteron properties. Using them, electromagnetic observables of the deuteron have been recalculated with high precision, further demonstrating the reliability of the Argonne ν_{18} potential as a realistic model of the nucleon–nucleon interaction.

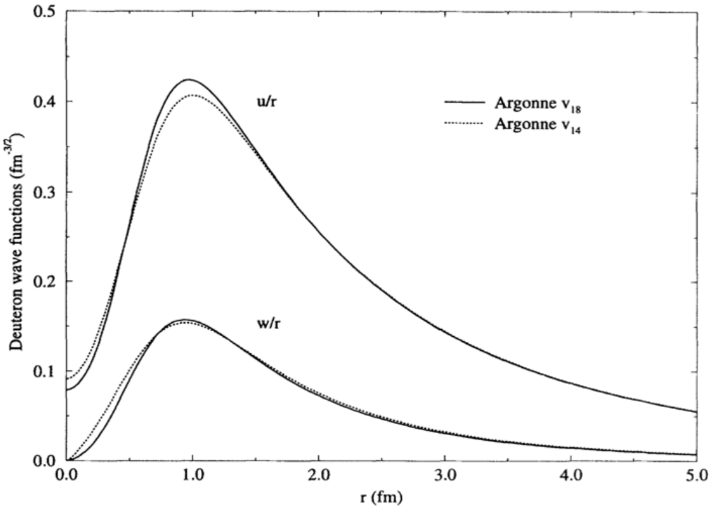

Figure 1.7: The deuteron $u(r)/r$ and $w(r)/r$ wave functions for the S- and D-state components, obtained using the Argonne ν_{18} potential and compared with the charge-independent Argonne ν_{14} interaction [35].

1.3 Production models of (anti)nuclei

The production of light (anti)nuclei in high-energy collisions is usually described through two different approaches: formation by nucleon coalescence or thermal–statistical production.

Thanks to large amounts of data from pp, p–Pb and Pb–Pb collisions collected during the first ten years of data taking at LHC, ALICE has measured the production of light (anti)nuclei at different center-of-mass energies, providing crucial experimental data [36]. Some properties of the (anti)nuclei under discussion are reported in Table 1.1. In Fig. 1.8, for example, the transverse-momentum distributions for deuteron and antideuteron are shown as measured by ALICE at rapidity $|y| < 0.5$ in inelastic pp collisions at $\sqrt{s}$ = 900 GeV, 2.76 TeV and 7 TeV [20].

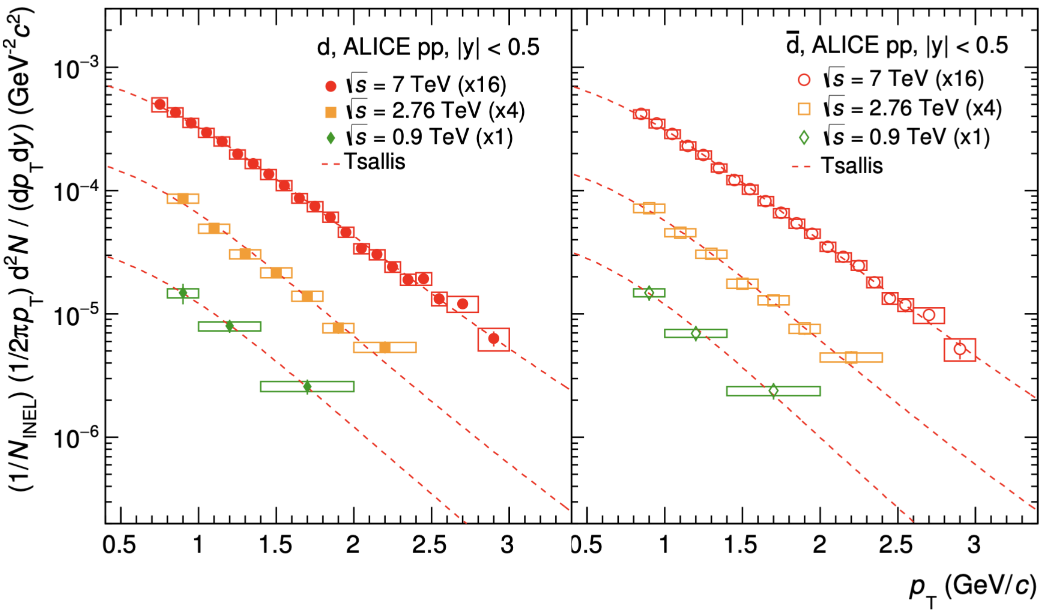

Figure 1.8: Invariant differential yield of deuterons (left) and antideuterons (right) in inelastic pp at $\sqrt{s}$ = 0.9, 2.76 and 7 TeV. Systematic uncertainties are represented by boxes and the data are multiplied by constant factors for clarity in the figure. The lowest-p_T point for deuterons at $\sqrt{s}$ = 7 TeV was taken from [37]. The dashed line represents the result of a fit with a Tsallis function [20].

In collision systems in which few particles are produced in the final state (often referred to as "small collision systems" or "low multiplicity"), the experimental data seem to confirm the validity of coalescence. Moreover, the most recent measurements as a function of the charged-particle multiplicity indicate a dependence of the coalescence process on the source volume [24].

This aspect is particularly evident from measurements of nuclear production in heavy-ion collisions, where coalescence models that do not take the source size into account fail to reproduce the experimental data [42]. On the other hand, it has been observed that the production of light (anti)nuclei measured in Pb–Pb collisions at LHC [37] is consistent with the predictions of the statistical hadronisation ("thermal") model [43], which assumes that the particle source is quantum gas of fermions and bosons in thermal and chemical equilibrium. It is worth recalling here that in Pb–Pb collisions the production of a state of nuclear matter, the quark–gluon plasma (QGP), is expected, in which quarks and gluons, the fundamentals constituents of hadronic matter, are no longer confined within the nucleons of the incoming nuclei but are almost free. This phase of nuclear matter occurs at high energy densities and high temperatures (of the order of 10^2 MeV [44], which is the critical temperature around which this transition occurs, as predicted by

Mass number	Nucleus	Composition	E_{BE} (MeV)	Spin J_A	λ_A^{meas} (fm)	r_A (fm)	Refs.
A = 2	d	pn	2.224575 (9)	1	2.1413 $\pm$ 0.0025	3.2	[38, 34]
A = 3	^{3}H	pnn	8.4817986 (20)	1/2	1.755 $\pm$ 0.086	2.15	[39]
A = 3	^{3}He	ppn	7.7180428 (23)	1/2	1.959 $\pm$ 0.030	2.48	[39]
A = 4	^{4}He	ppnn	28.29566 (20)	0	1.6755 $\pm$ 0.0028	1.9	[40, 41]

Table 1.1: Properties of nuclei with A ≤ 4. E_{BE} is the binding energy, r_A is the harmonic-oscillator size parameter, chosen to approximate the measured characteristic size of the charge distribution, λ_A^{meas}.

theoretical calculations). As soon as the quark–gluon plasma produced in the collision expands and cools, quarks and gluons are reconfined into hadrons, crossing the phase transition. In thermal models, it is assumed that nuclei and light antinuclei are produced together with other light particles such as pions and protons at instants just after the phase transition.

The statistical model predicts only the number of (anti)nuclei produced, but does not describe their formation from a dynamical point of view. The coalescence model, instead, allows the production of nuclei from nucleons to occur later during the expansion phase of the hadronic gas. Moreover, it provides a dynamical description of the formation process of the bound states. In this section, therefore, we focus on the coalescence model for the formation of (anti)nuclei, as it is the model we use for the later development.

1.3.1 Statistical Hadronisation Models

Statistical Hadronisation Models (SHM), are used to describe and predict the abundances of hadrons produced in high-energy particle collisions. Their origins trace back to the pioneering work of Fermi in the 1950s [45], later extended by Hagedorn in the 1960s [46]. A major milestone was reached in the 1990s, when SHM successfully reproduced hadron yields measured in heavy-ion collisions at the BNL AGS and in Si+Au(Pb) systems [47]. In the same period, the influence of resonance decays on pion spectra was quantitatively described within a thermal framework [48].

The main assumption of SHM is that, at hadronisation, all particle species compatible with conservation laws can be produced, with relative abundances determined by their statistical weights. The medium formed after the collision is modelled as an expanding hadron-resonance gas (HRG), composed of non-interacting hadrons and resonances. Depending on the size of the interaction volume, different statistical ensembles are used to enforce the conservation of quantum numbers.

In central relativistic heavy-ion collisions, where $\mathcal{O}(10^3)$ hadrons are produced per unit of rapidity in the final state, the large particle multiplicity drives the system close to the

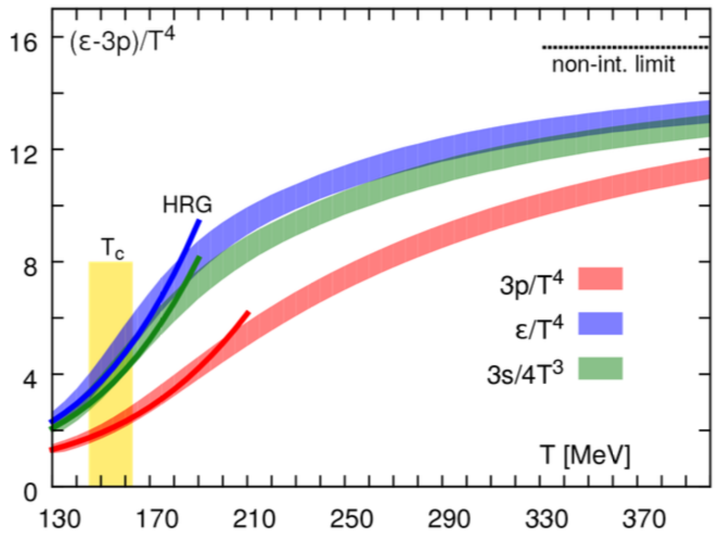

Figure 1.9: Comparison between the equation of state predicted by the Hadron Resonance Gas model and lattice QCD calculations [50].

thermodynamic limit, making the Grand Canonical (GC) ensemble applicable [43]. In this framework, energy and conserved charges (baryon number, strangeness, and electric charge) are conserved on average. The thermodynamic properties of the system are described by a small set of parameters, namely the temperature T, the volume V, and the chemical potentials associated with the conserved charges. The HRG formulation successfully reproduces the QCD equation of state obtained from lattice calculations over a broad temperature range below the deconfinement transition [44, 49, 50]. A comparison between HRG and lattice QCD predictions is shown in Fig. 1.9.

Within the GC-SHM, hadron yields depend primarily on the temperature and chemical potentials, while the explicit volume dependence cancels out when yield ratios are considered. Resonance decays provide an essential contribution to the final observed yields and must be included to accurately reproduce experimental data [43]. The model successfully describes hadron yields over a wide mass range, from pions up to light (anti)nuclei. As shown in Fig. 1.10, particle yields exhibit an approximately exponential dependence on particle mass, with deviations for light hadrons due to feed-down contributions.

Remarkably, the SHM also reproduces the yields of light (anti)nuclei, despite their binding energies being much smaller than the chemical freeze-out temperature [43, 51]. Their production is governed by phase-space population rather than by their internal structure. The model further predicts the antimatter-over-matter ratios as a function of

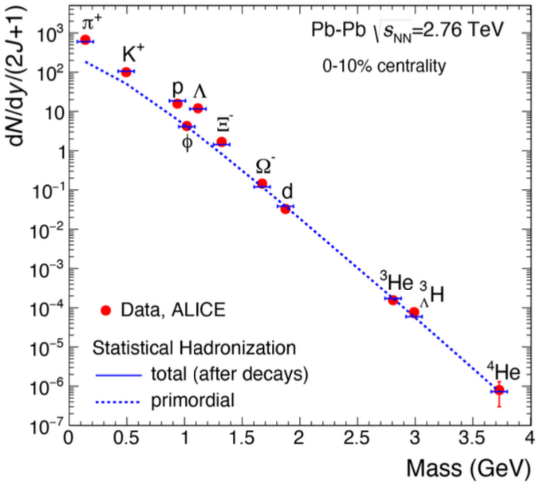

Figure 1.10: Hadron yields measured in central Pb–Pb collisions at $\sqrt{s_{\mathrm{NN}}} = 2.76$ TeV as a function of particle mass, compared with SHM predictions [43].

collision energy, with matter–antimatter symmetry emerging at LHC energies where the baryochemical potential approaches zero [52].
For smaller systems, such as pp or e^+e^- collisions, the assumptions of the GC ensemble are no longer valid due to the limited reaction volume. In these cases, exact local conservation of quantum numbers must be imposed, leading to the Canonical Statistical Hadronisation Model (CSM) [53, 54, 55, 56]. A direct consequence of the canonical treatment is the suppression of particles carrying conserved charges, known as canonical suppression, which is particularly pronounced for strange hadrons.

The canonical approach has been extended to include light (anti)nuclei and applied to LHC energies using modern implementations such as the Thermal-FIST framework [57]. While a baseline CSM assuming full chemical equilibrium reproduces several yield ratios, it fails to describe observables such as the K/π and ϕ/π ratios at low multiplicity [53, 58]. These discrepancies indicate incomplete chemical equilibration in small systems.

An improved description is obtained by introducing a strangeness saturation factor γ_S, leading to the γ_S-CSM [59, 60]. This extension accounts for incomplete strangeness equilibration and allows for a system-size-dependent freeze-out scenario. With a correlation volume scaling with the charged-particle multiplicity, this model provides a significantly improved description of hadron and light-nucleus yields across different collision systems and multiplicities [58].

1.3.2 Coalescence model

The coalescence approach is still a subject of intense discussion and research [42, 61, 62, 63, 64, 65]. In the coalescence model the nucleons produced in the collision bind if they have similar coordinates and momenta, therefore if they are close in phase space. In the earliest, simplest coalescence models [61, 62], given two nucleons with momenta $\vec{p}_1$ and $\vec{p}_2$, coalescence occurs if

$$|\vec{p}_1 - \vec{p}_2| < p_0 \tag{1.14}$$

with p_0 called the coalescence momentum.

For a nucleus with mass number A (where A = Z + N, with Z the number of protons and N the number of neutrons), the coalescence probability is expressed through the coalescence parameter B_A, defined by the relation [63]:

$$E_A \frac{d^3N}{d^3p_A} = B_A \left(E_p \frac{d^3N_p}{d^3p_p} \right)^Z \left(E_n \frac{d^3N_n}{d^3p_n} \right)^N \tag{1.15}$$

where E_A is the energy of the nucleus, $\vec{p}_A$ the momentum of the nucleus, $\vec{p}_p$ the momentum of the individual protons, and $\vec{p}_n$ the momentum of the individual neutrons. If one assumes that the energy distributions of protons and neutrons are the same, one has:

$$E_A \frac{d^3N}{d^3p_A} = B_A \left(E_{p,n} \frac{d^3N_{p,n}}{d^3p_{p,n}} \right)^A \Bigg|_{p_p = p_n = \frac{p_A}{A}} . \tag{1.16}$$

This assumption allows Eq. 1.16 to be used for the experimental extraction of the coalescence parameter B_A from measured proton spectra only, since neutrons are experimentally difficult to detect (for example, the ALICE apparatus detects only charged particles). At high energies it is nevertheless reasonable to assume that protons and neutrons are produced with the same distribution due to isospin symmetry.
In Fig. 1.11, the coalescence parameter for deuterons and antideuterons, B_2, is shown as a function of the transverse momentum per nucleon, as measured by ALICE in inelastic pp collisions at $\sqrt{s} = 900$ GeV, 2.76 TeV, and 7 TeV [20]. From the comparison of the values on the vertical axis at the different collision energies, it can be observed that B_2 does not exhibit a significant dependence on $\sqrt{s}$ when increasing the energy from 900 GeV to 7 TeV. In Fig. 1.12, the same behaviour can be observed for different collision systems.
The simplest coalescence models however, in which B_A does not depend on the source size, are not able to explain some measurements, such as the elliptic flow of deuterons—an observable sensitive to the hydrodynamic collective evolution of hadrons produced by the QGP in heavy-ion collisions and to the space–momentum correlations that arise

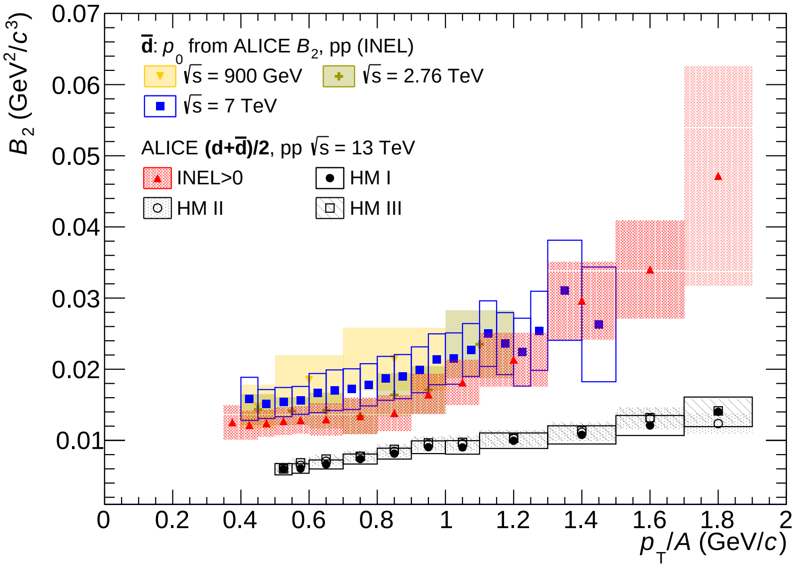

Figure 1.11: Coalescence parameter B_2 as a function of the transverse momentum per nucleon for antideuterons in inelastic pp collisions at $\sqrt{s} = 900$ GeV (yellow triangles), $\sqrt{s} = 2.76$ TeV (green crosses), and $\sqrt{s} = 7$ TeV (blue squares). The (anti)deuteron B_2 distribution for pp collisions at $\sqrt{s} = 13$ TeV is also shown for different multiplicity classes (red triangles for minimum bias, black filled circles for HM I, open black circles for HM II, and open squares for HM III). Uncertainties are represented by boxes [20].

from the collision geometry [69]. More advanced coalescence models [63] take into account the dependence of the coalescence parameter on the source size R, and show that since nucleons must be close in order to coalesce, B_A decreases as R increases.

Role of the source in the coalescence process

Coalescence is a quantum-mechanical process; for this reason the classical definition of phase space is replaced by the Wigner formalism in most recent approaches [63, 70]. The wave function of a nucleus can be approximated by the stationary-state wave functions of a spherically symmetric isotropic harmonic oscillator with r_A as the only characteristic size parameter.
For the deuteron d, a possible Gaussian wave function is

$$\phi_d(\vec{r}) = (\pi r_d^2)^{-\frac{3}{4}} exp\left(-\frac{r^2}{2r_d^2}\right). \tag{1.17}$$

To produce a deuteron by coalescence, in quantum-mechanical terms, one must project the bound-state wave function onto the wave function of the pair formed by the nucleons

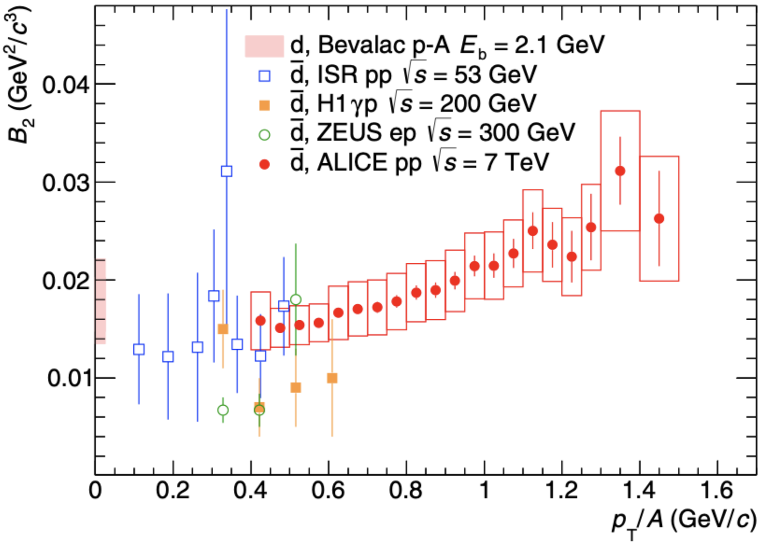

Figure 1.12: Coalescence parameter B_2 for antideuterons produced in inelastic pp collisions at $\sqrt{s} = 7\,\mathrm{TeV}$ (circles), compared with measurements at lower energies in pp [18, 19], γp [66], and ep [67] collisions (squares and open circles), as well as in p–Cu and p–Pb collisions [68] (band at $p_\mathrm{T}/A = 0\,\mathrm{GeV}/c$) [20].

of interest, i.e. a proton and a neutron:

$$\frac{d^3N_d}{dp_d^3} = tr(\rho_d \rho_{pn}) \tag{1.18}$$

where ρ_d is the density matrix of deuterons, ρ_{pn} is the two-nucleon density matrix, and tr denotes the trace of a matrix.

The quantum-mechanical nature of the coalescence products is implemented in the model through the introduction of an average correction factor $\langle C_A \rangle$, which accounts for both the spatial distribution of the nucleon source and the spatial distribution of the nucleons themselves (both are extended, non-pointlike objects). In particular, one obtains [63]:

$$\langle C_A \rangle = \prod_{i=1}^{3} \left[1 + \frac{r_i^2}{4R_i^2} \right]^{-\frac{1}{2}(A-1)} \tag{1.19}$$

where R_i are the characteristic dimensions of the coalescence volume. This formulation was introduced in [63] with Pb–Pb collisions in mind, where the volume from which nucleons—and thus nuclei—are emitted is spatially extended. For deuteron (D, A = 2), it can be written as

$$\langle C_D \rangle \approx \left[1 + \left(\frac{r_D}{2R(m_T)}\right)^2\right]^{-\frac{3}{2}} \tag{1.20}$$

In Eq. 1.20 it is evident that the probability of forming a bound state depends on the relation between the size of the nucleus and the size of the source. Assuming a spherical volume, i.e. $R_1 \approx R_2 \approx R_3 \approx R$, one can obtain:

$$B_A = \frac{2J_A + 1}{2^A} \frac{1}{\sqrt{A}} \frac{1}{m_T^{A-1}} \left(\frac{2\pi}{R^2 + (\frac{r_A}{2})^2}\right)^{\frac{3}{2}(A-1)} \tag{1.21}$$

where J_A denotes the spin of the nucleus, m_T its transverse mass, defined as $m_T = \sqrt{p_T^2 + m_A^2}$, with m_A the mass of the nucleus. The transverse momentum is given by $p_T = \frac{|\mathbf{p}_{T,1} + \mathbf{p}_{T,2}|}{2}$. Furthermore, r_A denotes the size of the produced nucleus, while R represents the size of the emission source.

Eq. 1.21 can be used to directly compare the predicted B_A with the experimental data. Eq. 1.21 explicitly accounts for the source size R, since the probability of coalescence naturally decreases for nucleons with similar momenta that are produced far apart

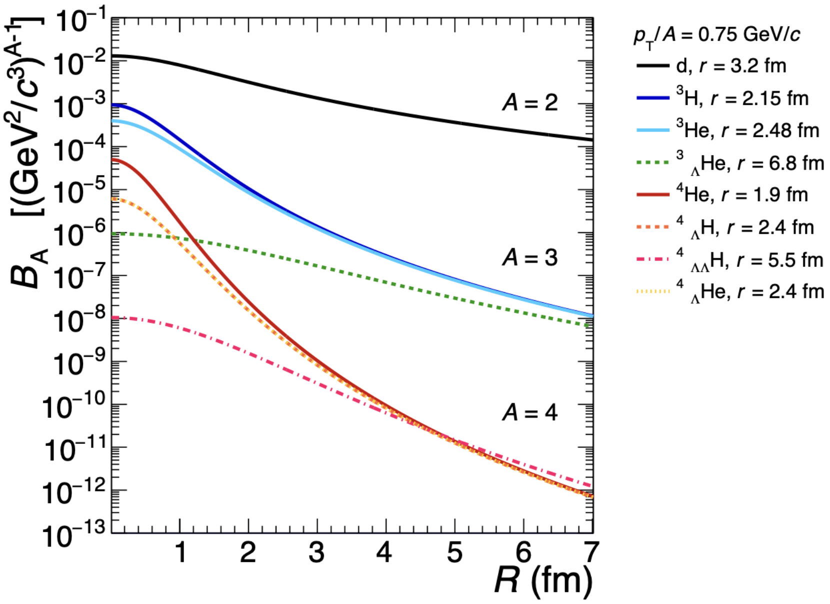

Figure 1.13: Coalescence parameter B_A as a function of the source radius R as predicted by the coalescence model (Eq. 1.21) for various composite objects with $p_T/A = 0.75$ GeV/c. For each (hyper)nucleus the legend reports the radius r used for the calculation; in cases where more than one estimate of the latter is available, the smaller value is adopted for the calculations [42].

in configuration space. Moreover, the source size is identified with the effective subvolume of the entire system from which particles with similar momenta are emitted, i.e. the femtoscopic homogeneity region as discussed in hydrodynamic and HBT studies [63]. This connection was later implemented in the coalescence framework in Ref. [71], and is experimentally accessible through femtoscopic interferometry techniques based on the measurement of two-particle correlation functions.
Fig. 1.13 shows the dependence on the source radius of B_A (Eq. 1.21) for nuclei with A = 2, 3 and 4 whose properties are reported in Table 1.1 and hypernuclei (nuclei where a neutron is replaced by a Λ baryon).
One observes that the coalescence probability decreases with increasing mass number and that B_A decreases as the radius increases. For a given A, the larger the radius of the object, the smaller B_A. For the same A, mass and spin (for example ^{3}H and ^{3}He), B_A differs only because of the different radius r_A and this difference is more relevant in small sources, because in extended collision systems the difference between nuclear radii is much smaller than the size of the source. Thus, for small sources, with $R \to 0$, the coalescence probability is inversely proportional to the harmonic-oscillator size parameter and, therefore, in the harmonic-oscillator model, proportional to the depth of the potential well, i.e. to the nuclear binding energy B_A. For a large source, where $R \gg r_A$, the coalescence probability is dominated by the classical phase-space separation, decreasing for large distances in configuration space.

1.4 Determination of nucleon source for coalescence

Considering two particles (for example a proton and a neutron) emitted by a source, there are two possibilities:

1. if the particles are emitted close in phase space they can bind and form a bound state;
2. if the particles are emitted far apart they do not form the bound state.

The correlation between coalescence probability and correlation function [70], in the case of the deuteron, is given by :

$$\mathcal{B}_2(p) \approx \frac{2(2s+1)}{m(2s_N+1)} \int d^3\mathbf{k}\mathcal{F}(\mathbf{k})C_2(p,\mathbf{k}) \tag{1.22}$$

where **k** is the relative momentum, s is the spin of the bound state, s_N is the spin of the nucleons and is equal to 1/2, m is the mass, p explicitly indicates the presence of a

proton, and $\mathcal{F}(\mathbf{k})$ is the momentum-space form factor.
The momentum-space form factor is closely related to the bound-state wave function, by the following defining equation:

$$|\phi(\mathbf{r})|^2 = \int \frac{d^3\mathbf{k}}{(2\pi)^3} e^{i\mathbf{kr}} \mathcal{F}(\mathbf{k}) \tag{1.23}$$

Eq. 1.22 states that the coalescence probability $\mathcal{B}_2(p)$ depends on the prefactor preceding the integral, set by the spin orientation and the Pauli exclusion principle; on $\mathcal{F}(\mathbf{k})$, hence on the bound-state wave function; and on $C(p, \mathbf{k})$, i.e. the correlation function that encodes the potential. Thus, again considering the deuteron, once its wave function is known and the source is determined, it is possible to obtain the coalescence probability. In Fig. 1.14 B_2 is shown as a function of the multiplicity pseudorapidity density of charged particles (or simply *multiplicity*)
$\langle dN_{ch}/d\eta_{lab}\rangle_{|\eta_{lab}|<0.5}$ for different collision systems and energies. The charged-particle multiplicity is a proxy of the system size [72]. The data corresponding to the different systems and collision energies confirm a dependence on multiplicity that can be interpreted as an effect of the interplay between the size of the system and that of the nucleus. In fact, at low charged-particle multiplicity, the size of the system is comparable to the size of the nucleus, leading to a slow decrease with multiplicity. Conversely, as the multiplicity increases, the system size becomes larger and larger than the nuclear size, making the coalescence process increasingly unlikely [37, 42].

1.4.1 Correlation function and source size

The femtoscopy technique makes it possible to determine the space–time characteristics of the source that emits the particles using the measurement of the particle correlations in momentum space [74]. The fundamental observable measured in femtoscopy is the correlation function $C(k^*)$. For simplicity, a two-body problem is considered.
The correlation function is expressed in terms of the relative distance between two final-state particles $\mathbf{r}^*$ and their reduced relative momentum, $k^* = \frac{|\mathbf{p}_2^* - \mathbf{p}_1^*|}{2}$ in the pair rest frame, with $\mathbf{p}_1^* = -\mathbf{p}_2^*$, by the Koonin–Pratt formula [75, 76]:

$$C(k^*) = \int S(\mathbf{r}^*) |\phi(\mathbf{r}^*, \mathbf{k}^*)|^2 d^3 r^*. \tag{1.24}$$

In Eq. 1.24, the first term, $S(\mathbf{r}^*)$, describes the source that emits the particles; the second term contains the information of the final-state interaction (FSI) through the two-particle wave function $\phi(\mathbf{r}^*, \mathbf{k}^*)$, from which it follows that the shape of the correlation function is determined by the characteristics of the source and by the sign (attractive or repulsive) and strength of the interaction.

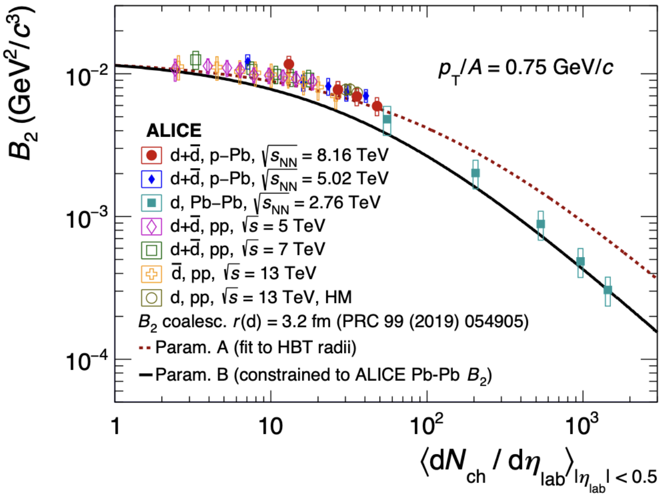

Figure 1.14: B_2 as a function of the mean charged-particle multiplicity density, $\langle dN_{ch}/d\eta_{lab}\rangle$, for a fixed value of $p_T/A = 0.75$ GeV$/c$. The experimental results are compared with coalescence model calculations from Ref. [42], performed using two different parameterizations of the system size as a function of $\langle \mathrm{d}N_{\mathrm{ch}}/\mathrm{d}\eta\rangle$ [73].

The effects of the interaction are primarily reflected in the correlation function at small values of k^*, where final-state interactions are most significant. In the absence of interactions, no correlations are present and the correlation function is equal to unity $C(k^*) = 1$.

A repulsive interaction, characterized by positive values of the local potential, leads to a correlation function with values between 0 and 1. For an attractive interaction, instead, the correlation function takes values greater than unity. This intuitive picture is modified, however, if the attraction is strong enough to support the formation of a bound state. In this case, a deviation of the correlation function, whose magnitude depends on the binding energy B_E, can be observed [77]. This deviation arises because the particles that form the bound state end up in a different final state and therefore do not contribute to $C(k^*)$.

The correlation strength is amplified by small source sizes, as discussed below. Other effects, not caused by the final-state interaction, can be visible at different k^* intervals of the correlation function, such as quantum-mechanical interference, resonance production, and conservation laws.

In Fig. 1.15, the sensitivity of the femtoscopic method to the study of the interaction in small colliding systems is illustrated, assuming an attractive, repulsive, or bound-state potential. In particular, looking at Fig. 1.15 on the right, one notes that the typical characteristics of attractive and repulsive interactions and the presence of a bound state are much more pronounced in the case of a small source size. For larger source sizes,

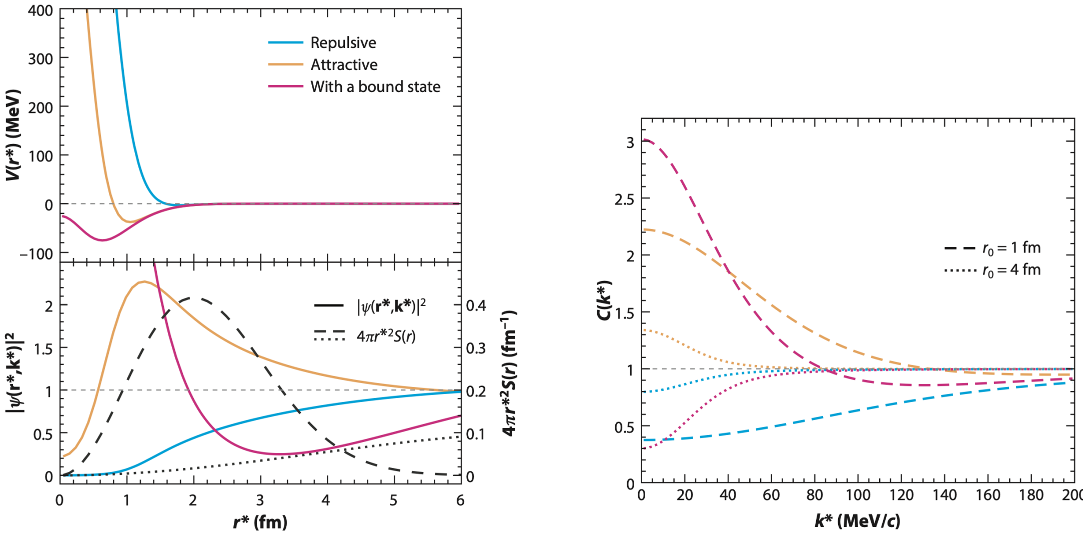

Figure 1.15: Top left: three examples of a potential $V(r^*)$: attractive in orange, repulsive in blue, and a potential with a bound state in pink. Bottom left: the squared modulus of the total wave functions, $|\psi(\mathbf{r}^*, \mathbf{k}^*)|^2$, as a function of the relative distance r^* for the three example potentials. The profile of the emitting source, assumed to be Gaussian, is shown in the same plot for 1 fm (black dashed line) and 4 fm (black dotted line). On the right, the resulting correlation function $C(k^*)$ is shown for each of the three interactions, evaluated for the two different source sizes, r_0 = 1 fm (dashed lines) and 4 fm (dotted lines) [78].

the correlation function becomes smoother and approaches unity, reflecting a reduced sensitivity to the details of the interaction. In the case of the bound state, the correlation function changes concavity, passing from above to below unity for different source sizes as a consequence of a very sharp peak present at small distances in the wave function, due to the much stronger localization of the bound state. This translates into a larger correlation for small radii, while for large radii only the asymptotic part of the wave function, which deflects due to probability conservation, affects the correlation function and brings it below one.

The method used to study the interactions between hadrons consists in comparing the theoretically expected correlation function with a correlation function obtained experimentally. The experimental correlation function [75] is obtained as the ratio between the distribution of the relative momentum of particle pairs produced in the same event (SE), which constitutes the sample of correlated pairs, and a reference distribution obtained by combining particles produced in different collisions, using the so-called mixed-event (ME) technique:

$$C(k^*) = \xi(k^*) \frac{N_{SE}}{N_{ME}}. \tag{1.25}$$

The corrections for experimental effects are denoted by $\xi(k^*)$ in Eq. 1.25. These corrections account for the finite experimental resolution, for adjustments to the mixed-event (ME) distributions to reproduce the same acceptance and event characteristics as in the same-event sample, and for the normalization. In general, ξ does not account for contributions from misidentification, weak decays, or residual background induced by mini-jets and event-by-event momentum conservation. These effects are taken into account when fitting the correlation functions.

The experimental correlation function is further distorted by two distinct mechanisms. The sample of particle pairs can include primary particles and secondary particles from hadrons that decay only weakly (we define resonances as those that undergo short-lived decays), introducing contributions from different pairs not originally correlated into the measured correlation function. The treatment of these contributions is described in detail in [79].

1.4.2 Determination of the nucleon source

After the collision between two protons and the completion of hadronisation processes, hadrons can undergo inelastic and elastic scatterings until their decoupling, after which they propagate freely to the detectors. We identify the source size as given by the distribution of spatial coordinates at which the various particles assume their momentum values.

In the simplest case one can assume that the source in pp and heavy-ion collisions is characterized by a Gaussian profile in one or three dimensions [75, 80]. The Gaussian profile of a one-dimensional source can be expressed as:

$$S(r^*) = \frac{1}{(4\pi r_0^2)^{3/2}} exp\left(-\frac{r^{*2}}{4r_0^2}\right) \tag{1.26}$$

where r_0 represents the source radius.

For the study of the formation of light nuclei, for example the deuteron, one needs to know the source of protons and neutrons. Neutrons are not measurable, but ALICE has demonstrated that the source of baryons is common [81], hence it is sufficient to measure the radius of the (anti)proton source via the correlation of $p - -p$ and $\overline{p}$–$\overline{p}$ pairs, respectively. The extraction of the numerical value of the radius r_0 starts from Eq. 1.24. Since $C(k^*)$ can be computed by constructing the samples of correlated pairs and subsequently applying Eq. 1.25, work that will be carried out in this thesis, the remaining ingredient is to compute the wave function ϕ.
To compute the wave function one can use the CATS framework [82], which allows one to solve the Schrödinger equation numerically given a known potential. The potential between (anti)protons is known, because it is the sum of the various potentials that make up the total interaction, namely:

- the potential associated with Pauli repulsion due to the fermionic nature of protons and antiprotons,
- the potential associated with the repulsive Coulomb interaction,
- the potential associated with the strong interaction.

CATS, acronym for *Correlation Analysis Tool using the Schrödinger equation*, is an analysis framework that makes it possible to find the wave function without any approximation by numerically solving the Schrödinger equation. It also allows the calculation of the correlation function for a two-particle femtoscopic system, for different functions describing the source profile and different interaction potentials. This framework is described in detail in [82].
Once the correlation function, the wave function and the analytical profile that models the emission source—that is, the Gaussian profile in Eq. 1.26—are known, the right-hand side of Eq. 1.25 becomes a function of r_0. In this way one can extract the value of r_0 through a fit of the measured correlation function using the CATS framework [82]. An example of the application of this procedure is visible in Fig. 1.16, where the correlation function for proton and antiproton pairs measured by the ALICE experiment in pp collisions at $\sqrt{s}$ = 13 TeV is shown. The proton sample includes both primary protons produced in the collision and those produced by strong resonance decays. The resulting interaction between protons is modelled using CATS [82], assuming Argonne v18 [35] as the strong-interaction potential and including the Coulomb interaction together with

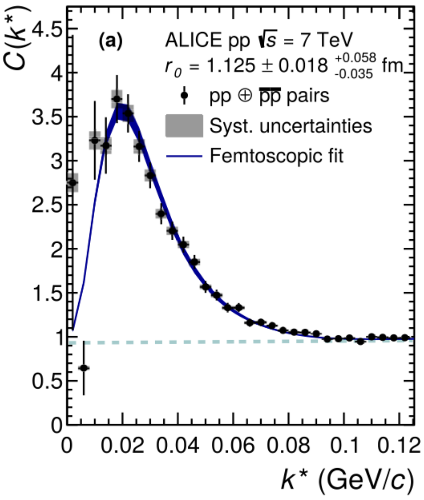

Figure 1.16: The plot shows the correlation function for proton and antiproton pairs measured in pp collisions at $\sqrt{s}$ = 13 TeV by the ALICE experiment at the LHC, for high-multiplicity events. The sample of (anti)protons includes those from strong resonance decays, while contributions from weak decays are excluded. In blue, the result of the fit to the correlation function is shown. The grey boxes represent the systematic uncertainty of the data [79].

the appropriate antisymmetrization of the wave function, to account for the fermionic nature of protons. The underlying strong interaction between protons is known with high precision and is accurately described by the Argonne v18 potential [35], enabling a reliable determination of the parameter r_0. As shown in Fig. 1.16, the data are well reproduced by the modelled correlation function. The same study was repeated by selecting different intervals of the proton-pair transverse mass m_T, and the extracted source size is shown in Fig. 1.17 [81]. When the analysis is repeated for different particle pairs and the known resonance contribution is subtracted in a model-driven way, it is found that the source is common to different baryons produced in the collision.

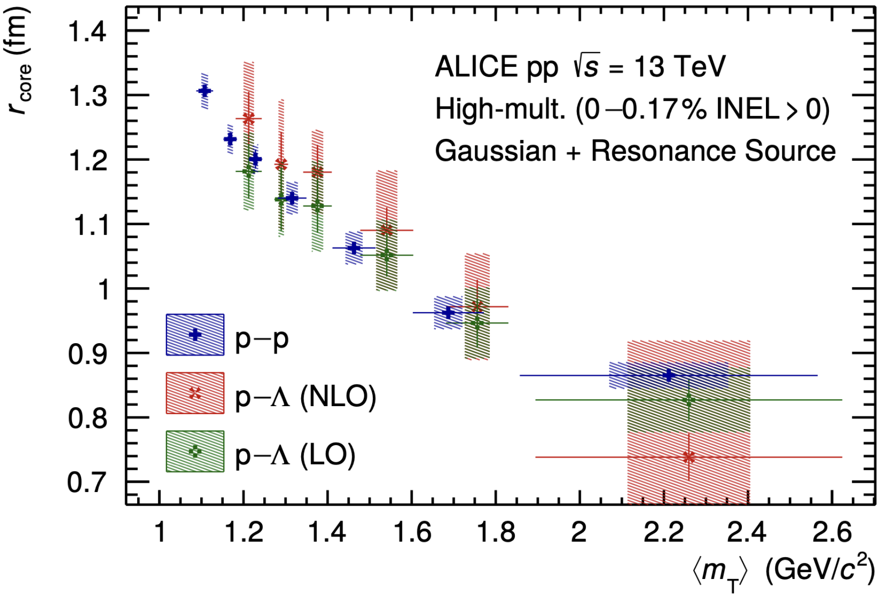

Figure 1.17: Source radius as a function of $\langle m_T \rangle$ for the hypothesis of a Gaussian source with added resonances. Note that r_{core} represents the source radius for the hypothesis of a Gaussian source with additional resonances. The blue crosses derive from the fit of the p–p correlation function with the Argonne v18 strong potential [35]. The green square crosses (red diagonal crosses) derive from the fit of the p–Λ correlation functions with the χEFT LO [83] (NLO [84]) strong potential. Statistical (lines) and systematic (boxes) uncertainties are shown separately [81].

Chapter 2

Light (anti)nuclei at Colliders Accelerators and Cosmic Rays

In this chapter, the experimental study of light (anti)nuclei production is reviewed, starting from measurements performed at accelerator facilities and extending to searches in cosmic rays. Results from collider and fixed-target experiments are discussed as a benchmark for antinucleus formation models, with particular emphasis on measurements carried out at the Large Hadron Collider (LHC) and at lepton colliders. The chapter then introduces cosmic rays and the ongoing experimental efforts to detect antinuclei in space, highlighting their relevance for dark matter searches and for the interpretation of rare antimatter signals.

2.1 Measurements at accelerators

The controlled environment of collider and fixed-target experiments has been crucial for establishing the experimental knowledge on light (anti)nuclei production. In high-energy hadronic interactions, antinuclei are produced with very small probabilities with respect to (anti)protons [20], typically suppressed by about three orders of magnitude for each added antinucleon. Nevertheless, modern detectors with excellent tracking and particle-identification capabilities have enabled precision measurements of light antinuclei, in particular (anti)deuterons and, more recently, heavier species such as (anti)^{3}He. These measurements provide an essential benchmark for microscopic formation models (e.g. coalescence, Sec. 1.3.2) and for thermal-statistical approaches (Sec. 1.3.1), and they are also a key ingredient for the interpretation of cosmic-ray antinuclei searches, where accelerator data are used to constrain production rates and reduce systematic uncertainties in background predictions [71, 85, 86].
From an experimental standpoint, accelerator results span several complementary initial

states and energy regimes. At the LHC, the A Large Ion Collider Experiment (ALICE) experiment has measured light (anti)deuteron production across multiple collision systems such as proton–proton (pp), proton–lead (p–Pb), and lead–lead (Pb–Pb) and center-of-mass energies, enabling systematic studies versus event activity and system size, and extending the programme towards rarer species such as antihelium with increased statistics in recent LHC runs [25, 87, 88, 89]. At lepton colliders, the ALEPH experiment at LEP provided an important measurement of deuteron and antideuteron production in $\mathrm{e}^+\mathrm{e}^-$ collisions at the Z resonance energy, offering a clean environment to test (anti)deuteron formation in a fragmentation-dominated regime [90]. At HERA, ZEUS reported the observation of (anti)deuterons in deep-inelastic ep scattering, allowing a study of (anti)deuteron production in a distinct kinematic configuration and providing additional constraints for coalescence-based interpretations [67]. Looking ahead, the future Electron–Ion Collider (EIC) will extend precision QCD measurements in ep and e–A collisions; in this context, light antinuclei measurements will have the potential to connect hadronisation studies to the nuclear degrees of freedom relevant for antinuclei formation [91].

2.1.1 The ALICE experiment at the LHC

ALICE is an experiment at the Large Hadron Collider (LHC) [92, 93] dedicated to heavy-ion collisions and is located at interaction point 2, approximately 56 m underground. It was proposed to study the properties of the strong interaction and to characterize the Quark–Gluon Plasma (QGP), a very hot and dense state of matter composed of deconfined quarks and gluons. The QGP is produced in high-energy heavy-ion collisions and is believed to have existed during the first moments of the evolution of the Universe [92].

The ALICE physics programme is not only devoted to the study of heavy-ion collisions, such as Pb–Pb interactions, but also includes pp and p–Pb collisions. Thanks to its particle identification systems and an excellent tracking system, ALICE is capable of measuring particles down to very low transverse momenta (p_T) in a high-multiplicity environment [92].

ALICE began operation in 2009, when the LHC Run 1 (2009–2013) started with pp collisions at a center-of-mass energy of $\sqrt{s} = 0.9$ TeV. During Run 1, pp collisions were also recorded at $\sqrt{s} = 2.76$, 7, and 8 TeV. The experiment collected more data during Run 2 (2015–2018), with pp collisions at $\sqrt{s} = 5.02$ and 13 TeV, together with p–Pb collisions at $\sqrt{s_{\mathrm{NN}}} = 5.02$ (Run 1) and 8.16 TeV and Pb–Pb collisions at $\sqrt{s_{\mathrm{NN}}} = 2.76$ (Run 1) and 5.02 TeV.

Following the Long Shutdown 2, ALICE entered Run 3 (2022–2026), operating with an upgraded detector and recording pp collisions at $\sqrt{s} = 13.6$ TeV. In addition, Pb–Pb collisions at a nucleon–nucleon center-of-mass energy of $\sqrt{s_{\mathrm{NN}}} = 5.36$ TeV were successfully collected during Run 3. These data significantly extend the available experimental sample for studies of strongly interacting matter and rare probes, including light (anti)nuclei.

The ALICE detector weighs approximately 10 000 tonnes and has dimensions of about 26 m in length and 16 m in both height and width. It is built with cylindrical symmetry around the beam pipes, as shown in Fig. 2.1. The beam axis defines the z-axis of the detector reference frame, while the transverse plane corresponds to the x–y plane. The detector is composed of several sub-detectors designed to characterize the main properties of the collision events. A central barrel, a forward Muon Spectrometer, and additional smaller detectors constitute the ALICE apparatus. The central barrel is located inside a large solenoidal magnet providing a uniform magnetic field of $B = 0.5$ T along the beam direction [92]. The magnet (in red Fig. 2.1), inherited from the former LEP experiment L3, surrounds the central barrel detectors and includes:

- the Inner Tracking System (ITS);
- the Time Projection Chamber (TPC);
- the Time-Of-Flight detector (TOF);
- the Transition Radiation Detector (TRD), used for track reconstruction and momentum determination of charged particles in the region $|\eta| < 0.9$, and for electron identification and pion background suppression;
- the Electromagnetic Calorimeter (EMCal), used to detect electrons and photons produced in heavy-flavor hadron decays and neutral mesons, and to provide trigger capabilities;
- the Photon Spectrometer (PHOS), a high-resolution electromagnetic calorimeter optimized for photon measurements;
- the High Momentum Particle Identification Detector (HMPID), a ring-imaging Cherenkov detector used to identify hadrons at high transverse momentum over a limited acceptance.

In the forward region, the Muon Spectrometer includes an absorber to suppress background contributions, tracking chambers located before, inside, and after a dipole magnet, and dedicated trigger chambers. Within its acceptance region, $-3.6 < \eta < -2.45$, the Muon Spectrometer allows for the identification of muons produced in hadronic decays with a pointing resolution of the order of 100 μm [36]. Finally, the Zero Degree Calorimeters (ZDC) are used to determine the collision centrality, while since Run 3 the Fast Interaction Trigger (FIT) system has been employed as interaction trigger, online luminometer, initial vertex indicator, and forward multiplicity counter [94].

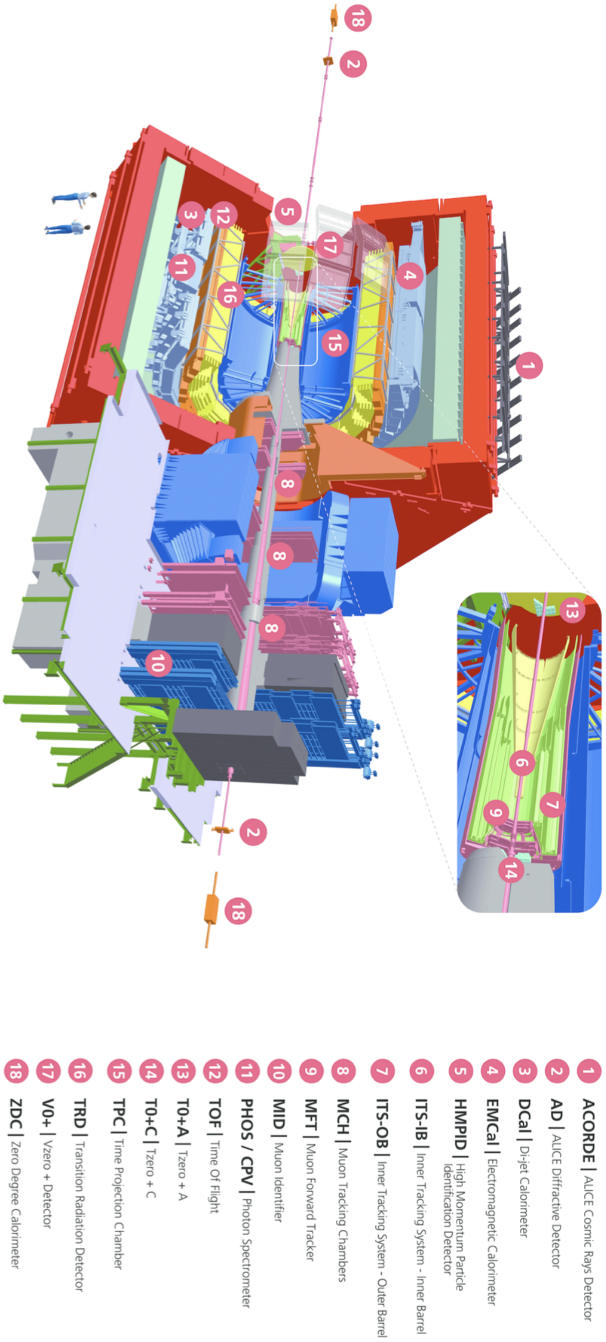

Figure 2.1: The ALICE detector during Run 3 [95].

The experimental characteristics described above make ALICE particularly well suited for the study of light (anti)nuclei production at accelerators. The measurement of composite objects such as antideuterons and heavier antinuclei requires an experimental setup capable of reconstructing charged particles with very low transverse momentum, providing precise momentum determination, and achieving robust particle identification in an environment dominated by lighter hadrons. Thanks to its excellent tracking performance, low material budget, and redundant particle-identification capabilities, ALICE fulfills all these requirements [92, 96].

In particular, the combination of specific energy-loss measurements in the Time Projection Chamber (TPC) and time-of-flight information from the TOF detector allows an unambiguous identification of light (anti)nuclei over a broad momentum range. An example of the separation power of the TPC for light nuclei and antinuclei is illustrated by the distinct $\mathrm{d}E/\mathrm{d}x$ bands shown in Fig. 2.2. The low material budget of the central barrel significantly reduces secondary interactions and absorption effects, which represent one of the dominant sources of systematic uncertainty in antinuclei measurements [20]. These features are essential for achieving high-purity antinucleus samples and for controlling background contributions from misidentified particles.

Moreover, the broad physics programme of ALICE enables investigations of light (anti)nuclei production across different collision systems and over a wide range of event multiplicities, from small systems such as pp collisions to large systems such as Pb–Pb collisions. This versatility allows systematic studies of antinucleus formation under varying source conditions, providing essential experimental constraints for coalescence-based and thermal-statistical models [25, 20]. Consequently, ALICE results represent the primary experimental benchmark in this field and play a crucial role in guiding theoretical interpretations and in supporting cosmic-ray antinuclei searches [20].

2.1.2 ALEPH experiment at LEP

The Large Electron–Positron Collider (LEP) at CERN featured $\mathrm{e}^{+}\mathrm{e}^{-}$ collisions at center of mass energies at the Z-mass resonance and up to $\sqrt{s} \simeq 209$ GeV, which provided a clean environment useful for precision physics in the study of hadron production and fragmentation. It was in the context of the LEP that the ALEPH experiment measured the production of deuteron and antideuteron in hadronic Z decays [90].

The ALEPH detector, shown in Fig. 2.3, featured a cylindrical geometry with full azimuthal coverage, optimized for precision tracking and calorimetry. Charged particle reconstruction was provided by an inner tracking system composed of a silicon vertex detector, an inner drift chamber and a large Time Projection Chamber (TPC), all immersed in a solenoidal magnetic field of 1.5 T. The TPC provides particle identification via $\mathrm{d}E/\mathrm{d}x$ measurements over a broad momentum range (2–50 GeV/c), with effective

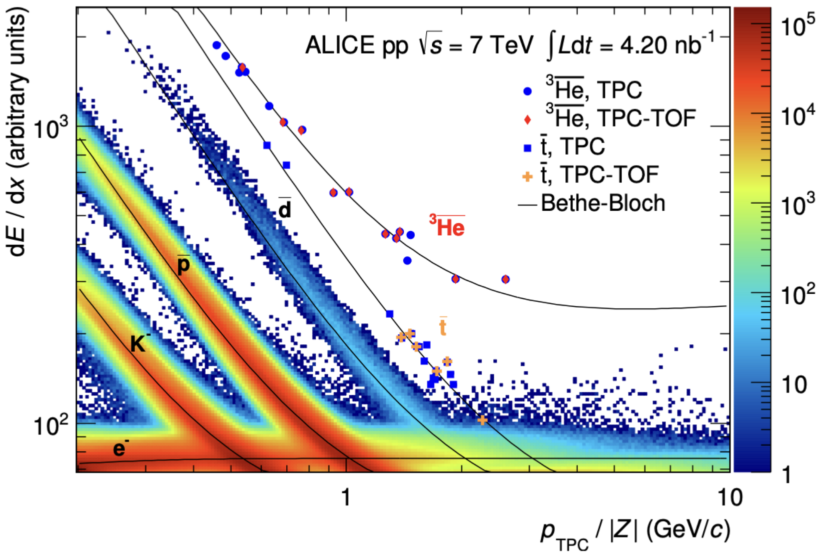

Figure 2.2: Specific energy loss $\mathrm{d}E/\mathrm{d}x$ measured in the ALICE TPC as a function of rigidity, showing the separation of light nuclei and antinuclei from lighter hadrons [20].

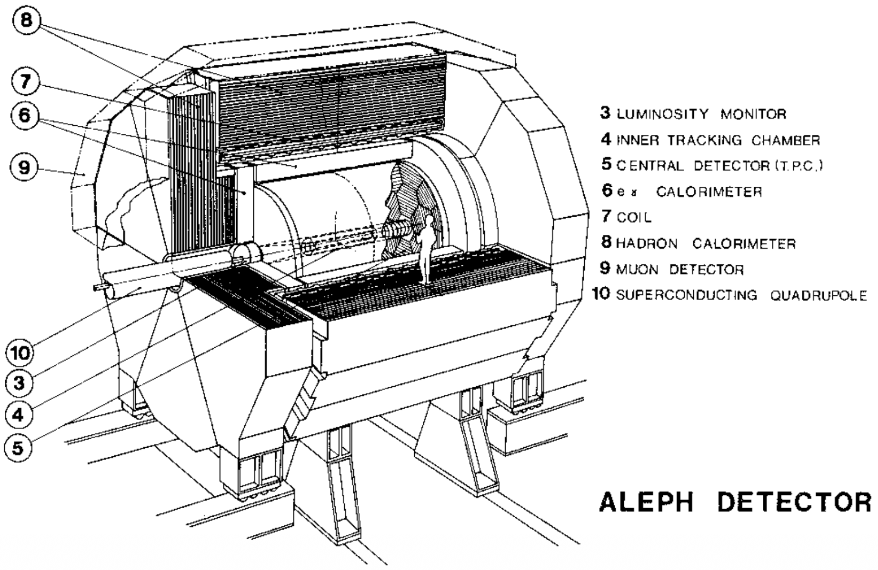

Figure 2.3: Schematic overview of the ALEPH detector at LEP [97].

e–π separation at the level of about 3 standard deviations for momenta below approximately 10 GeV/c [97]. Surrounding the tracking volume, electromagnetic and hadronic calorimeters provided energy measurements, while an outer muon system ensured efficient muon identification [97].

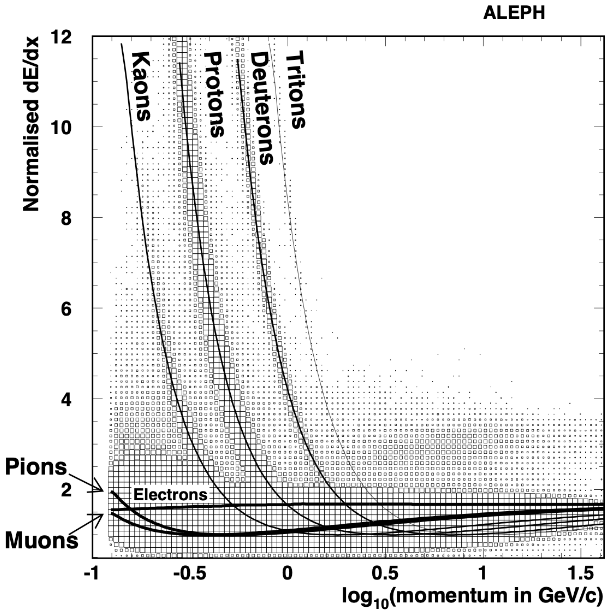

Figure 2.4: $\mathrm{d}E/\mathrm{d}x$ as a function of momentum for charged particles measured by ALEPH, illustrating the separation of deuterons (and antideuterons) from lighter hadrons [90].

The identification of light (anti)nuclei in ALEPH relied primarily on the measurement of $\mathrm{d}E/\mathrm{d}x$ in the TPC. Due to their different masses, (anti)deuterons could be clearly separated from lighter hadrons at low and intermediate momenta using the ionization energy loss, as shown in Fig. 2.4. This capability allowed ALEPH to reconstruct deuterons and antideuterons produced in hadronic Z decays with high purity [90].
ALEPH employed the coalescence framework introduced in Sec. 2, extracting the antinucleus formation probability through the coalescence parameter B (see Fig. 2.5). The ALEPH results represent an essential benchmark for testing coalescence models in elementary $\mathrm{e}^{+}\mathrm{e}^{-}$ collisions and for constraining the universality of antinucleus production mechanisms across different collision systems [90].

2.1.3 ZEUS experiment at HERA

The Hadron–Electron Ring Accelerator (HERA) collider at DESY provided electron–proton collisions up to a center-of-mass energy of $\sqrt{s} = 318$ GeV, enabling detailed studies of hadron production in a lepton–hadron environment. In this context, the

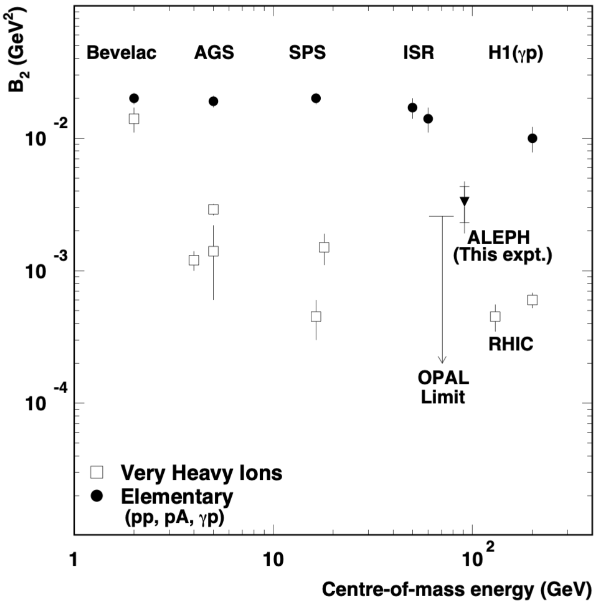

Figure 2.5: Values of the coalescence parameter B_2 measured in heavy-ion and elementary collisions, compared to the result from ALEPH in hadronic Z decays and to the OPAL upper limit [90]. For ALEPH the measurement is integrated over $0.62 < p < 1.03\,\mathrm{GeV}/c$, corresponding to $0.31 < p/A < 0.515\,\mathrm{GeV}/c$.

ZEUS experiment performed the first observation of (anti)deuteron production in deep-inelastic scattering (DIS) reactions [67].

The ZEUS detector [98], visible in Fig. 2.6, comprised a central tracking system immersed in a solenoidal magnetic field of 1.43 T and a high-resolution uranium–scintillator calorimeter. Charged-particle tracking and momentum reconstruction were provided by the Central Tracking Detector (CTD), covering the polar-angle range $15^\circ < \theta < 164^\circ$. The CTD also delivered measurements of the ionization energy loss, $\mathrm{d}E/\mathrm{d}x$, with a typical resolution of about 9% for full-length tracks, enabling particle identification at low and intermediate momenta up to 10 GeV/c [67]. The event kinematics and the scattered-lepton reconstruction were determined using the electromagnetic and hadronic calorimeter system, which consisted of forward, barrel, and rear sections and provided energy measurements. The magnetic field and tracking performance ensured sufficient momentum resolution to reconstruct heavy charged particles such as light (anti)nuclei [98].

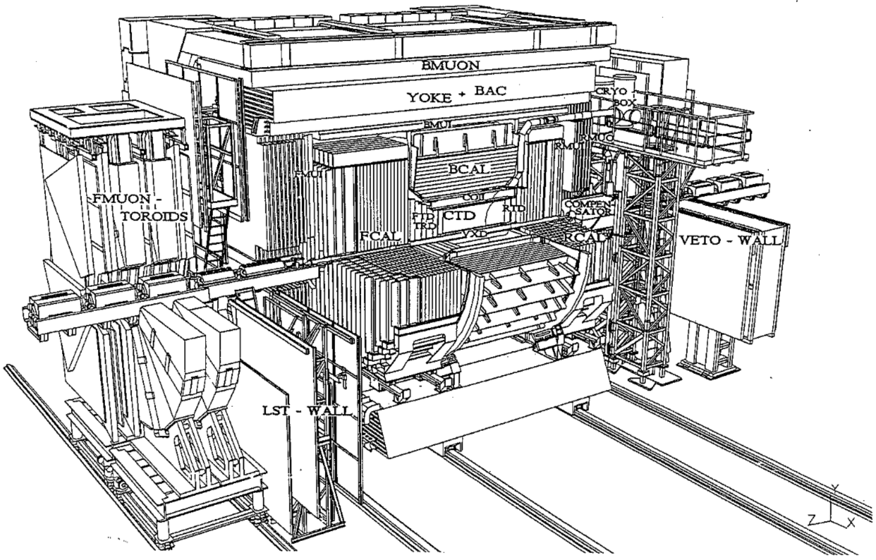

Figure 2.6: Schematic overview of the ZEUS detector at HERA [98].

In ZEUS (anti)deuterons were identified exploiting their characteristic large ionization energy loss, $\mathrm{d}E/\mathrm{d}x$, in the central tracking detector, allowing separation from lighter hadrons at low and intermediate momenta ($0.3 < p_T/M < 0.7$) [67], thanks to the different mass, as visible in Fig. 2.7. ZEUS measured deuterons and antideuterons in DIS events (typically requiring $Q^2 > 1\ \mathrm{GeV}^2$) and extracted the coalescence parameter B_2, introduced in Chap. 2, which expresses the formation probability of a deuteron and antideuteron. The B_2 observable is particularly useful for cross-system comparisons,

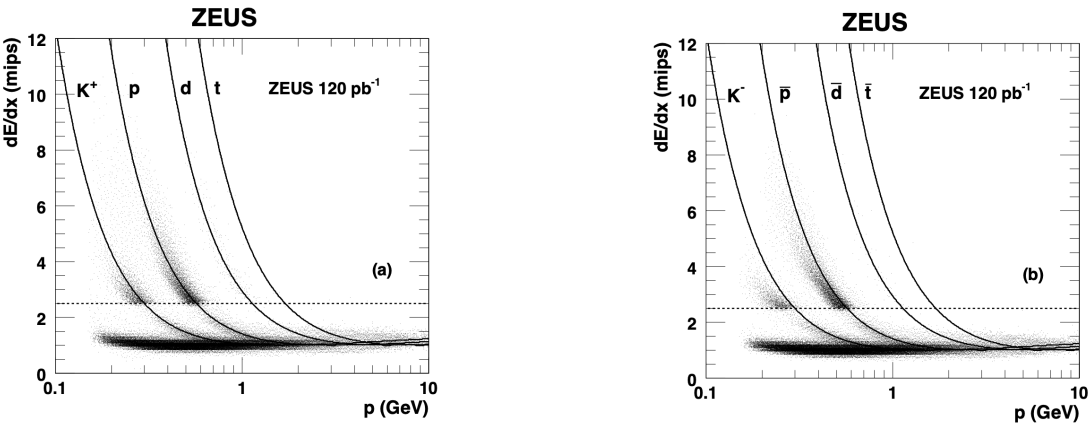

(a) Positive tracks

(b) Negative tracks

Figure 2.7: The dE/dx distributions as a function of track momentum for positive and negative tracks [67] in ZEUS.

since it is sensitive to the effective source conditions relevant for the formation of loosely bound states. The ZEUS results for the p_{T}/M dependence of B_2 in DIS, compared to those obtained in photoproduction events using a common analysis strategy [67], are shown in Fig. 2.8.

The ZEUS measurement provides an important reference point for light (anti)nucleus production in a collision system where the underlying event structure and hadronisation dynamics differ from those in hadron–hadron and nucleus–nucleus collisions. In particular, the comparison between DIS and photoproduction within the same experiment constrains the systematics of antideuteron formation in a fragmentation-dominated regime [67].

2.1.4 Electron–Ion Collider (EIC)

The Electron–Ion Collider (EIC) is a next-generation lepton–hadron collider planned for construction at Brookhaven National Laboratory (BNL) in the United States. The EIC will provide collisions of polarized electrons with polarized protons and light ions, as well as with heavier nuclei, over a broad range of center-of-mass energies, $\sqrt{s} \simeq 20$–100 GeV, with a possible upgrade up to $\sqrt{s} \simeq 140$ GeV. The design luminosity, reaching values of 10^{33}–$10^{34}\,\mathrm{cm}^{-2}\mathrm{s}^{-1}$, will exceed that of previous lepton–hadron facilities by orders of magnitude, enabling precision studies of Quantum Chromodynamics in both nucleons and nuclei [91].

The EIC physics programme is primarily focused on studying the internal structure of

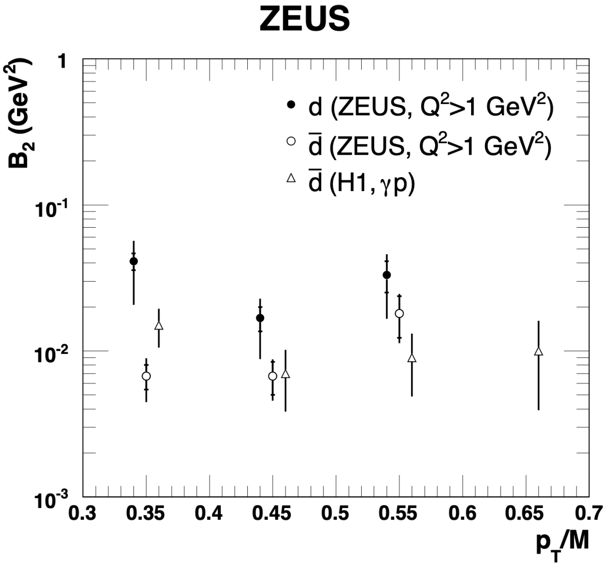

Figure 2.8: The p_{T}/M dependence of the coalescence parameter B_2 for deuterons and antideuterons in DIS and photoproduction as measured by ZEUS at HERA at $\sqrt{s} = 318$ GeV, based on an integrated luminosity of 120 pb^{-1} [67].

hadrons and nuclei in terms of quarks and gluons, including the origin of the nucleon mass and the spin, three-dimensional partonic imaging, and the dynamics of color charge in cold nuclear matter. The collider will operate in a kinematic regime intermediate between fixed-target deep-inelastic scattering experiments and high-energy hadron colliders, providing a unique environment for the study of hadronisation and fragmentation processes in lepton–ion collisions [91].

The experimental programme foresees at least one multi-purpose detector with nearly full solid-angle coverage, optimized for precision tracking, vertexing, electron and hadron identification, and calorimetry over a wide rapidity range [91]. The ePIC detector concepts, visible in Fig. 2.10 (a), include high-resolution silicon vertex detectors, large-acceptance tracking systems embedded in solenoidal magnetic fields, and advanced particle-identification subsystems based on time-of-flight measurements, Cherenkov detectors, and calorimetry. Dedicated forward and backward detector regions are designed to ensure efficient reconstruction of the scattered electron and the hadronic final state, even at low momentum transfer [91]. In particular, the dual Ring Imaging Cherenkov (dRICH) detector, visible in Fig. 2.10 (b), is designed to provide precise particle identification in the forward region of the future ePIC experiment at the Electron-Ion Collider. By combining aerogel and gas radiators with silicon photomultiplier sensors, it achieves more than 3σ pion–kaon separation up to about 50 GeV/c [100] within the pseudorapidity region $1.5 < \eta < 3.5$, thus meeting the stringent PID requirements of

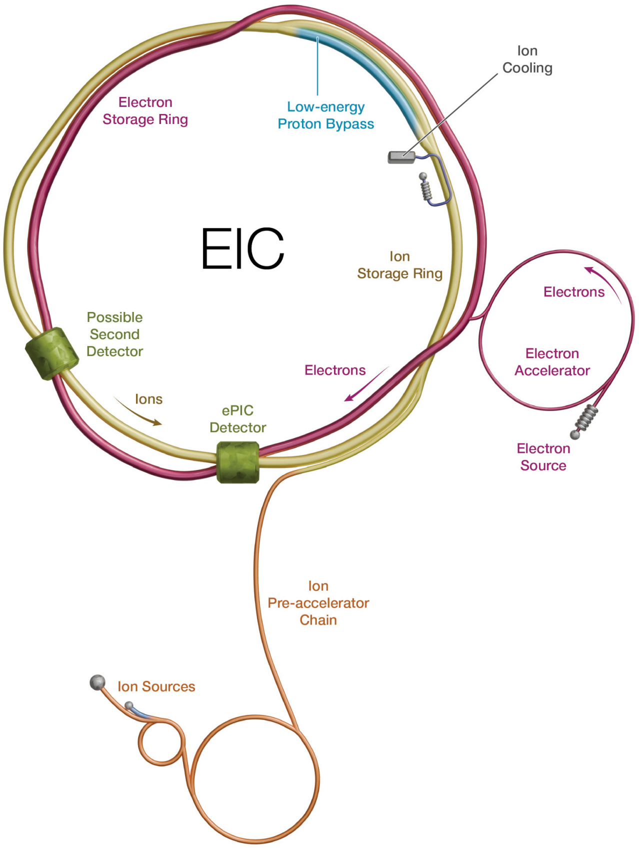

Figure 2.9: Schematic overview of the planned Electron–Ion Collider facility [99].

the EIC physics programme.

The construction of the EIC builds upon the existing RHIC infrastructure. Construction is beginning now, with the goal of being fully operational in the early 2030s. From a physics perspective, measurements of light (anti)nuclei production at the EIC would provide a natural extension of existing results from $\mathrm{e^+e^-}$, ep, and hadronic collision systems. In particular, they would enable the investigation of antinucleus formation in a fragmentation-dominated regime, offering sensitivity to coalescence mechanisms (see Sec. 2) in cold nuclear matter and to the space–time structure of hadronisation in deep-inelastic scattering [91].

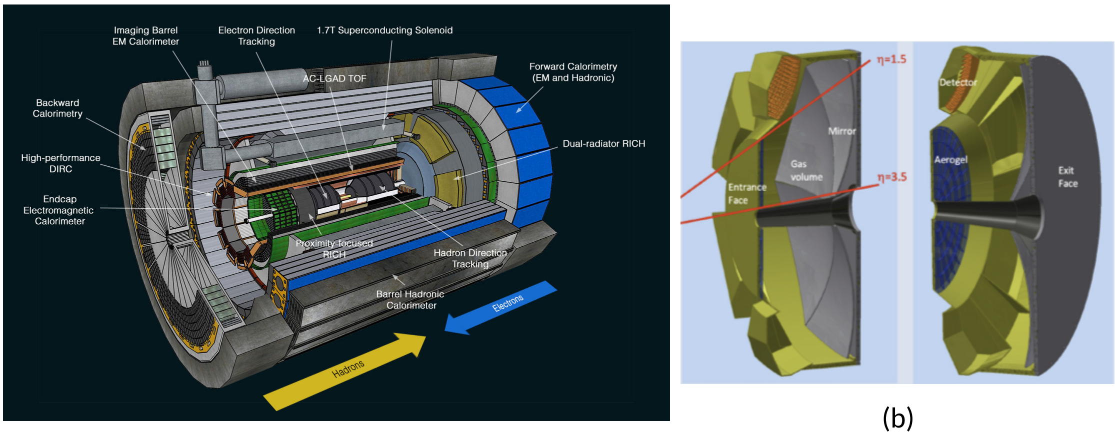

(a) (b)

Figure 2.10: (a) ePIC detector scheme [91], (b) dRICH 3D CAD model [100]

2.2 Cosmic Rays and the Search for Antinuclei

At the beginning of the 20th century, the nature of the penetrating radiation observed in the atmosphere was still unknown. In 1912, Victor Hess addressed this by performing a series of balloon flights equipped with an electroscope, demonstrating that the intensity of ionizing radiation increased with altitude. This result proved that the radiation did not originate from terrestrial sources such as natural radioactivity, but instead had an extraterrestrial origin, leading to the term cosmic rays. Since then, cosmic rays (CRs) have been extensively studied, and their composition, energy spectra, and propagation properties are now relatively well understood.

The observation of antimatter in cosmic rays has since developed into a mature field, with precision measurements of positrons and antiprotons performed by balloon-borne and space-borne experiments. In contrast, the search for antinuclei (i.e. composite antimatter states heavier than the antiproton) remains one of the most challenging frontiers of charged-particle astroparticle physics [101].

From a phenomenological perspective, antinuclei observed near Earth can be produced as secondary particles through hadronic interactions of primary cosmic rays, predominantly protons and helium nuclei, with the interstellar matter (ISM), which is itself mainly composed of hydrogen and helium [102, 103]. Because antinucleus formation requires the simultaneous production of multiple antinucleons in a single interaction, followed by their fusion into a loosely bound state, the resulting yields are strongly suppressed relative to those of single antinucleons. In particular, the production of antideuterons and antihelium nuclei involves both high kinematic thresholds and an additional coalescence penalty, leading to fluxes typically suppressed by a factor of 10^3–10^4 compared to the antiproton flux [101, 104].
This strong suppression makes the experimental search for cosmic antinuclei especially compelling. At low kinetic energy per nucleon, where solar modulation and propagation effects significantly reshape cosmic-ray spectra [102, 103], scenarios beyond purely secondary production predict a comparatively enhanced antinuclei component, while the expected astrophysical background remains extremely small [101, 102]. In particular, extensions of the Standard Model of particle physics allow for the production of antimatter through dark matter annihilation or decay, giving a fundamentally new significance to the observation of cosmic antinuclei [85].

Experimentally, the search for cosmic-ray antinuclei is carried on by instruments designed to cope with extremely low expected fluxes and stringent background-rejection requirements. Past and current searches have been carried out mainly by balloon-borne and space-borne experiments such as BESS and AMS-02, which directly measure the charged cosmic-ray flux near Earth and perform event-by-event identification of antinuclei using redundant determinations of charge sign, rigidity, velocity, and mass [105, 106]. In parallel, dedicated detection concepts such as the GAPS, ADHD experiment [107] have been developed to optimize sensitivity in the low kinetic-energy region, where the antinuclei signal is expected to be most prominent and experimental backgrounds are strongly suppressed [108].

2.2.1 Dark Matter searches

A wide set of astrophysical and cosmological observations indicate that most of the matter content of the Universe is not made of baryons, but of a non electromagnetically interacting component commonly referred to as Dark Matter (DM), indirectly through its

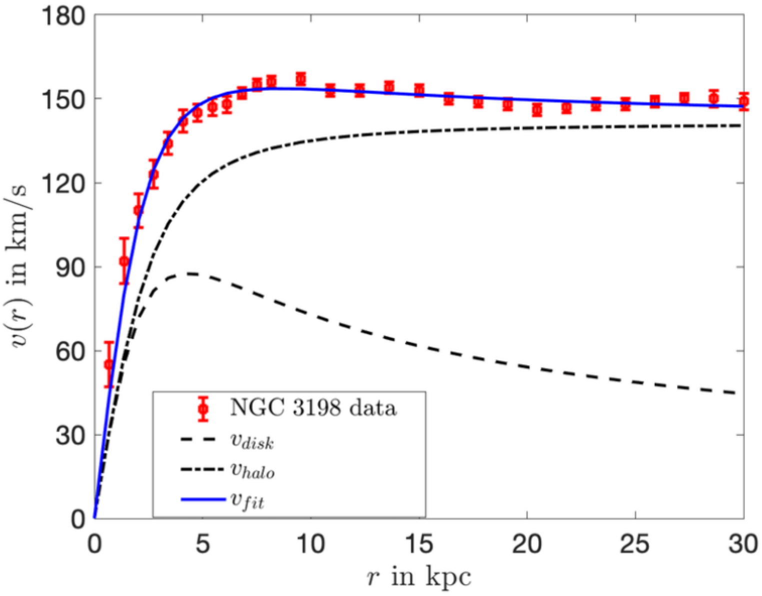

Figure 2.11: Rotation curve example illustrating the need for a non-luminous mass component to reproduce the observed circular velocity at large radii. Adapted from a classic rotation-curve measurement [111].

gravitational effects on ordinary matter [109, 110]. Historically, direct indications came from the dynamics of galaxies: the observed rotation curves remain approximately flat at large radii, which imply the presence of an extended mass distribution well beyond the visible disk [111]. As it can be seen in Fig. 2.11, the measured rotational velocity profile cannot be reproduced by the visible components alone. The DM hypothesis is supported by multiple and independent probes, including gravitational lensing, the dynamics of galaxy clusters, and the precise determination of the matter density from the Cosmic Microwave Background (CMB) anisotropies [110].
From a particle-physics perspective, the existence of Dark Matter implies the presence of new degrees of freedom beyond the Standard Model. Among the various candidates proposed, Weakly Interacting Massive Particles (WIMPs) [112] are often considered as a reference scenario for indirect searches. In this framework, Dark Matter particles may annihilate or decay into Standard Model states, potentially giving rise to observable signatures in cosmic rays. The identification of such signatures requires a careful understanding of astrophysical backgrounds and of the transport of charged particles in the Galaxy.

WIMPs may interact with Standard Model particles via new mediators or via effective operators, and can annihilate (or, in alternative scenarios, decay) into Standard Model final states [112]. Depending on the dominant couplings, annihilation channels can involve quarks, gauge bosons, leptons, or Higgs states. Hadronic channels in particular lead to the production of antiprotons, antineutrons, and mesons through parton showering and hadronisation. A schematic overview of the typical annihilation chains and the resulting messengers relevant for indirect searches is shown in Fig. 2.12. While the underlying microscopic interaction is model-dependent, the key experimental point is that any DM contribution to charged cosmic rays must be identified on top of astrophysical backgrounds generated by known non exotic sources, standard acceleration and propagation mechanisms.

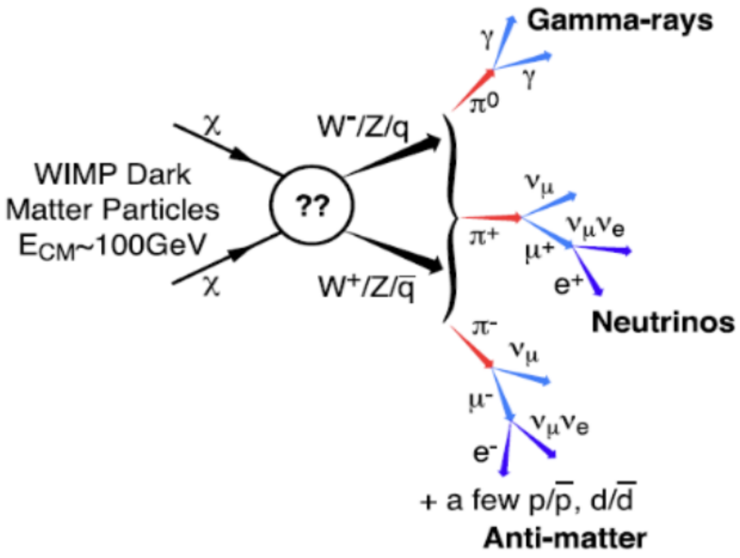

Figure 2.12: Possible WIMP annihilation channels into Standard Model particles and the resulting indirect messengers (photons, neutrinos, and antimatter) [113].

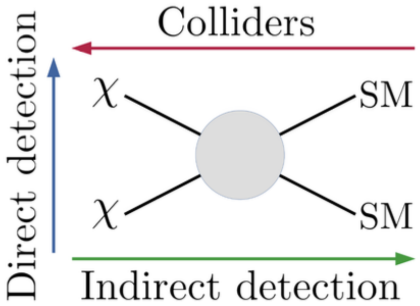

Figure 2.13: Complementarity of direct detection, indirect detection, and collider searches for particle DM [114]).

The investigation of dark matter can be pursued through several complementary approaches, as schematically illustrated in Fig. 2.13. Direct detection experiments aim to observe the interaction between dark matter particles and ordinary matter using two primary techniques. The first relies on large detectors consisting of tanks filled with hundreds of liters of a noble element in the liquid phase (such as xenon or argon). In this case, a collision between a dark matter particle and an atomic nucleus of the liquid induces the emission of a flash of light. The second technique employs absorptive crystals (for instance, germanium), in which the interaction releases energy that is detected as a small increase in temperature. In both approaches, the signals of interest are microscopic and extremely rare. Consequently, experiments of this type must be strongly shielded from external sources of background, in particular cosmic rays, which can traverse the detectors and produce spurious signals. For this reason, underground laboratories have been constructed to achieve a high level of shielding, like for example the Laboratori Nazionali del Gran Sasso (LNGS) with the XENONnT detector [115].

An alternative strategy is pursued at high-energy colliders such as the LHC, where dark matter particles could be produced through collisions of known particles, in a manner analogous to the production of the Higgs boson in proton–proton interactions. Since dark matter particles interact only weakly with ordinary matter, their presence would be inferred from a large imbalance in transverse momentum in proton–proton collisions.
Indirect detection of dark matter, instead, exploits the possibility that dark matter particles may annihilate, in analogy with ordinary matter, producing secondary particles such as gamma rays, charged particles (electrons, positrons, etc.), and neutrinos. These products contribute to cosmic radiation of astrophysical origin, although they are expected to be subdominant. Nevertheless, the search for stable antiparticles in cosmic radiation represents a promising avenue for identifying a potential dark matter signal.
Antimatter, in fact, is significantly less abundant than primary cosmic radiation, and recent results obtained by experiments such as HEAT [116], PAMELA [117], and AMS-02 [118], and shown in Fig. 2.14, have revealed an excess of positrons in the cosmic-ray spectrum [109]. Many models of dark matter annihilation or decay are able to naturally reproduce the observed increase in the positron fraction (green curve in Fig. 2.14), although this typically requires annihilation cross sections that are much larger than those predicted. Alternative explanations have also been proposed; as illustrated in Fig. 2.14, the contribution of a nearby pulsar (red curve) or modifications to current models of cosmic-ray propagation (blue curve) could account for both the positron excess and the observed electron spectrum [119].
It should be emphasized that antimatter plays a crucial role not only in the context of dark matter searches, but also because the apparent dominance of matter over antimatter in the Universe represents one of the major open questions in cosmology and particle physics.

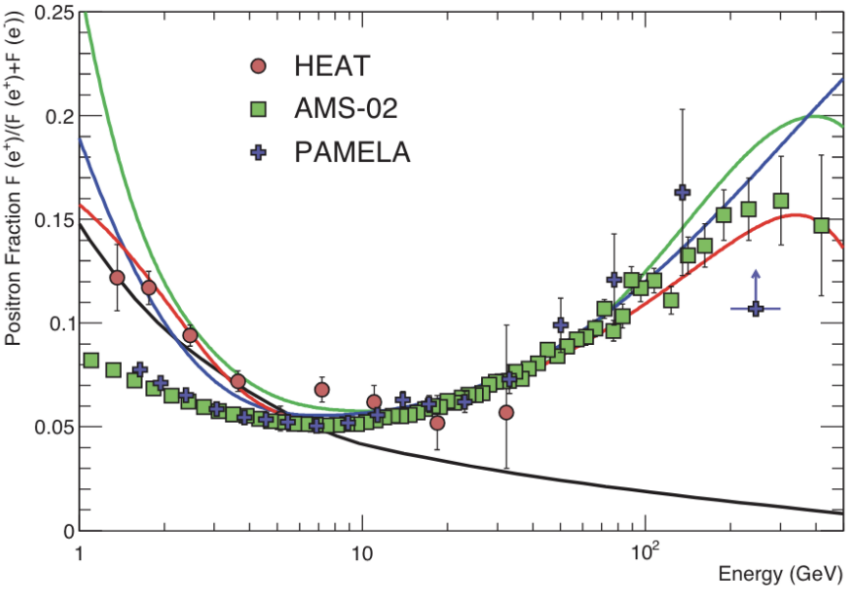

Figure 2.14: The positron fraction as a function of the particle kinetic energy in cosmic rays measured by HEAT, PAMELA, and AMS-02. The solid black line is a model of pure secondary production, and the three colored thin lines show three representative attempts to model the positron excess with different phenomena: green is for dark matter decay, blue is for propagation physics, red is for production in pulsars. The ratio below 10 GeV depends on the polarity of the solar magnetic field [119].

2.2.2 Cosmic antinuclei as an indirect probe of Dark Matter

Research on dark matter through the observation of positrons or gamma rays relies on the identification of a small excess over other relevant astrophysical sources, which constitute a substantial background. This circumstance poses significant challenges in the extraction of a possible dark matter signal. The case of antiprotons, measured by experiments such as BESS [120], PAMELA [121], and AMS-02 [122], is similarly demanding, since the observed flux is compatible with several theoretical models that predict sources unrelated to dark matter. Nevertheless, these measurements allow stringent constraints to be placed on scenarios of astrophysical production and propagation. In this paragraph, however, we focus on a different aspect of dark matter investigations: cosmic antinuclei.

Antinuclei represent an extremely promising probe for dark matter searches because, in contrast to positrons or antiprotons, they are characterized by a very low background from astrophysical processes at low energies. As discussed at the beginning of this section, although several astrophysical mechanisms can produce antimatter, antinuclei formation requires specific threshold energies and occurs only rarely through secondary cosmic-ray (CR) interactions with the interstellar medium. As shown in Fig. 2.15 [85], a potential dark matter (DM) signal is expected to dominate at low kinetic energy per nucleon ($T/n \lesssim 1$ GeV), while the secondary CR background peaks in the 1–10 GeV/n range. The large uncertainty bands in the figure reflect the significant modeling uncertainties related to CR sources and propagation, which remain a major limitation in predicting the secondary antinuclei flux. Consequently, the potential observation of cosmic antinuclei would constitute an unambiguous signature of new physics.

The most stringent experimental limits on cosmic antinuclei have been set by the BESS Collaboration. Using BESS-Polar II [123], a high-precision measurement of the low-energy antiproton spectrum below 1 GeV was achieved. No antideuteron candidate events were observed; however, combining its missions, BESS established an upper limit on the antideuteron flux of $\Phi_{\bar{d}} < 5.5 \times 10^{-5}\,\mathrm{m}^{-2}\,\mathrm{sr}^{-1}\,(\mathrm{GeV/n})^{-1}$ [124]. The antihelium search resulted in a new upper limit on the antihelium-to-helium ratio of 6.9×10^{-8} at 95% confidence level, representing the most stringent constraint to date [124].
Beginning with the first BESS [125] (Balloon-borne Experiment with Superconducting Spectrometer) balloon flight in 1993, the Collaboration carried out a total of 11 balloon missions, including two long-duration flights over Antarctica, with the last flight taking place in 2008. The original BESS-Polar experiment was flown over Antarctica in late 2004, followed by the BESS-Polar II mission, which collected data during 24.5 days between December 2007 and January 2008. The detector featured a coaxial cylindrical geometry with a geometric acceptance of 0.23 m^2sr and consisted of a 0.8 T solenoidal magnet housing inner drift chambers (IDC) and a jet-type drift tracking chamber (JET), together with an aerogel Cherenkov counter and a time-of-flight system. Details of the

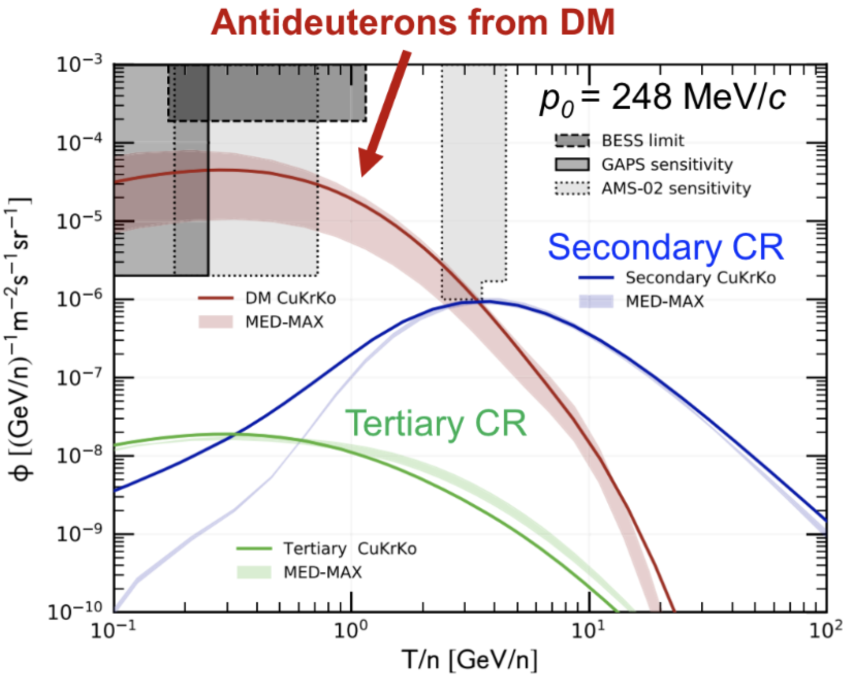

Figure 2.15: Comparison between the expected flux originating from dark matter interactions and the flux produced by cosmic rays interacting with the interstellar medium as a function of the kinetic energy per nucleon. The red solid line represents the dark matter (DM) contribution, while the blue solid line shows the secondary cosmic-ray component and the green solid line the tertiary component. The shaded bands around each curve represent the uncertainties associated with cosmic-ray propagation parameters in the Galaxy. The gray shaded boxes indicate current experimental limits and projected sensitivities of future or ongoing experiments. The arrow highlights the energy region where the dark matter signal is expected to dominate over the secondary background. It can be observed that below 1 GeV/n the red curve dominates over the blue one [85].

apparatus are shown in Fig. 2.16.

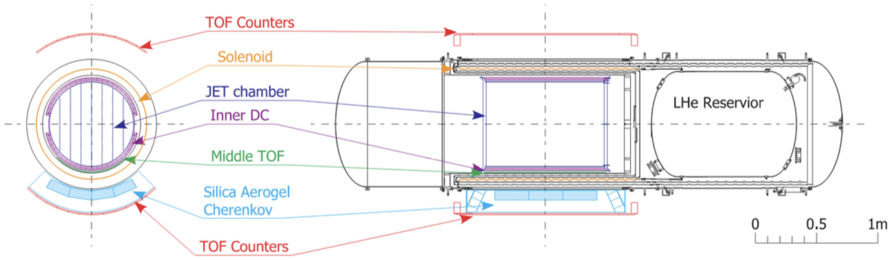

Figure 2.16: The BESS-Polar II experiment. From: [101].

In more recent years, the search for cosmic antinuclei has been continued by AMS-02, currently operating on the International Space Station. Thanks to AMS-02, the most precise measurement of the antiproton spectrum to date has been achieved in the energy range from 1 to 450 GeV [126]. In 2018, the Collaboration also reported a small number of candidate events compatible with antihelium nuclei, namely six $\overline{^3\mathrm{He}}$ and two $\overline{^4\mathrm{He}}$ candidates [127]; however, these events have not yet been independently confirmed.

Installed on the International Space Station in May 2011 [106, 122, 128], AMS-02 is a solenoidal magnetic spectrometer designed to measure charged cosmic-ray spectra over a wide energy range, up to the TeV scale, and to detect high-energy photons with energies of a few hundred GeV. It also investigates the nuclear component of cosmic rays and searches for indirect signatures of dark matter.

As illustrated in Fig. 2.17, AMS-02 consists of several sub-detectors. The Transition Radiation Detector rejects low-mass particles such as electrons, pions, and kaons and determines the relativistic Lorentz factor γ. The time-of-flight (ToF) system measures particle velocity (up to $\beta \simeq 0.8$) and provides the trigger for the experiment. The particle momentum is reconstructed using the 0.15 T magnetic field, while at high velocities particle identification is further improved by a proximity-focusing Ring Imaging Cherenkov (RICH) detector employing a dual-radiator configuration of silica aerogel and sodium chloride.

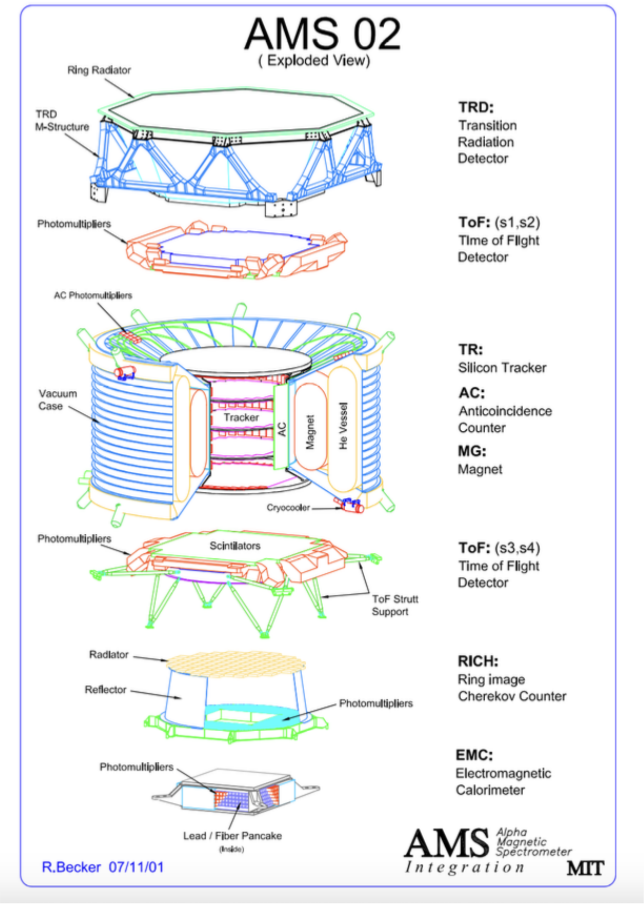

Figure 2.17: Schematic overview of the AMS-02 experiment [129].

Chapter 3

Modelling N–N Interaction and Coalescence

To investigate final-state correlations and nuclei production, a model must be established that describes both nucleon–nucleon (N–N) interactions (which do not result in a bound state) and coalescence (which instead leads to the formation of a nuclear bound state). In this chapter, a model capable of satisfying this requirement is implemented as an afterburner to be coupled with an event generator (e.g., PYTHIA). The afterburner can simultaneously treat coalescence and N–N interactions within two formalisms: the wave function formalism and the Wigner formalism. Such an afterburner is developed in a way similar to [130], which has been proven successful in reproducing ALICE data.

This chapter first introduces a wave function–based description of the source and the deuteron bound state. From this framework, the coalescence probability is derived via the scalar product of the corresponding wave functions and subsequently applied to the production of nuclei up to $A = 4$, including the associated treatment of photon emission.
Within this framework, a semiclassical treatment of the N–N interaction is implemented by comparing the initial energy of the system with the final asymptotic energy. Specific attention is paid to the treatment of the initial kinetic energy to ensure consistency with the kinematic input from the event generator. An alternative formulation based on Wigner functions is then presented, in which both the source and the bound state are described in phase space, and the coalescence probability is computed accordingly.
Finally, the event-generator configurations used as input to the afterburner are discussed.

3.1 Coalescence model

The model describing coalescence has been developed within two formalisms: a wave function–based formalism and a Wigner function–based formalism.

3.1.1 Coalescence in a wave function–based model

To provide a quantitative description of bound-state formation starting from correlated nucleon pairs produced in high-energy collisions, the wave function formalism is employed. Both the emitting source and the nuclear bound state are described quantum mechanically, and the coalescence probability is given by the scalar product of the wave functions.

Within this approach, the source emitting the nucleon pair is modelled as a Gaussian distribution in coordinate space, as in [130], and it is additionally modulated by a plane-wave factor that encodes the relative momentum of the pair,

$$\psi_{\text{src}}(\vec{r}, \vec{k}^*) = A \exp\left(-\frac{r^2}{2R_0^2}\right) \exp\left(i\frac{\vec{k}^* \cdot \vec{r}}{\hbar}\right), \tag{3.1}$$

where R_0 is the fixed source radius, A is the normalization constant, $\vec{r}$ is the position vector, $\vec{k}^* = \frac{|\vec{p_1} - \vec{p_2}|}{2}$ is the relative momentum of the particle pair in their rest frame, and $r = |\vec{r}|$.
The plane-wave factor $\exp\left(i\frac{\vec{k}^* \cdot \vec{r}}{\hbar}\right)$, which was neglected in [130], gives the wave function a preferred direction and wavelength (momentum) and is necessary for $k^* \neq 0$, while the Gaussian envelope $A\exp\left(-\frac{r^2}{2R_0^2}\right)$ confines it to a finite source region.
The normalization constant A is obtained by imposing

$$\int |\psi_{\text{src}}(\vec{r})|^2 \, d^3r = 1, \tag{3.2}$$

and the squared modulus is

$$|\psi_{\text{src}}(\vec{r})|^2 = |A|^2 \exp\left(-\frac{r^2}{R_0^2}\right). \tag{3.3}$$

Equation 3.2, evaluated in spherical coordinates, gives

$$|A|^2 = \frac{1}{(8\pi R_0^2)^{3/2}} \quad \Rightarrow \quad A = \frac{1}{(8\pi R_0^2)^{3/4}}. \tag{3.4}$$

The deuteron S-state wave function[1]is modeled starting from a square-well potential

$$V(r) = -V_0\,\Theta(R_D - r), \tag{3.5}$$

where $\Theta(x)$ is the Heaviside step function, and R_D is a fixed deuteron radius, while V_0 is the depth of the square well, fixed such that the resulting binding energy matches the measured value $E_{BE} \approx 2.2$ MeV. Solving the Schrödinger equation with the potential in Eq. 3.5 leads to the ground-state (S-wave) function:

$$\psi_{\text{deut}}(\vec{r}) = \frac{u(r)}{r} Y_{00}(\theta, \phi), \tag{3.6}$$

where $u(r)$ is given by

$$u(r) = \begin{cases} \mathcal{N}\sin(kr), & \text{for } r < R_D, \\ \mathcal{N}\sin(\kappa R_D)\, e^{-\kappa(r-R_D)}, & \text{for } r \geq R_D, \end{cases} \tag{3.7}$$

where $k = \sqrt{\frac{2\mu(V_0 - |E_{BE}|)}{\hbar}}$ and $\kappa = \sqrt{\frac{2\mu|E_{BE}|}{\hbar}}$, with E_{BE} being the binding energy and μ the reduced mass. $\mathcal{N}$ is the normalization constant determined by

$$\int_0^\infty |u(r)|^2\, dr = 1, \tag{3.8}$$

and $Y_{00}(\theta, \phi)$ is the spherical harmonic with quantum numbers $\ell = 0$ and $m = 0$, given by

$$Y_{00}(\theta, \phi) = \frac{1}{\sqrt{4\pi}}. \tag{3.9}$$

The coalescence probability is then given by the projection of the source wave function onto the deuteron ground state:

$$P_{\text{coal}}(k^*) = \left| \langle \psi_{\text{src}}(\vec{r}, \vec{k}^*) \mid \psi_{\text{deut}}(\vec{r}) \rangle \right|^2 = \left| \int \psi_{\text{deut}}(\vec{r})\, \psi_{\text{src}}(\vec{r}, \vec{k}^*)\, d^3r \right|^2 . \tag{3.10}$$

3.1.2 Coalescence in a Wigner function formalism

An alternative implementation of the coalescence model has been developed in the afterburner, based on Wigner functions, which are quasi-probability distributions in

---

[1] An S-state wave function is a quantum state with orbital angular momentum equal to 0.

phase space defined over the real field and that completely describe a quantum state. A generic Wigner function for a particle pair can be defined as

$$W(\vec{r},\vec{p}) = \frac{1}{(2\pi\hbar)^3}\int \phi^*\left(\vec{r}+\frac{\vec{s}}{2}\right)\phi\left(\vec{r}-\frac{\vec{s}}{2}\right)\exp\left(-\frac{i\vec{p}\cdot\vec{s}}{\hbar}\right)d^3s, \tag{3.11}$$

where ϕ is a wave function for the given quantum state.
In our case, the Wigner function of the source, W_{src}, is obtained by imposing $\phi = \psi_{\text{src}}$ from Eq. 3.1, which results in

$$W_{\text{src}}(\vec{r},\vec{p}) = \frac{1}{(2\pi\hbar)^3}\exp\left(-\frac{r^2}{4R_0^2}\right)\exp\left[-\frac{4R_0^2}{\hbar^2}\left(\vec{k}^*+\vec{p}\right)^2\right]. \tag{3.12}$$

Equation 3.33 is Gaussian in both coordinate and momentum space, with inversely proportional widths, $\sigma_r = \hbar/\sigma_{k^*}$.

The Wigner function of the deuteron S-state, W_{deut}, is computed by imposing $\phi = \psi_{\text{deut}}$ from Eq. 3.6 into Eq. 3.11. The calculation has not been carried out analytically, but numerically. The results for a deuteron radius $R_D = 3.2$ fm are shown in Fig. 3.1.

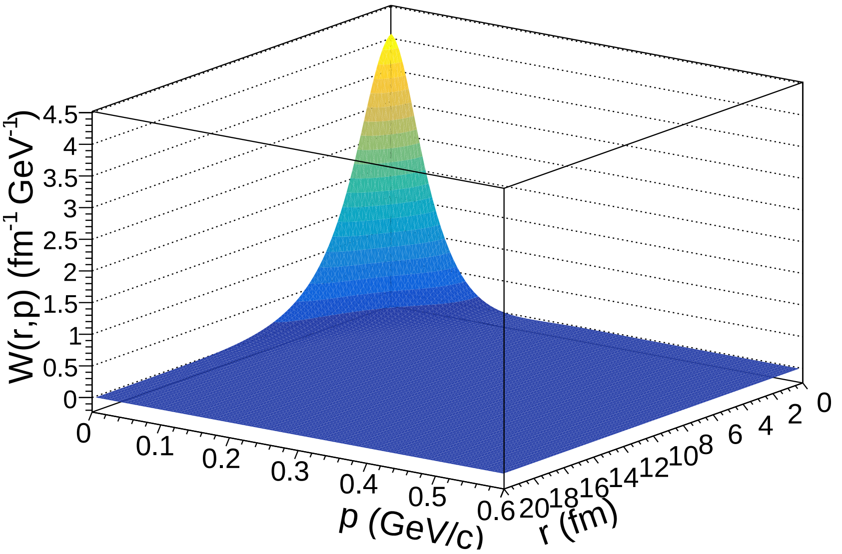

Figure 3.1: Deuteron S-state Wigner function for a deuteron radius of $R_D = 3.2$ fm.

Once the source and deuteron S-state Wigner functions are known, it is possible to compute the coalescence probability as

$$P(k^*) = \int W_{\text{deut}}(\vec{r},\vec{p})\,W_{\text{src}}(\vec{r},\vec{p};k^*)\,d^3r\,d^3p. \tag{3.13}$$

The two formalisms, wave function and Wigner function, yield the same results and are therefore compatible, as shown in Fig. 3.2. The wave function formalism is chosen because it is computationally more efficient, being approximately 33 times faster than the Wigner formalism.

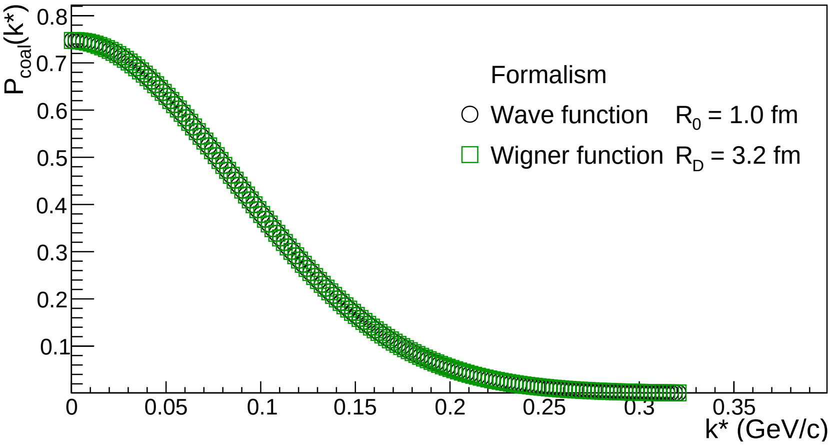

Figure 3.2: Coalescence probability as a function of k^*, obtained with the Wigner formalism (green open circles) and the wave function formalism (black open circles). The distributions are obtained with the same source radius $R_0 = 1$ fm and the same deuteron radius $R_D = 3.2$ fm.

3.1.3 Nucleon spin

The (anti)deuteron, as a (anti)proton–(anti)neutron bound state, exists exclusively in a specific spin configuration. More precisely, it is a triplet state with total spin $S = 1$, where the two nucleon spins are aligned. Conversely, the singlet configuration with total spin $S = 0$, corresponding to anti-aligned spins, does not yield a stable bound state due to the nature of the nuclear force.

In a more complete description, the spin degree of freedom is coupled to the orbital angular momentum through the spin–orbit interaction. The deuteron ground state corresponds primarily to an $L = 0$ (S-wave) configuration with total angular momentum $J = 1$, with a small admixture of $L = 2$ (D-wave) induced by the tensor component of the nuclear force. Thus, the allowed bound state requires not only the triplet spin configuration ($S = 1$), which statistically represents $\frac{3}{4}$ of the possible spin combinations, but also the appropriate coupling between spin and orbital angular momentum that produces the correct total angular momentum $J = 1$.

In the presented model (in both formalisms), spin and orbital angular momentum are not explicitly included. The coalescence probabilities given in Eq. 3.10 and Eq. 3.13 implicitly assume that all proton–neutron pairs can potentially fuse to form a deuteron. In reality, only a subset of proton–neutron pairs can form a bound deuteron. Since the deuteron exists exclusively in the spin–triplet state ($S = 1$), only three out of the four possible spin combinations of two spin-$\frac{1}{2}$ nucleons contribute, yielding a statistical factor of $\frac{3}{4}$. In addition, the deuteron is an isospin singlet state with total isospin $I = 0$. In the coalescence process we start from a proton and a neutron, which have fixed isospin projections $I_3 = +\frac{1}{2}$ and $I_3 = -\frac{1}{2}$, respectively, so that the pair has total third component $I_3 = 0$. Such a proton–neutron system can belong either to the isospin singlet state $(I = 0, I_3 = 0)$ or to the isospin triplet state $(I = 1, I_3 = 0)$. Assuming that these configurations are equally populated in an uncorrelated and unpolarized source, only half of the proton–neutron pairs correspond to the correct isospin configuration required to form a deuteron. This introduces an additional factor of $1/2$ in the coalescence probability. Altogether, these considerations lead to the statistical factor. In order to account for this factor within the model, the coalescence probabilities given in Eq. 3.10 and Eq. 3.13 are multiplied by a statistical factor g effectively implementing a mean-field correction:

$$P_{\text{coal}}^{\text{final}}(k^*) = g\, P_{\text{coal}}(k^*). \tag{3.14}$$

with g being

$$g = \frac{3}{4} \times \frac{1}{2} = \frac{3}{8}. \tag{3.15}$$

3.2 Production of nuclei up to $\mathbf{A} = 4$

In the afterburner nuclei up to A = 4 are formed by iteratively applying coalescence to the previously formed, lighter nuclei, as visible in Fig. 3.3. Starting from protons and neutrons from the event generator, deuterium is created through coalescence; then, by further iterations, tritium or helium-3 are formed, and finally helium-4. The process stops when there is no coalescence or helium-4 is reached. The same procedure is applied for antinuclei starting from antinucleons.

3.2.1 wave function approximation

As seen in Eq. 3.10, the coalescence probability is computed using the deuteron S-state wave function given in Eq. 3.6. Therefore, for the proton–neutron bound state (deuteron), the coalescence probability is evaluated without any approximation.

In the case of nuclei heavier than $A = 2$, an approximation is introduced. The wave

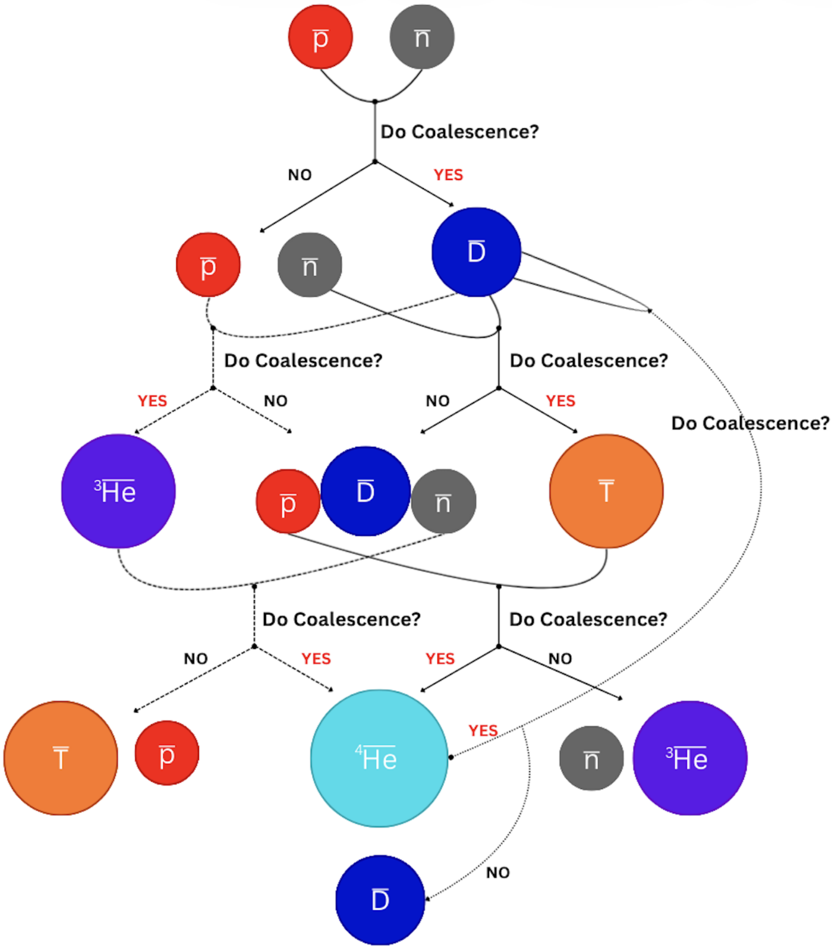

Figure 3.3: (Anti)Nuclei formation conceptual scheme.

function is no longer the exact ground-state wave function of the nucleus, but an approximation based on the deuteron wave function of Eq. 3.6. In this approach, the depth of the square-well potential, V_0, which determines the form of $u(r)$ in Eq. 3.6, is initially taken from the deuteron case. For the formation of heavier nuclei, this depth is scaled assuming that the effective strong charge of a nuclear cluster is proportional to its number of nucleons A. The underlying potential for the interaction between two clusters is then taken to be proportional to the product of their individual strong charges.

For instance, in the coalescence of a deuteron (assumed to have an effective strong charge of 2) and a proton (charge 1) into a triton (T), the depth of the potential well would be scaled as

$$V_{\mathrm{D}+p} = (2 \times 1)\, V_0 = 2V_0. \tag{3.16}$$

After this scaling, the radius of the square well is adjusted as a free parameter to reproduce the known binding energy of the specific nucleus under consideration (e.g., T, $^3\mathrm{He}$, $^4\mathrm{He}$, see Tab. 1.1). An example of this approximation is shown in Fig. 3.4.

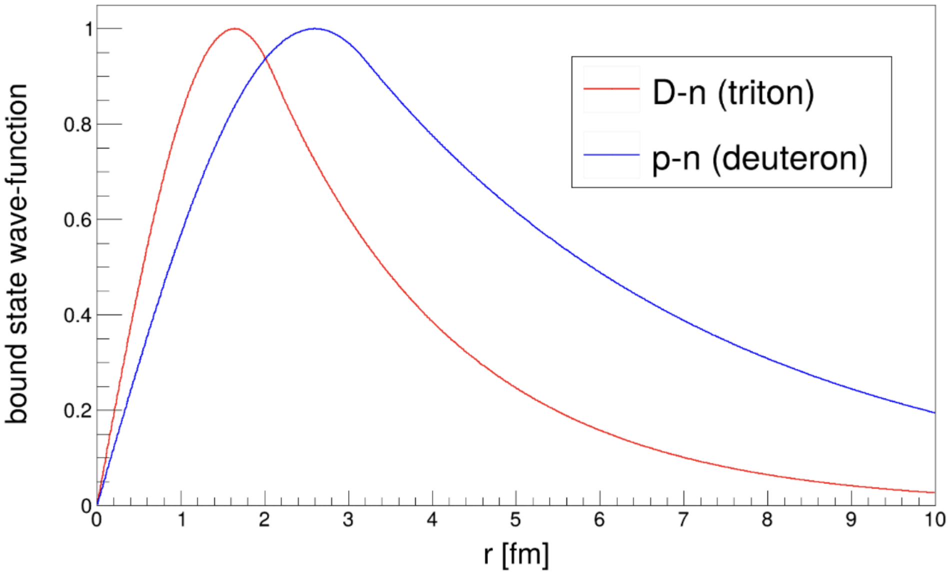

Figure 3.4: Example of the approximate ground-state wave function of tritium (blue) compared to the exact deuteron ground-state wave function (red).

3.2.2 Photon production

In the afterburner model, when a nucleus is produced there is a difference in energy between the initial and the final state,

$$\Delta E = M_{\text{init}} - M_{\text{bound state}}, \tag{3.17}$$

where M_{init} and $M_{\text{bound state}}$ are, respectively, the initial and bound-state invariant masses. The energy difference ΔE is released as a photon in order to obey energy conservation. An example with a p–n pair forming a deuteron is shown in Fig. 3.5, but the same mechanism is also applied in the formation of T, ^3He, ^4He, and the corresponding antiparticles.

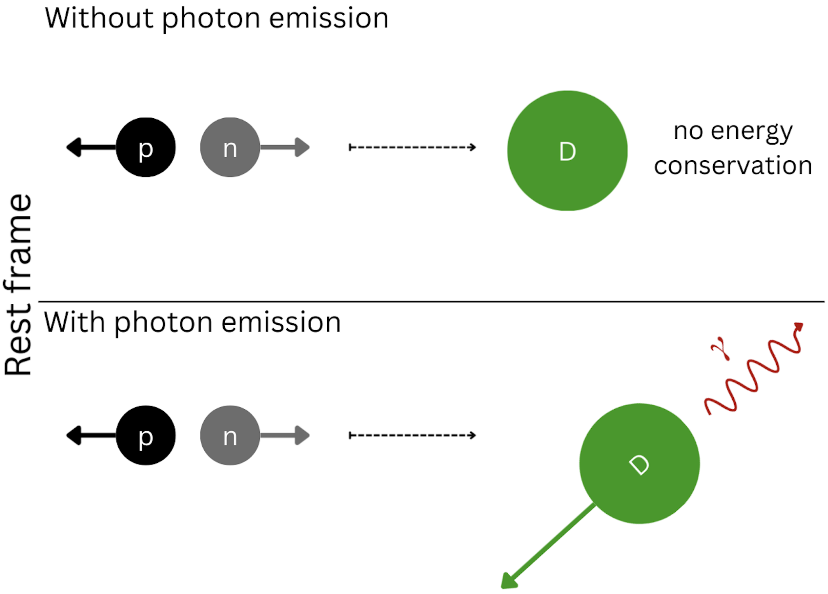

Figure 3.5: Schematic example of the production, in the rest frame, of a photon–deuteron pair.

The photon is produced isotropically in the rest frame of the photon–bound-state system. The fundamental point is the transformation between the rest frame and the laboratory frame, in which both the photon and the deuteron receive a boost. The energy boost of the photon is described by

$$E_{\text{lab}} = \gamma E^* \left(1 + \beta \cos\theta^*\right), \tag{3.18}$$

where E^* is the energy of the photon in the rest frame, $\gamma = \frac{1}{\sqrt{1-\beta^2}}$ is the Lorentz factor, $\beta = \frac{v_{\text{CM}}}{c}$ is the velocity of the rest frame, and θ^* is the polar angle, i.e. the emission angle of the photon in the nucleus rest frame.

The momentum $\vec{p} = (p_x, p_y, p_z)$ is then described, taking the z axis as the direction of motion of the rest frame, as

$$p_{z,\text{lab}} = \gamma\left(p_z^* + \beta\, E^*/c\right) = \gamma \frac{E^*}{c}\left(\cos\theta^* + \beta\right), \tag{3.19}$$

$$p_{x,\text{lab}} = p_x^* = \frac{E^*}{c}\sin\theta^*\cos\phi^*, \tag{3.20}$$

$$p_{y,\text{lab}} = p_y^* = \frac{E^*}{c}\sin\theta^*\sin\phi^*, \tag{3.21}$$

where ϕ^* is the azimuthal emission angle of the photon in the rest frame. As shown by Eqs. 3.19–3.21, only the longitudinal component (p_z) changes, while the transverse components (p_x, p_y) remain unchanged. In the laboratory frame, θ^* transforms as

$$\tan\theta_\text{lab} = \frac{p_{\perp,\text{lab}}}{p_{z,\text{lab}}} = \frac{\sin\theta^*}{\gamma(\cos\theta^* + \beta)}, \qquad \text{with } p_\perp = \sqrt{p_x^2 + p_y^2}. \tag{3.22}$$

The angle ϕ^* remains unchanged. From Eq. 3.22 it can be observed that the larger the boost, the smaller θ_lab becomes; therefore, the photon and the bound-state nucleus are more collimated.

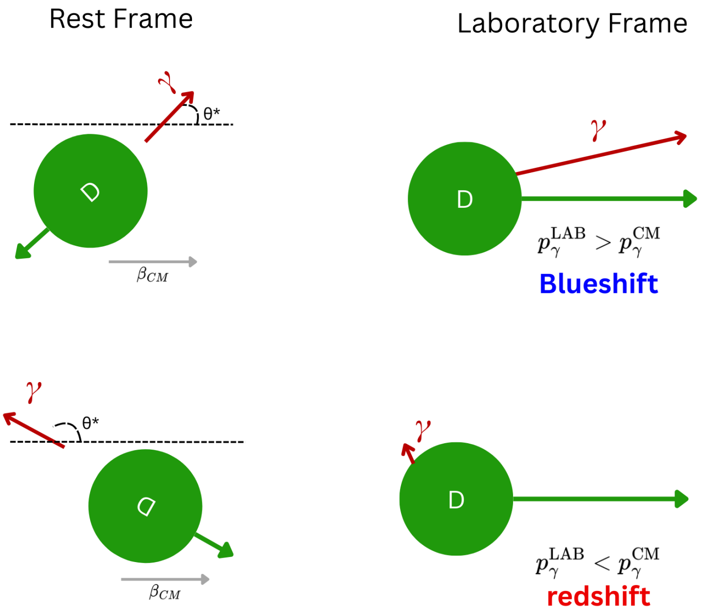

Figure 3.6: Schematic example of the boost in the case of the D–γ system, showing two situations: the effect of the blueshift (upper sketch) and the effect of the redshift (lower sketch).

Figure 3.6 provides a schematic visualization, for the photon–deuteron system, of the application of Eq. 3.19:

- if $\cos\theta^* > 0$, a blueshift occurs; the momentum of the photon in the laboratory frame is larger than in the rest frame, $p_{z,\text{lab}} > p_z^*$, and the emission angle in the laboratory is almost collinear with the direction of motion of the nucleus (i.e. the direction of motion of the rest frame);
- if $\cos\theta^* < 0$, a redshift occurs; the momentum of the photon in the laboratory frame is smaller than in the rest frame, $p_{z,\text{lab}} < p_z^*$, and the emission angle in the laboratory is almost perpendicular to the direction of motion of the nucleus.

The blueshift can be significant.

3.3 N-N Interaction

Up to now, only coalescence has been described; however, not all nucleons and nuclei necessarily undergo coalescence, for several reasons. They may not satisfy the requirements for coalescence (for example, an antiproton–antineutron pair that is too far apart in phase space). Moreover, coalescence is a statistical process, so even if the requirements are satisfied, a bound state may not form. It is also important to note that the particle pair under consideration may not possess a bound state (for example, an antiproton–antiproton pair). For these reasons, it is essential to include nucleon–nucleon (N–N) interactions in the model.

The N–N interaction is modeled within the wave function formalism using a semiclassical approach and is implemented in the afterburner to be applied simultaneously with coalescence. The N–N interaction is based on the comparison between the initial energy of the source and the final energy at infinity (where, in our square-well potential model, the potential is assumed to vanish), from which the nucleon final relative momentum k_f^* is determined:

$$\langle\psi_{\text{source}}|K+V|\psi_{\text{source}}\rangle = \frac{k_f^{*2}}{2\mu} \qquad (v \ll c) \tag{3.23}$$

where K is the kinetic energy, V is the strong plus Coulomb interaction potential, and μ is the reduced mass. Note that, at this stage, as visible in Eq. 3.1, the source radius R_0 is fixed. The classical aspect of the model resides in energy conservation, while the quantum-mechanical aspect resides in the evaluation of the initial energy of the system. The potential V consists of a strong contribution plus a Coulomb term. The strong interaction is modeled by a square-well potential adjusted to the deuteron radius, which is the same potential introduced in Eq. 3.5 for the derivation of the deuteron S-state wave function. The Coulomb interaction is given by

$$V_{\text{Coul}}(r) = \frac{1}{4\pi\epsilon_0}\frac{e^2}{r} = \frac{1.44\ \text{MeV fm}}{r}, \tag{3.24}$$

where ϵ_0 is the vacuum permittivity.

However, this semiclassical approach presents an issue. To identify it, we first need to perform the Fourier transform of Eq. 3.1 in order to move from coordinate space to momentum space:

$$\tilde{\psi}_{\mathrm{src}}(\vec{p}) = \frac{1}{(2\pi\hbar)^{3/2}} \int \psi_{\mathrm{src}}(\vec{r})\, e^{-i\vec{p}\cdot\vec{r}/\hbar}\, d^3r = \left(\frac{8R_0^2}{\pi\hbar^2}\right)^{3/4} \exp\left(-2R_0^2 \frac{(\vec{p}-\vec{k})^2}{\hbar^2}\right). \tag{3.25}$$

Since the source radius R_0 is fixed, the expectation value of the momentum and the expectation value of the squared momentum for the pair are given, respectively, by

$$\langle \vec{p} \rangle = \int \left|\tilde{\psi}_{\mathrm{src}}(\vec{p})\right|^2 \vec{p}\, d^3p = \hbar \langle k^* \rangle, \tag{3.26}$$

$$\langle p^2 \rangle = \int \left|\tilde{\psi}_{\mathrm{src}}(\vec{p})\right|^2 p^2\, d^3p = (\hbar k^*)^2 + \frac{3\hbar^2}{8R_0^2}. \tag{3.27}$$

Equation 3.27 shows a contribution $(\hbar k^*)^2$ arising from the relative momentum k^*, taken as input from the event generator, and an additional term $\frac{3\hbar^2}{8R_0^2}$ related to the fixed source radius R_0, introduced as a model parameter.
From Eq. 3.27, the kinetic energy K can be written as

$$K = \frac{\langle p^2 \rangle}{2\mu} = \frac{(\hbar k^*)^2}{2\mu} + \frac{3\hbar^2}{16R_0^2\mu}. \tag{3.28}$$

Due to the presence of the term $\frac{3\hbar^2}{8R_0^2}$ in Eq. 3.27, the kinetic energy exhibits a minimum value K_{min}. As can be seen from Eq. 3.28, even in the limit $k^* \to 0$, the kinetic energy does not vanish.
The existence of a minimum kinetic energy K_{min} also implies the presence of a minimum relative momentum k^*_{min}, defined through

$$K_{\mathrm{min}} = \frac{{k^*_{\mathrm{min}}}^2}{2\mu}, \tag{3.29}$$

below which no final value of k^* can be obtained.

To overcome this issue and efficiently simulate the N–N interactions in a semiclassical regime, the model must be modified. The adopted strategy is to take the kinetic energy K of the particle pair directly from the event generator as input and to modify the source wave function in Eq. 3.1 such that the kinetic energy entering the semiclassical calculation in Eq. 3.23 reproduces this input value. As a consequence, it is no longer possible to keep the source radius fixed. The source wave function is therefore rewritten as

$$\psi_{\text{src}}(\vec{r}, \vec{k}^*) = A \exp\left(-\frac{r^2}{2R_{\text{eff}}^2}\right) \exp\left(i\frac{\vec{k}^* \cdot \vec{r}}{\hbar}\right), \tag{3.30}$$

where R_{eff} is an effective radius, defined as

$$R_{\text{eff}} = \sqrt{R_{\min}(k^*_{\text{min}})^2 + R_0^2}. \tag{3.31}$$

The minimum radius $R_{\min}$ is given by

$$R_{\min}(k^*_{\text{min}}) = \sqrt{\frac{3}{8}}\,\frac{\hbar}{k^*_{\text{min}}}, \tag{3.32}$$

which is obtained by imposing that the $(\hbar k^*)^2$ term in Eq. 3.27 vanishes.
The definition in Eq. 3.31 represents the simplest choice that allows one to introduce a minimum radius compatible with the initial kinetic energy, while simultaneously incorporating the effect of a Gaussian source with characteristic radius R_0. With this prescription, it is ensured that the kinetic energy does not exceed the initial value and that the classical limit is recovered for large values of k^*. Consequently, from Eq. 3.31, it follows that:

- for small values of k^*, the contribution from $R_{\min}$ dominates;
- for large values of k^*, the contribution from R_0 dominates.

In Fig. 3.7 the $C(k^*)$ distribution before the application (left) is compared to that after the application (right) of the model to $\overline{\mathrm{p}} - -\overline{\mathrm{p}}$ pairs from simulated events. A peak is visible after the application, originating from the strong interaction.
The model has also been proven successful in reproducing the effect of the source size, as shown in Fig. 3.7 (left). When applied through the afterburner, the model correctly captures the dependence of the correlation function on the source size, with the peak of $C(k^*)$ decreasing as the source radius R_0 (which enters in Eq. 3.31) increases, as expected from Fig. 1.15 (right). The value of the peak of $C(k^*)$ (Fig. 1.15 (right)), considering the value of the source size from Fig. 1.16 ($R_0 = 1.125$ fm [79]), is higher by a factor of 3. This is due to the semiclassical approximation.

The initial model, which hereafter will be referred to as the *fixed R_0 model*, does not efficiently reproduce the N–N interaction due to the semiclassical approximation. This motivated its modification into a second model, referred to as the *$R_{\text{eff}}(k^*)$ model*. However, since the radius is modified in Eq. 3.1, the coalescence probability will also differ, as visible in Fig. 3.8. Figure 3.8 also shows that, when the kinetic energy is fixed, a depletion appears in the low-k^* region as a consequence of the large effective radius R_{eff}.

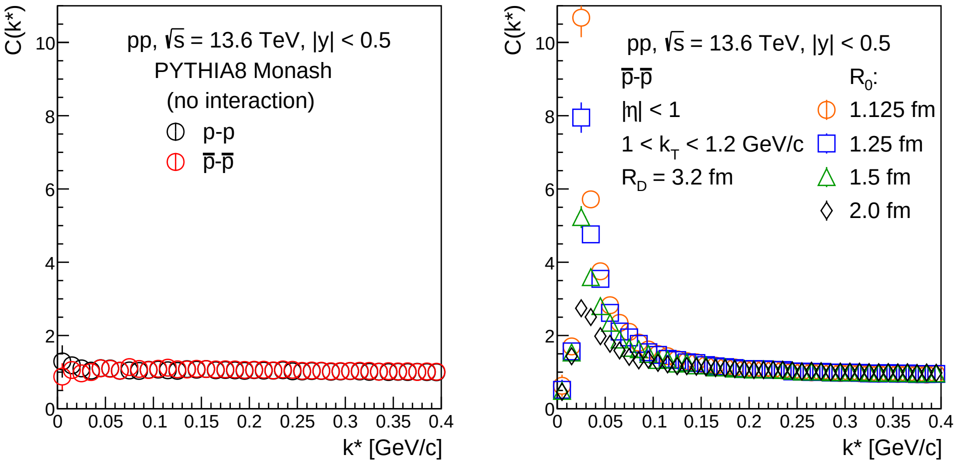

Figure 3.7: Right: Correlation function of p–p (black) and $\bar{\mathrm{p}}$–$\bar{\mathrm{p}}$ (red) pairs for one billion events at $\sqrt{s} = 13.6$ TeV (LHC configuration), before the application of the afterburner. A cut on the rapidity is applied: $|y| < 0.5$. Left: Correlation function for antiproton–antiproton pairs as a function of k^* for different source radii R_0 and fixed deuteron radius $R_D = 3.2$ fm. The following selections are applied: pair average transverse momentum 1 GeV$< k_T < 1.2$ GeV, pseudorapidity $|\eta| < 1$ and rapidity $|y| < 0.5$.

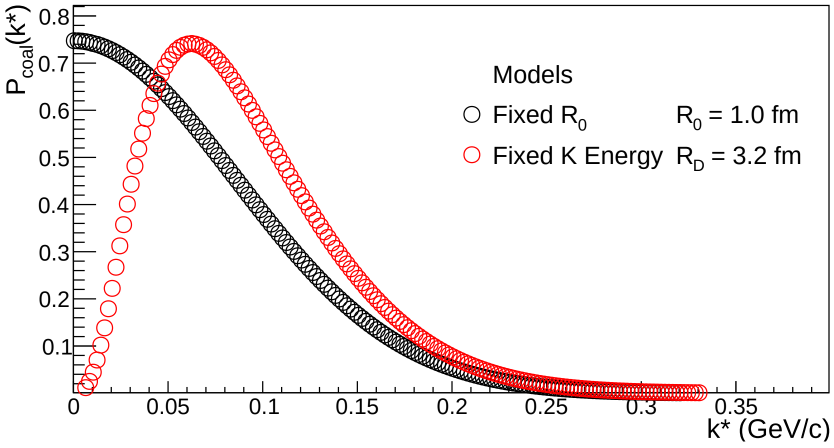

Figure 3.8: Coalescence probability as a function of k^* for: the fixed R_0 model (black) and the $R_{\text{eff}}(k^*)$ model (red), both with source radius $R_0 = 1$ fm and a deuteron radius $R_D = 1$ fm.

The model with fixed R_0 remains valid for coalescence and will also apply to N–N interactions once a fully quantum-mechanical treatment is introduced. For this reason, results (excluding those related to N–N interactions) obtained with both models will be shown in Chap. 4.

N-N interaction in Wigner formalism

In the wave function formalism, the source wave function (Eq. 3.30) has been redefined to take into account the effective radius R_{eff} (Eq. 3.31). Consequently, the Wigner function of the source, which is derived from the source wave function (see Eq. 3.11), becomes:

$$W_{\text{src}}(\vec{r},\vec{p}) = \frac{1}{(2\pi\hbar)^3} \exp\left(-\frac{r^2}{4R_{\text{eff}}^2}\right) \exp\left[-\frac{4R_{\text{eff}}^2}{\hbar^2}\left(\vec{k}^* + \vec{p}\right)^2\right]. \tag{3.33}$$

When compared to the wave function formalism within the same model, identical results are obtained, as shown in Fig. 3.9.

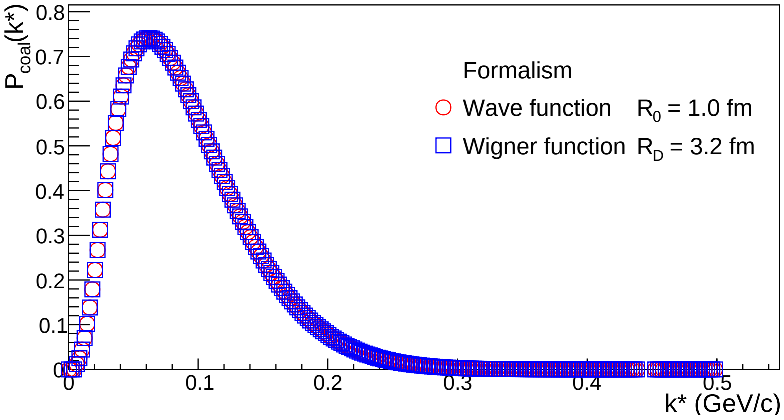

Figure 3.9: Coalescence probability as a function of k^*, obtained with the Wigner formalism (red open circles) and the wave function formalism (blue open circles) for the model with fixed kinetic energy. The distributions are obtained with the same source radius $R_0 = 1$ fm and the same deuteron radius $R_D = 3.2$ fm.

Looking at the interaction from the Wigner-formalism point of view, the fundamental idea is again to compare the initial energy of the source with the final energy at infinity, as done in Eq. 3.23, but with a different left-hand side, since wave functions are not used in this case. The corresponding expression is

$$\langle K\rangle + \langle V\rangle, \tag{3.34}$$

where

$$\langle K \rangle = \int_{\mathbb{R}^3} \int_{\mathbb{R}^3} W_s(\vec{r}, \vec{p})\, K(\vec{p})\, d^3\vec{r}\, d^3\vec{p}, \tag{3.35}$$

and

$$\langle V \rangle = \int_{\mathbb{R}^3} \int_{\mathbb{R}^3} W_s(\vec{r}, \vec{p})\, V(\vec{r})\, d^3\vec{r}\, d^3\vec{p}. \tag{3.36}$$

Here, $V(\vec{r})$ is the same potential used in the wave function model, composed by the strong interaction given in Eq. 3.5 and the Coulomb interaction given in Eq. 3.24.

The Wigner and wave formalisms yield the same results also for the N-N interaction, as shown in Fig. 3.10. The comparison demonstrates that the interaction effects, encoded in the Same Event distribution, are consistent between the two approaches. Additionally, within this model and formalism, the spin–orbit dependence is implemented as described in Sec. 3.1.3.

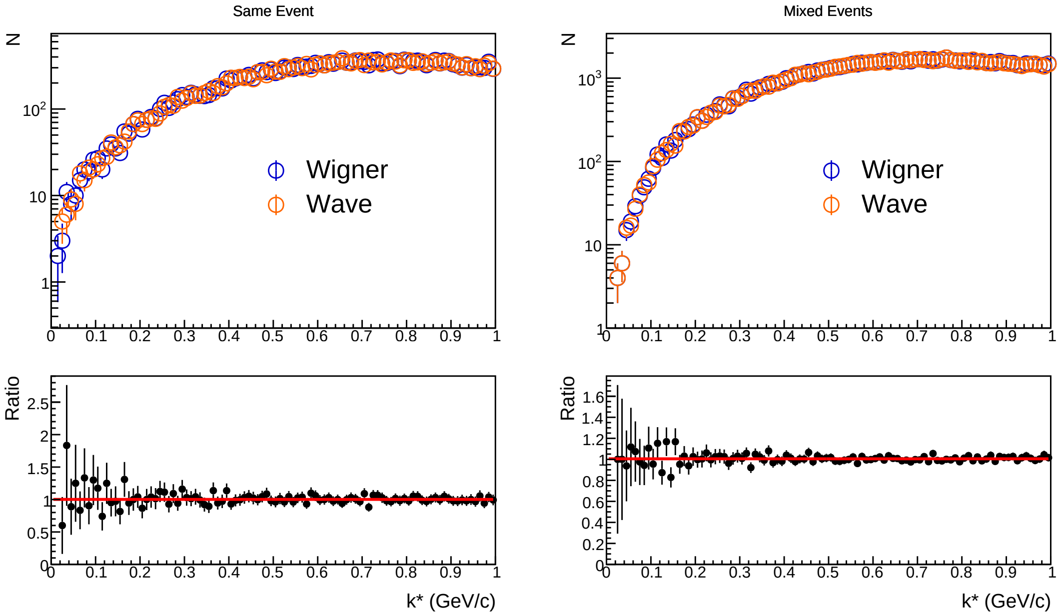

Figure 3.10: Comparison between the Same Event (SE) k^* distribution for p–p pairs (left) and the Mixed Event (ME) k^* distribution for p–p pairs (right), obtained with the Wigner-function formalism (orange) and the wave function formalism (blue). The bottom panel shows the ratio of the results obtained with the two formalisms.

3.4 Event simulation with PYTHIA

The afterburner, as already hinted in Secs. 3.1.1 and 3.2, is a framework that simulates coalescence and interaction on already generated nucleon events. These events must be provided by an event generator; in this work, PYTHIA8 [131] is used.

For the purposes of this study, PYTHIA8 was used to simulate particle collisions under different beam configurations and center-of-mass energies. The configurations considered include proton–proton (pp) collisions at a center-of-mass energy of $\sqrt{s} = 13.6$ TeV, corresponding to the energy achieved during LHC Run 3 (2022–2026); electron–proton (ep) collisions at the HERA center-of-mass energy of $\sqrt{s} = 318$ GeV; and electron–proton (ep) collisions at the projected Electron–Ion Collider (EIC) beam energies, with a proton beam energy of $E_p = 130$ GeV and an electron beam energy of $E_e = 10$ GeV.

proton–proton collisions at $\sqrt{s} = 13.6$ TeV (LHC)

The simulated events correspond to protons, antiprotons, neutrons, and antineutrons from collisions at a center-of-mass energy of $\sqrt{s} = 13.6$ TeV, which is the energy reached at the LHC during Run 3, were simulated.

In the PYTHIA8 configuration both incoming beams are set to protons by assigning the Particle Data Group (PDG) code 2212 to beam A and beam B (`Beams:idA = 2212` and `Beams:idB = 2212`). The center-of-mass energy of the collision is fixed to `Beams:eCM = 13600`, expressed in GeV.
Only inelastic soft QCD processes are enabled in the simulation by setting `SoftQCD: inelastic = on`. This choice allows the generation of minimum-bias events dominated by non-perturbative QCD interactions, which are responsible for the bulk production of low-momentum hadrons and (anti)nucleons relevant for coalescence studies.

Particle decays are handled with particular care, since the afterburner relies on the spatial and kinematic correlations of nucleons. Long-lived particles are allowed to propagate up to a maximum proper lifetime of `ParticleDecays:tau0Max = 10` mm/c, while decays are enabled only for selected resonances. In particular, decays of ρ and Δ resonances are allowed, whereas weakly decaying strange baryons, kaons, pions, neutrons, and antineutrons are forced to be stable. This choice ensures that nucleons originating from displaced weak decays are not mixed with promptly produced nucleons, preserving a well-defined production vertex for the coalescence procedure.

No explicit phase-space cuts are imposed on the hard scattering. The transverse momentum of the partonic interaction is left unrestricted by setting `PhaseSpace:pTHatMin =`

`0` and `PhaseSpace:pTHatMax = -1`, allowing the full kinematic range of soft interactions to be sampled.

Of the particles produced, only nucleons and antinucleons are selected to apply the afterburner. In Fig. 3.7 (left), the correlation function $C(k^*)$ of p–p and $\bar{p}$–$\bar{p}$ pairs before the application of the afterburner is shown. In this case, $C(k^*)$ is flat because no interaction is applied to the nucleons, neither in PYTHIA8 nor in the afterburner. Figure 3.11 shows the momentum spectra of these (anti)particles.

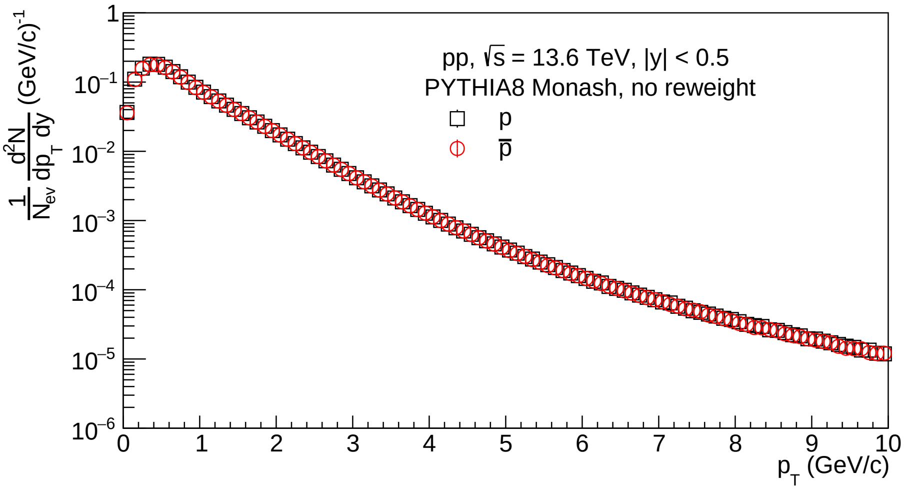

Figure 3.11: Proton (black) and antiproton (red) p_T distributions from 1 billion of proton–proton collision events at $\sqrt{s} = 13.6$ TeV (LHC configuration) produced by PYTHIA8. A selection on rapidity is applied $|y| < 0.5$. The two spectra overlap, showing a symmetry between particles and antiparticles.

electron–proton collisions in the HERA regime

The simulated events correspond to 2 billion of electron–proton collisions events at HERA energies, with an electron beam energy of $E_e = 27.5$ GeV and a proton beam energy of $E_p = 920$ GeV.

The incoming beams are set to an electron and a proton by assigning the Particle Data Group (PDG) codes 11 and 2212 to beam A and beam B, respectively (`Beams:idA = 11` and `Beams:idB = 2212`). The beam energies are fixed to `Beams:eA = 27.5` for electrons and `Beams:eB = 920` for protons, expressed in GeV. The laboratory-frame configuration is enforced by setting `Beams:frameType = 2`.

The hard process is simulated through electroweak boson exchange enabling `WeakBoson Exchange: ff2ff(t:gmZ) = on`. In addition, initial-state radiation is treated with the dipole recoil scheme by setting `SpaceShower:dipoleRecoil = on`. A minimum value of the photon virtuality is imposed by requiring `PhaseSpace:Q2min = 1`.

Particle decays are handled consistently with the proton–proton setup. As previously done for pp collisions also here of the particles produced, only nucleons and antinucleons are selected to apply the afterburner. The starting proton and antiproton spectra are shown in Fig. 3.12.

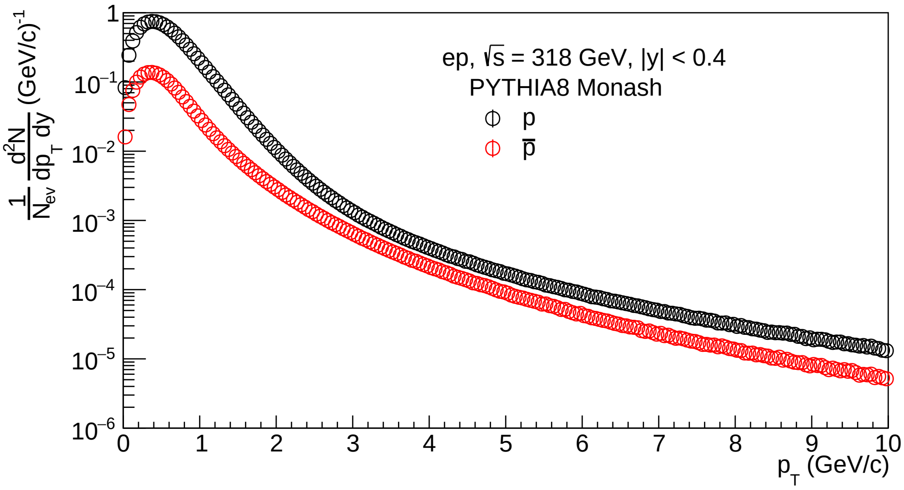

Figure 3.12: Proton (black) and antiproton (red) spectra from 2 billion electron–proton collision events in the HERA configuration, produced by PYTHIA8. A rapidity cut $|y| < 0.5$ is applied.

electron–proton collisions in the EIC regime

The simulated events correspond to 1 billion of electron–proton collisions events at Electron–Ion Collider (EIC) energies, with a proton beam energy of $E_p = 130$ GeV and an electron beam energy of $E_e = 10$ GeV.

The incoming beams are set to a proton and an electron by assigning the Particle Data Group (PDG) codes 2212 and 11 to beam A and beam B, respectively (`Beams:idA = 2212` and `Beams:idB = 11`). The beam energies are fixed to `Beams:eA = 130` for protons and `Beams:eB = 10` for electrons, expressed in GeV. The laboratory-frame configuration is enforced by setting `Beams:frameType = 2`.

The hard scattering process is simulated through electroweak boson exchange by enabling `WeakBosonExchange:ff2ff(t:gmZ) = on`. Initial-state radiation is treated using the dipole recoil scheme by setting `SpaceShower:dipoleRecoil = on`. A lower bound on the photon virtuality (the four-momentum transferred by the photon) is imposed through the parameter `PhaseSpace:Q2min`, varied for the analysis between $Q^2 > 1, 5, 10, 20$ GeV^2.

Particle decays are handled consistently with the LHC pp and HERA ep setups. Also here of the particles produced, only nucleons and antinucleons are selected to apply the afterburner. The starting proton and antiproton spectra are shown in Fig. 3.13.

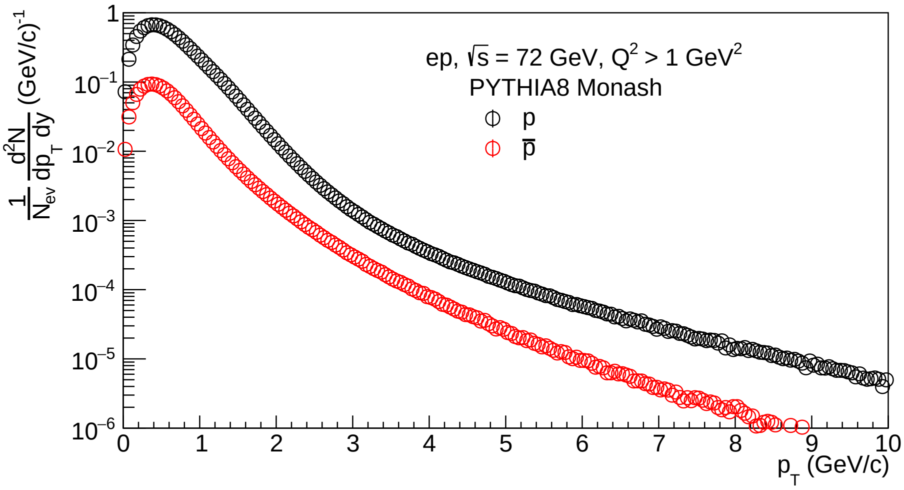

Figure 3.13: Proton (black) and antiproton (red) spectra from 1 billion of electron–proton collision events in the EIC configuration, produced by PYTHIA8. No cut on rapidity or pseudorapidity has been applied, while the photon virtuality is set to $Q^2 > 1$ GeV^2.

Chapter 4

Application of the Coalescence Afterburner to pp and ep Collisions

After establishing the coalescence and nucleon–nucleon (N–N) interaction framework in the previous chapter, this chapter presents its applications in proton–proton and electron–proton collisions. The afterburner is coupled to PYTHIA event samples generated with configurations relevant for the LHC, HERA, and the future EIC.

The first part of the chapter focuses on proton–proton collisions at $\sqrt{s} = 13.6$ TeV. Transverse-momentum spectra of $\overline{p}$, $\overline{D}$, $\overline{T}$, ${}^{3}\overline{\mathrm{He}}$ at midrapidity are compared to ALICE measurements. From these spectra, the coalescence parameters B_2 and B_3 are extracted and used to constrain the source parameters through a grid-based χ^2 minimisation procedure, providing best-fit values, uncertainties, and correlations. The associated photon production from (anti)deuteron formation is then investigated, showing how γ-$\bar{d}$ kinematics can be exploited to reconstruct the relative-momentum distribution of $\bar{p}$–$\bar{n}$ pairs prior to coalescence. Finally, the interplay between coalescence and N–N interactions is studied through two-particle correlation functions $C(k^*)$, by comparing scenarios with coalescence switched on and off in order to quantify the depletion of low relative momentum (k^*) nucleon pairs due to bound-state formation. This effect is particularly relevant in the context of three-body correlations, such as those probed in deuteron–proton femtoscopy, where the formation of ${}^{3}\overline{\mathrm{He}}$ can further reduce the available pair yield, thereby modifying the correlation signal and offering a direct handle on the interplay between clustering and final-state interactions.

The second part addresses electron–proton collisions. The framework is first confronted with HERA data at $\sqrt{s} = 318$ GeV by comparing the simulated B_2 distributions for D and $\overline{D}$ to ZEUS measurements. Building on this validation, predictions are provided for the EIC configuration, including pseudorapidity-dependent yields of deuterons and antideuterons and the corresponding B_2 distributions within the acceptance of the future ePIC dual RICH (dRICH) detector [99] for different photon-virtuality selections.

4.1 Proton–Proton collisions

In this section, we present the results, validations, and predictions obtained by applying the afterburner to the 10^9 pp collision events at $\sqrt{s} = 13.6$ TeV generated with PYTHIA8 using the LHC configuration described in Sec. 3.4.

4.1.1 Antiparticle spectra

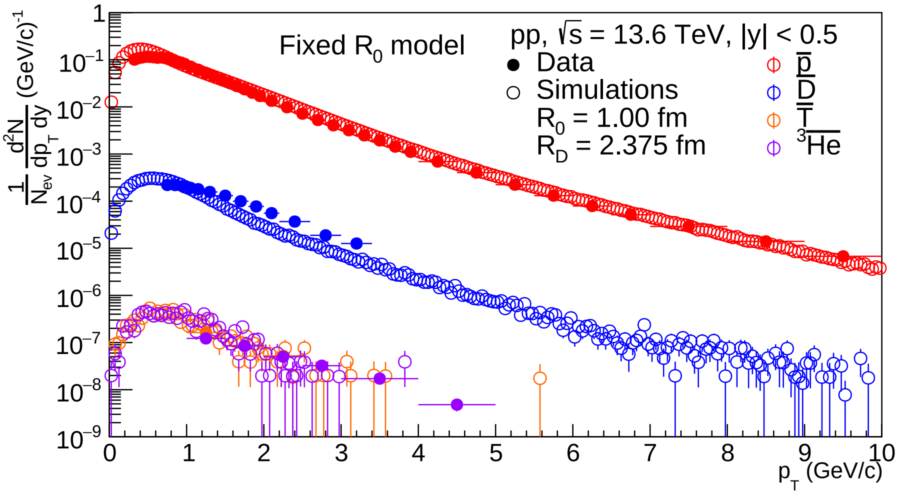

Figure 4.1: Transverse momentum p_T distributions for $\overline{p}$, $\overline{D}$, $\overline{T}$, $^3\overline{\mathrm{He}}$ at midrapidity ($|y| < 0.5$). Simulated distributions (open markers) are obtained from 10^9 pp collisions at $\sqrt{s} = 13.6$ TeV generated with PYTHIA, followed by the afterburner with parameters $R_0 = 1.00$ fm and $R_D = 2.375$ fm. Data (full markers) are from ALICE [132, 22].

The simulated transverse momentum (p_T) distributions of antiproton ($\overline{p}$), antideuteron ($\overline{D}$), antitriton ($\overline{T}$), and antihelium-3 ($^3\overline{\mathrm{He}}$), obtained with the method described in Sec. 3.2 (fixed R_0 model), are shown in Fig. 4.1. The results are in good agreement with the ALICE data [132, 22]. The corresponding spectra obtained with the $R_{\text{eff}}(k^*)$ model are shown in Fig. 4.2; in this case, the p_T distribution of antihelium-4 ($^4\overline{\mathrm{He}}$) is also included. All antinuclei are reported for rapidity $|y| < 0.5$ to allow for a direct comparison with the ALICE measurements [132, 22].

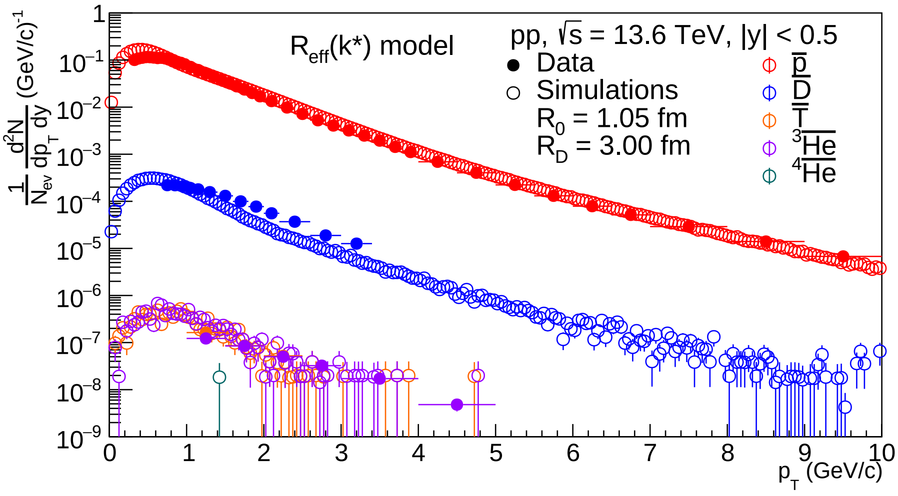

Figure 4.2: Transverse momentum p_T distributions for $\overline{p}$, $\overline{D}$, $\overline{T}$, $^3\overline{\mathrm{He}}$, and $^4\overline{\mathrm{He}}$ at midrapidity ($|y| < 0.5$). Simulated distributions (open markers) are obtained from 10^9 pp collisions at $\sqrt{s} = 13.6$ TeV generated with PYTHIA, followed by the afterburner using the $R_{\text{eff}}(k^*)$ model, with parameters $R_0 = 1.05$ fm and $R_D = 3.00$ fm. Data (full markers) are from ALICE [132, 22].

Reweighting of the spectra

The same afterburner applies to both nuclei and antinuclei. Here (Fig. 4.1, 4.2), only antimatter is reported. Since the antiproton and antineutron spectra are not generated through the coalescence mechanism, varying the values of R_D and R_0 does not modify their spectral shapes. However, it changes the overall number of nucleons and antinucleons, as a fraction of them undergoes coalescence to form heavier nuclei. The simulations are reweighted event-by-event to rescale p, n, $\overline{p}$, $\overline{n}$ spectra to the p and $\overline{p}$ measured distributions. It should be noted that no data are available for n, $\overline{n}$, so isospin symmetry arguments are applied in this procedure. Similarly antimatter is produced in equal amounts as matter as the LHC [22, 132] In Appendix A.1, the antiproton spectra without reweighting compared to the data and the reweighted ones are shown.

The spectra in Fig. 4.1 and Fig. 4.2 exhibit the characteristic decreasing trend as a function of transverse momentum p_{T}, with a strong suppression of the production yield as the baryon number increases. The abundance decreases by seven orders of magnitude when moving from antiprotons to $^3\overline{\mathrm{He}}$, reflecting the progressively rarer formation of heavier antinuclei. The production remains dominated by the low-p_{T} region, as typically expected in high-energy pp collisions. For $^4\overline{\mathrm{He}}$, only one candidate in 10^9 events has been found with the $R_{\text{eff}}(k^*)$ model (Fig. 4.2), and none with the fixed R_0 model (Fig. 4.1).

The coalescence parameter B_2 obtained with fixed R_0 configuration is shown in Fig. 4.3 (open marker) and is consistent with the data (full marker). In Fig. 4.4, the B_2 parameter obtained with the $R_{\text{eff}}(k^*)$ model is presented. Within the explored kinematic range, B_2 shows a mild increasing trend with p_{T}/A. This behaviour is quantitatively reproduced by the simulation within uncertainties, as confirmed by the ratio to data. The lower panels of the figures show the ratio between simulation and data, highlighting that the model reproduces the measured B_2 within unity across the full p_{T}/A interval. The overall agreement confirms that the implemented coalescence frameworks capture the essential features governing antideuteron production in high-energy pp collisions.

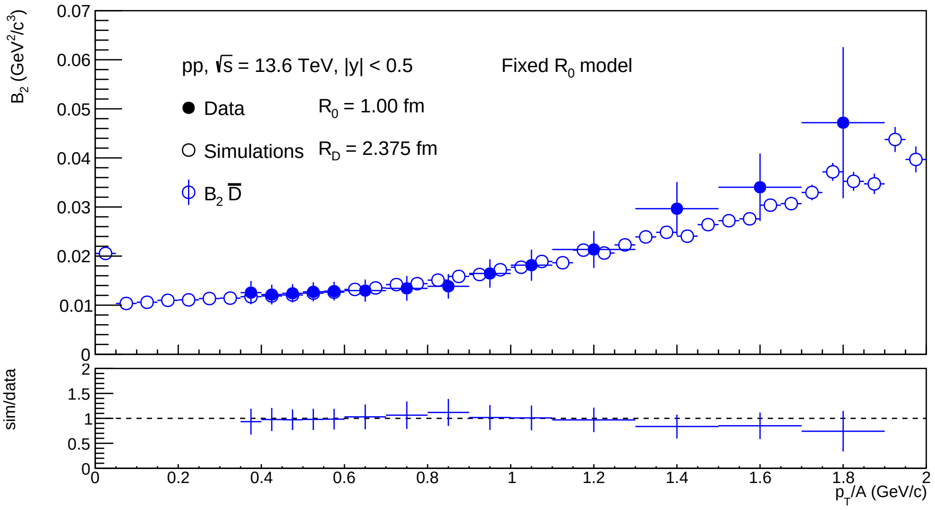

Figure 4.3: B_2 distribution (top panel) for p_T/A at midrapidity ($|y| < 0.5$). In the fixed R_0 coalescence configuration with $R_0 = 1.00$ fm and $R_D = 2.375$ fm. The data (full markers) are from [133]. The ratio between simulation and data (bottom panel) is also shown.

The spectra shown in Fig. 4.1 and Fig. 4.2 are obtained by reweighting the simulated antinucleon distributions to the data [132, 22], while the parameters R_D and R_0 are determined, both for the spectra and for the B_2 distribution, through a fine-tuning procedure (described in detail in the following subsection).

The B_3 parameter (obtained with A=3 in Eq. 1.16) reported in Fig. 4.5. In Fig. 4.6, the B_3 parameter obtained with the $R_{\text{eff}}(k^*)$ model is presented. In this case the values of R_0 and R_D are not fined tuned using B_3 data, but they come from the fine tuning from the B_2 distributions. Moreover, the $\overline{T}$ and $^3\overline{\text{He}}$ wave functions are not the exact

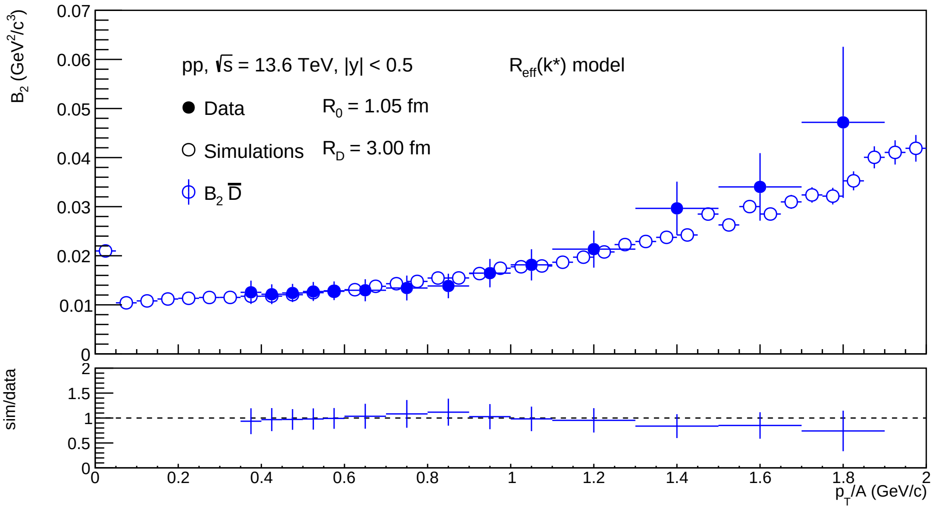

Figure 4.4: B_2 distribution (top panel) for p_T/A at midrapidity ($|y| < 0.5$). The simulation (open markers) is obtained from the $R_{\text{eff}}(k^*)$ model, with parameters $R_0 = 1.05$ fm and $R_D = 3.00$ fm. The data (full markers) are from [133]. The ratio between simulation and data (bottom panel) is also shown.

ground-state solutions, but are constructed using the approximate square-well approach described in Section 3.2.1. In this framework, the depth of the interaction potential is scaled according to the effective strong charges of the clusters involved, while the well radius is adjusted to reproduce the experimental binding energy of the nucleus. However, the results obtained are consistent with data. In Fig. 4.5 the ratio between simulation and data (bottom panel) is compatible with unity until 0.8 GeV/c, from that point is still close and qualitative compatible. In Fig. 4.6 the ratio between simulation and data (bottom panel) is compatible with the unity for all the range.

Fine tuning of radius parameters

The fine tuning of the R_D and R_0 parameters is performed through the comparison of the B_2 distribution obtained from the simulation with ALICE data [133]. The comparison is carried out bin-by-bin using the definition $\chi^2 = \sum_{i=1}^{n} \frac{(O_i - E_i)^2}{\sigma_i^2}$, where O_i is the simulated B_2 value, E_i is the experimental B_2 value [133], and σ_i represents the total (statistical and systematic, combined in quadrature) uncertainty associated with the data [133]. Each set of R_0 and R_D corresponds to a specific B_2 distribution and therefore to a given value of χ^2. The optimal set of parameters is chosen as the one that minimises the χ^2 value. The explored parameter ranges are:

- R_0 varies from 0.8 fm to 1.5 fm in steps of 0.05 fm;

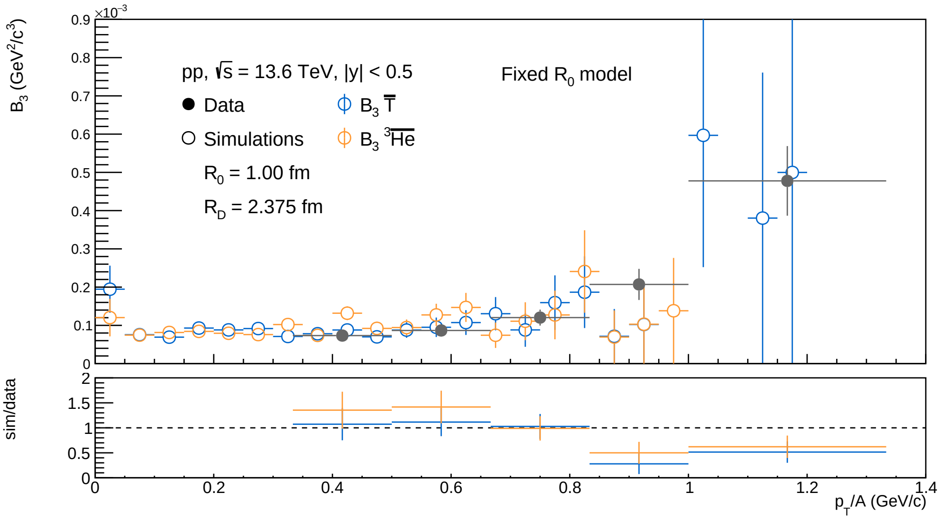

Figure 4.5: B_3 distribution (top panel) for p_T/A in the fixed R_0 coalescence configuration with $R_0 = 1.00$ fm and $R_D = 2.375$ fm. The data (full markers) are from [22]. The ratio between simulation and data (bottom panel) is also shown.

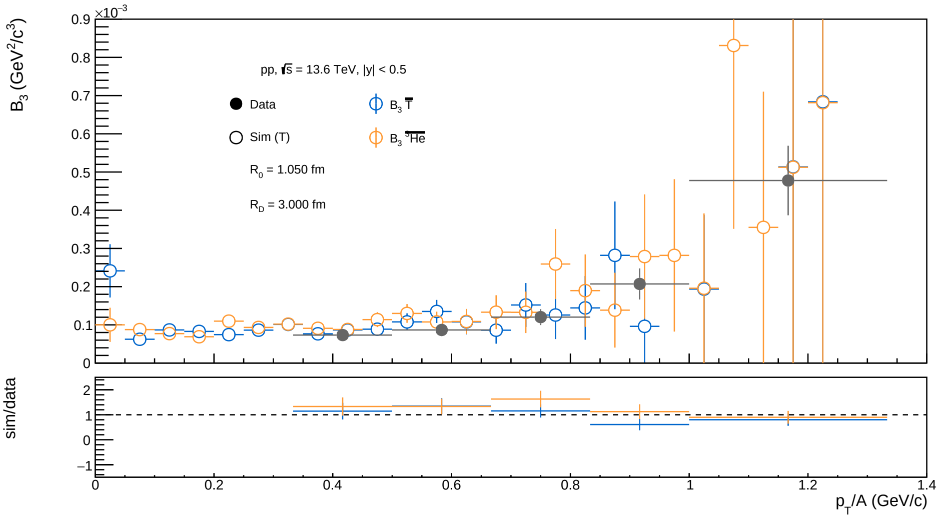

Figure 4.6: B_3 distribution (top panel) for p_T/A obtained from the $R_{\text{eff}}(k^*)$ model, with parameters $R_0 = 1.05$ fm and $R_D = 3.00$ fm. The data (full markers) are from [22]. The ratio between simulation and data (bottom panel) is also shown.

- R_D varies from 1.5 fm to 3.625 fm in steps of 0.125 fm.

These variations are chosen also considering the computational aspects: the time required for a single model is approximately $1,$day $\cdot$ core$/$point. In this case, 270 grid points are evaluated using 20 cores, resulting in a total computation time of approximately 14 days. The χ^2 grids are shown in Fig. 4.7 and Fig. 4.8. Both grids exhibit a clear anticorrelation between R_0 and R_D, together with a qualitative consistency between the two models.

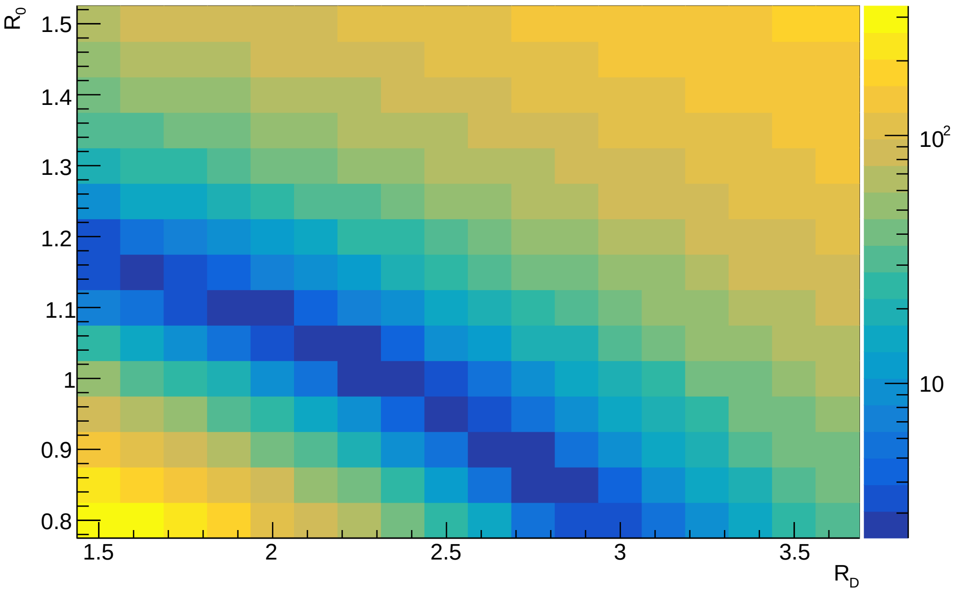

Figure 4.7: Distribution of χ^2 as a function of R_0 and R_D for the model with fixed R_0.

From Fig. 4.7, the best-fit values that reproduce the data for this model are $R_0 = 1.00 \pm 0.06$ fm and $R_D = 2.375 \pm 0.234$ fm, while for the model shown in Fig. 4.8 the optimal parameters are $R_0 = 1.05 \pm 0.03$ fm and $R_D = 3.00 \pm 0.20$ fm.

Since the values of χ^2 as a function of the radius parameters form a discrete distribution, the chosen method to estimate the uncertainties on the parameters is based on the minimisation of χ^2,

$$\chi^2(\theta) \approx \chi^2_{\text{min}} + \frac{1}{2}(\theta - \hat{\theta})^T H(\theta - \hat{\theta}), \tag{4.1}$$

where χ^2_{min} is the minimum value of χ^2 on the grid (Fig. 4.7 and Fig. 4.8), $\theta = \begin{pmatrix} R_D \\ R_0 \end{pmatrix}$, $\hat{\theta} = \begin{pmatrix} \hat{R}_D \\ \hat{R}_0 \end{pmatrix}$, with $\hat{R}_D$ and $\hat{R}_0$ being the values of R_D and R_0 at χ^2_{min}. The Hessian matrix

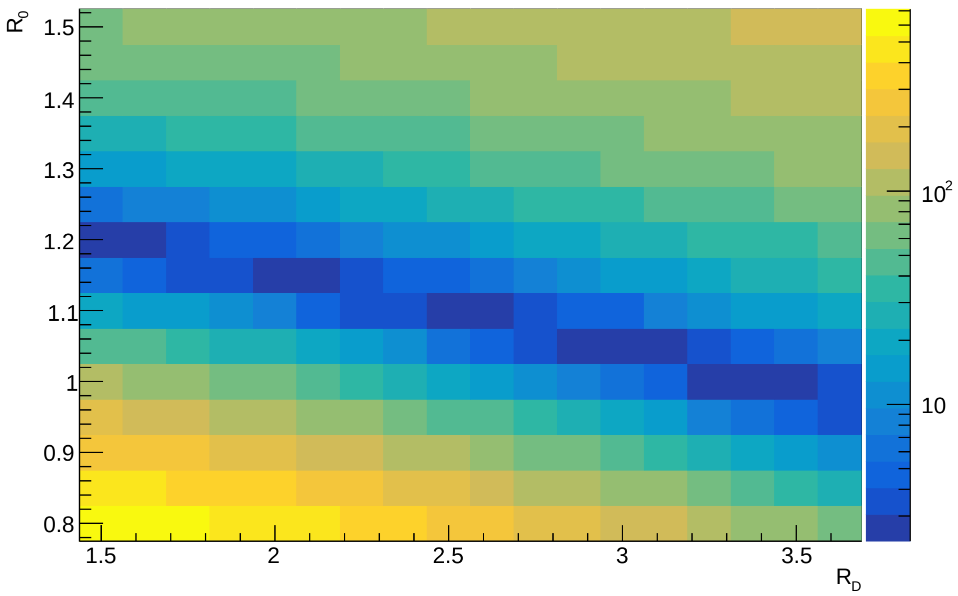

Figure 4.8: Distribution of χ^2 as a function of R_0 and R_D for the $R_{\text{eff}}(k^*)$ model.

H is defined as

$$H = \begin{pmatrix} H_{11} & H_{12} \\ H_{12} & H_{22} \end{pmatrix} = \begin{pmatrix} \dfrac{\partial^2\chi^2}{\partial R_D^2} & \dfrac{\partial^2\chi^2}{\partial R_D \partial R_0} \\ \dfrac{\partial^2\chi^2}{\partial R_0 \partial R_D} & \dfrac{\partial^2\chi^2}{\partial R_0^2} \end{pmatrix}_{\hat{\theta}} . \tag{4.2}$$

From the Hessian matrix, it is possible to derive the covariance matrix Σ,

$$\Sigma = H^{-1} = \frac{1}{\det H} \begin{pmatrix} H_{22} & -H_{12} \\ -H_{12} & H_{11} \end{pmatrix} . \tag{4.3}$$

From the covariance matrix, the uncertainties on R_D and R_0 are obtained as

$$\sigma_{R_D} = \sqrt{\Sigma_{11}} = \sqrt{\frac{H_{22}}{\det H}}, \qquad \sigma_{R_0} = \sqrt{\Sigma_{22}} = \sqrt{\frac{H_{11}}{\det H}}. \tag{4.4}$$

The correlation coefficient is

$$\rho = \frac{\Sigma_{12}}{\sigma_{R_D}\sigma_{R_0}} = \frac{-H_{12}}{\sqrt{H_{11}H_{22}}}. \tag{4.5}$$

The full method is described in Appendix A.2. The results obtained with this method are reported in Tab. 4.1 under *Hessian*, and are compared, as a cross-check, with a fit procedure (Appendix A.3). From the table, it can be seen that the two methods give compatible results. Therefore, the values adopted in the simulations as best-fit parameters are:

- $R_D = 2.375$ fm and $R_0 = 1.00$ fm for the fixed R_0 model,
- $R_D = 3.00$ fm and $R_0 = 1.05$ fm for the $R_{\text{eff}}(k^*)$ model.

The values of the correlation coefficients are also reported in Tab. 4.1 under *Hessian*. For both models, the coefficients are negative, indicating an anticorrelation between R_0 and R_D.

Model	Parameter	Hessian		Fit
		Value $\pm\,\sigma$	ρ	Value $^{+\sigma_R}_{-\sigma_L}$
R_0 fixed model	R_0	1.00 ± 0.06 fm	-0.92	$0.98^{+0.07}_{-0.05}$ fm
	R_D	2.375 ± 0.234 fm		$2.33^{+0.25}_{-0.20}$ fm
$R_{\text{eff}}(k^*)$ model	R_0	1.05 ± 0.03 fm	-0.76	$1.03^{+0.06}_{-0.03}$ fm
	R_D	3.00 ± 0.20 fm		$2.96^{+0.32}_{-0.39}$ fm

Table 4.1: Comparison of parameter estimates from the Hessian and Fit methods. For the Hessian method, ρ is provided.

4.1.2 Photon production

From the knowledge of the k^* distribution of photon-antideuteron ($\gamma - \bar{D}$) pairs, as visible in Fig. 4.9 is possible to derive the k^* distribution for antiproton–antineutron pairs, just using kinematics

$$k^*_{\bar{p}\bar{n}} = \frac{0.5}{M}\sqrt{M^4 + (m^2_{\bar{n}} - m^2_{\bar{p}})^2 - 2(m^2_{\bar{n}} + m^2_{\bar{p}})M^2} \tag{4.6}$$

where M is the invariant mass of the $\gamma - \bar{D}$ pair, $m_{\bar{n}}$ the mass of the antineutron and $m_{\bar{p}}$ the mass of the antiproton. The $k^*_{\bar{p}\bar{n}}$ distribution obtained through Eq. 4.6 corresponds to the relative momentum that the antiproton–antineutron pair had prior to coalescence. In events where coalescence occurs, the two nucleons do not appear as free final-state particles, but are bound into an antideuteron. Consequently, their original k^* distribution cannot be accessed directly from the hadronic final state. The photon emitted in the radiative formation process carries the necessary kinematic information, allowing an indirect reconstruction of the initial $\bar{p}$–$\bar{n}$ relative momentum distribution, which, as visible in Fig. 4.9, is in agreement with the respective coalescence probability (blue

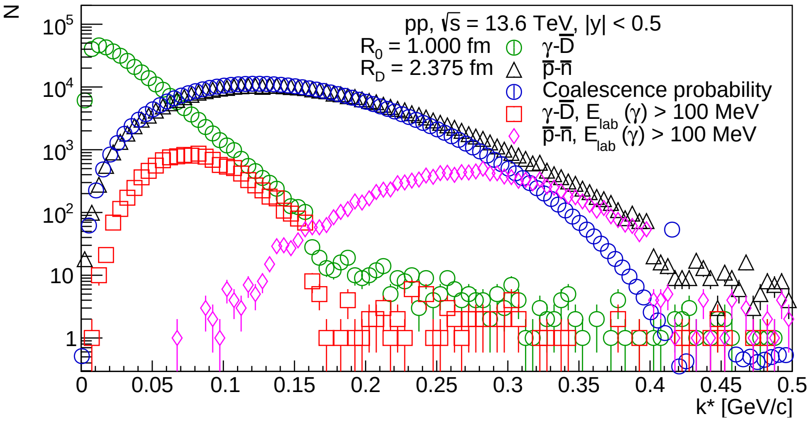

Figure 4.9: Photon-antideuteron ($\gamma - \bar{D}$) and antiproton-antineutron ($\bar{p} - \bar{n}$) k^* distributions. $\gamma - \bar{D}$ is obtained from the fixed R_0 coalescence afterburner configuration. The $\bar{p} - \bar{n}$ distribution is the result of the calculation through Eq. 4.6. The coalescence probability for $\bar{p}$–$\bar{n}$ is shown (blue), while the k^* distribution for photons with laboratory energies greater than 100 MeV is shown (red), while the corresponding $\bar{p}$–$\bar{n}$ k^* distribution obtained from photons in the same laboratory-energy range is shown (magenta).

markers).

By looking at Fig. 4.9, it is possible to observe that the peak of the $\gamma - \bar{D}$ k^* (green points) distribution occurs at a few tens of MeV, which is relatively low. In the rest frame, photons with such energies would be difficult to detect in the laboratory frame. However, thanks to the blueshift discussed in Sec. 3.2.2, a significant fraction of photons in the laboratory frame can reach energies above $100\ \mathrm{MeV}$, as shown in Fig. 4.10 (red dotted line). This is particularly advantageous, since photons with laboratory energies exceeding $100\ \mathrm{MeV}$ are experimentally detectable.
Since not all photons satisfy this requirement, the full γ–$\bar{D}$ k^* distribution (green curve in Fig. 4.9) cannot be reconstructed. The experimentally accessible observable is therefore the γ–D k^* distribution obtained for photons with $E_\gamma^{\mathrm{lab}} > 100$ MeV, shown in red in Fig. 4.9. Through Eq. 4.6, this distribution translates into the corresponding $\bar{p}$–$\bar{n}$ k^* distribution (magenta curve), which therefore represents the expected measurable $\bar{p}$–$\bar{n}$ k^* spectrum. In Fig. 4.10 it is possible to observe a broad correlation between the γ and the $\bar{D}$. The width of such a correlation, as explained in Sec. 3.2.2, depends on the initial k^* of $\bar{p}$–$\bar{n}$ pairs and the angle of emission of the photon in the rest frame.

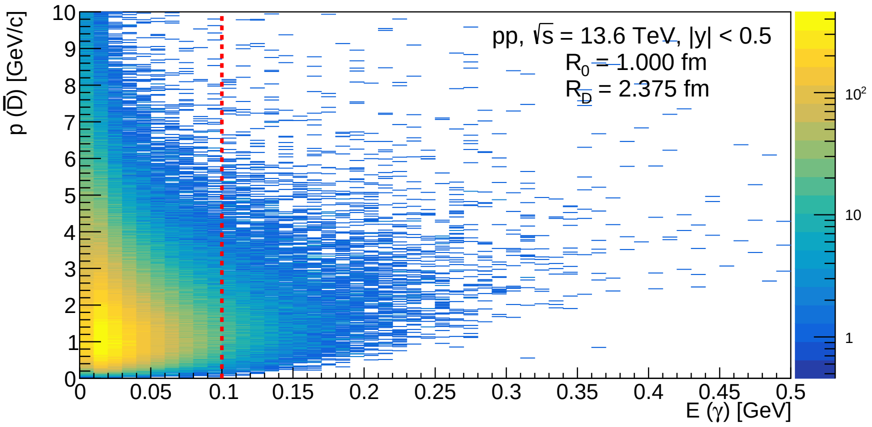

Figure 4.10: Photon-antideuteron ($\gamma - \bar{D}$) distribution obtained from the application of the afterburner with a $R_0 = 1.00$ fm and $R_D = 2.375$ fm on 10^9 pp collisions at $\sqrt{s} = 13.6$ TeV generated with PYTHIA. The red dotted line at $E(\gamma) = 100$ MeV represents the typical γ detection threshold.

4.1.3 Correlation functions for $\overline{\mathrm{p}}$–$\overline{\mathrm{p}}$ and $\overline{\mathrm{p}}$–$\overline{\mathrm{n}}$

The two-particle correlation function $C(k^*)$ is computed as the ratio between the correlated pair distribution and a reference distribution obtained from uncorrelated pairs, as a function of the relative momentum k^*, according to Sec. 1.4.1. The correlation function for $\overline{\mathrm{p}}$–$\overline{\mathrm{p}}$ pairs shown in Fig. 4.11 (left) remains unchanged by switching coalescence on or off, as it is expected since these pairs cannot form bound states. On the contrary, a suppression in the correlation function for $\overline{\mathrm{p}}$–$\overline{\mathrm{n}}$ pairs appears at low k^* as shown in Fig. 4.11 (right), when coalescence is enabled due to the formation of (anti)deuterons, which removes closely spaced pairs. The $C(k^*)$ for $\overline{\mathrm{p}}$–$\overline{\mathrm{n}}$ with coalescence off and for $\overline{\mathrm{p}}$–$\overline{\mathrm{p}}$ (both with coalescence on and off) are similar, both exhibiting a similar peak due to the strong interaction. Besides a small suppression at low k^* of the $C(k^*)$ for $\overline{\mathrm{p}}$–$\overline{\mathrm{p}}$ due to the Coulomb repulsion. The similarity in the peaks is due to the strong interaction, which is similar between $\overline{\mathrm{p}}$ (p) and $\overline{\mathrm{n}}$ (n). Although no data on the $\overline{\mathrm{p}}$–$\overline{\mathrm{n}}$ correlation are available this study represents a proof of concept of how the coalescence mechanism modifies two-particle correlation functions. The same effect is expected in experimentally accessible systems, such as deuteron–proton correlations, where the formation of $^3\mathrm{He}$ would remove low-k^* pairs from the final state, leading to an analogous suppression pattern. Therefore, the present analysis provides a benchmark for future correlation studies involving light nuclei that can be directly reconstructed experimentally.

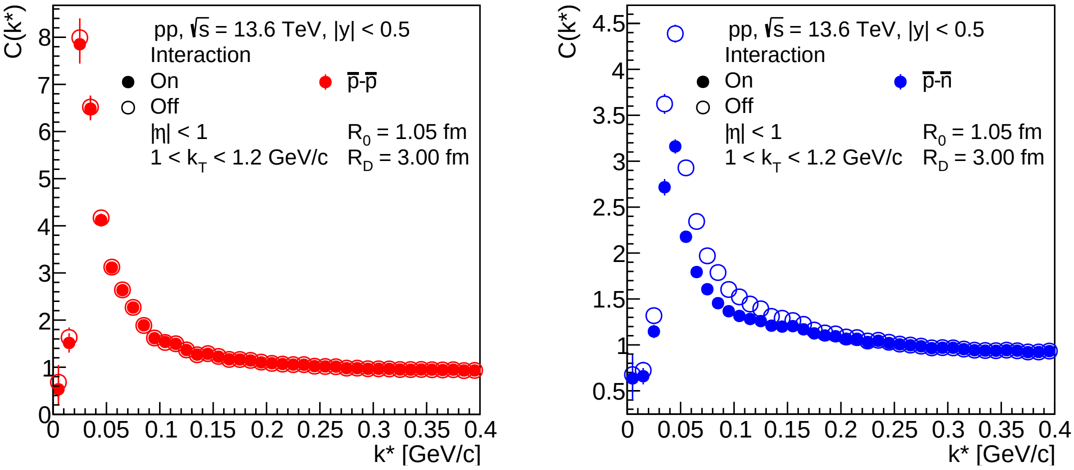

Figure 4.11: Correlation functions $C(k*)$ of nucleon pairs. Left: $\overline{\mathrm{p}}$–$\overline{\mathrm{p}}$ correlations with coalescence on and off. Right: $\overline{\mathrm{p}}$–$\overline{\mathrm{n}}$ correlations with coalescence on and off. The simulation (open markers) is obtained from 10^9 pp collisions at $\sqrt{s} = 13.6$ TeV generated with PYTHIA, followed by the afterburner using the $R_{\text{eff}}(k^*)$ model, with parameters $R_0 = 1.05$ fm and $R_D = 3.00$ fm. The following cuts are applied: pair average transverse momentum 1 GeV$< k_T < 1.2$ GeV and pseudorapidity $|\eta| < 1$.

4.2 Electron-Proton collisions

The application of the afterburner on Electron-Proton collisions (Sec. 3.4) events is first compared to Electron-Proton collisions data from HERA experiment and then the prediction on EIC configuration are presented, considering in both cases the source and deuteron radius found from the fine tuning in pp collisions (Sec. 4.1). The choice to retain the same tuning as in pp collisions is motivated by the following considerations:

1. There are no sufficiently precise data from HERA to repeat the fine tuning.
2. No measurements of the source in ep collisions are available.

4.2.1 HERA

The coalescence parameter B_2 extracted from the (anti)deuteron and (anti)proton simulated spectra for electron–proton collisions at $\sqrt{s} = 318$ GeV is shown in Fig. 4.12. For the fixed-R_0 model, the B_2 distribution for $\overline{D}$ is compatible with the ZEUS data [67] up to $p_T/M \approx 0.5$. At higher values of p_T/M, the simulation remains consistent at the level of the order of magnitude (blue markers in Fig. 4.12). For D, the simulated B_2

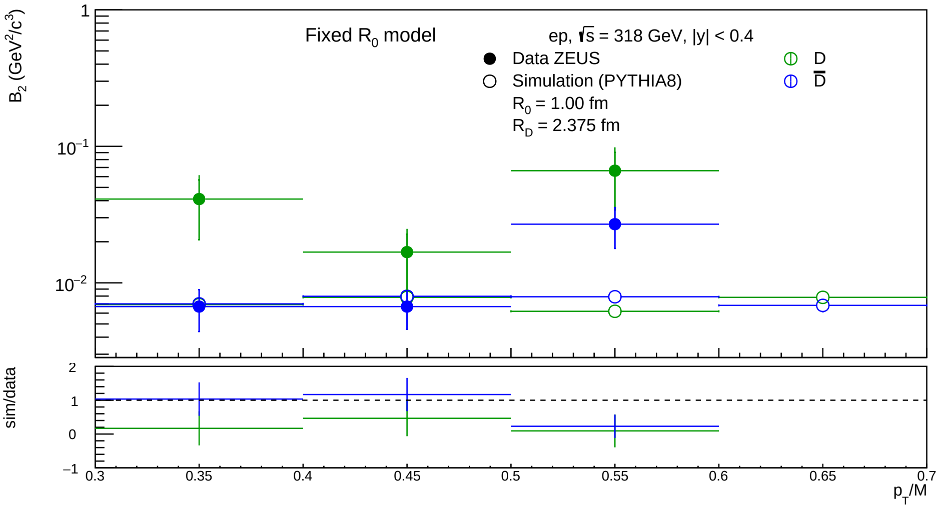

Figure 4.12: B_2 distribution (top panel) as a function of p_T/M (transverse momentum over nuclear mass) at midrapidity ($|y| < 0.4$) for D and $\overline{D}$. The simulation (open markers) is obtained from $2 \cdot 10^9$ ep collisions at $\sqrt{s} = 318$ GeV generated with PYTHIA, followed by the afterburner with parameters $R_0 = 1.00$ fm and $R_D = 2.375$ fm. These values represent the optimal set of parameters obtained from the χ^2-minimisation procedure described in the "Fine tuning" subsection. The data (full markers) are from [67]. The ratio between simulation and data is shown in the bottom panel.

values are likewise consistent with the experimental measurements within the same order of magnitude over the explored kinematic range (green markers in Fig. 4.12). The model reproduces the expected symmetry between $B_2(D)$ and $B_2(\overline{D})$. This symmetry is a direct consequence of the coalescence mechanism and is expected in the HERA data as the measurements are performed at midrapidity, where the net-baryon asymmetry of the proton projectile does not influence the production yields. The corresponding B_2 distribution obtained with the $R_{\text{eff}}(k^*)$ model is presented in Fig. 4.13. The results obtained within this framework lead to the same conclusions as in the fixed-R_0 scenario: the description of both D and $\overline{D}$ production is compatible with the ZEUS data up to $p_T/M = 0.5$ and remains consistent at the level of the order of magnitude at higher transverse momenta. In addition, the symmetry between matter and antimatter is preserved in this implementation. The lower panels of Figs. 4.12 and 4.13 display the ratio between simulation and data, quantitatively illustrating the level of agreement discussed above.

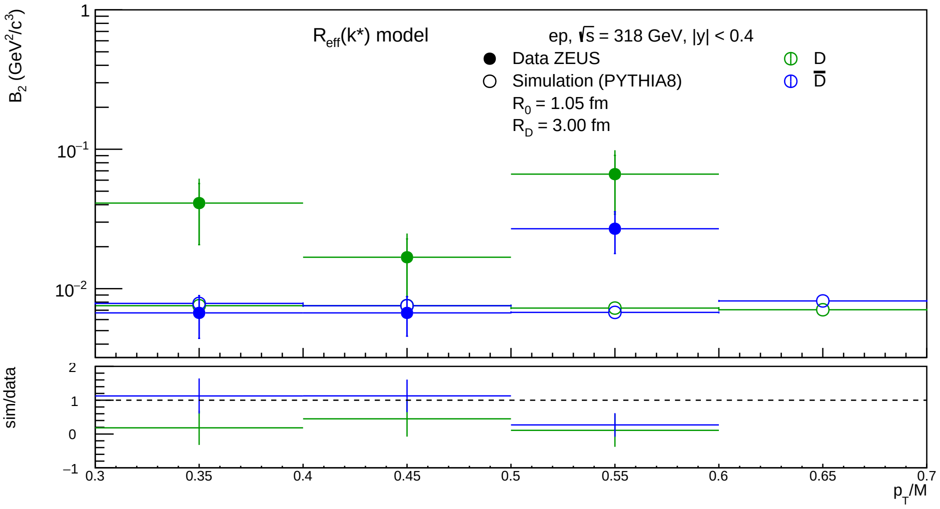

Figure 4.13: B_2 distribution (top panel) as a function of p_T/M (transverse momentum over nuclear mass) at midrapidity ($|y| < 0.4$) for D and $\overline{D}$. The simulation (open markers) is obtained from $2 \cdot 10^9$ ep collisions at $\sqrt{s} = 318$ GeV generated with PYTHIA, followed by the afterburner using the $R_{\text{eff}}(k^*)$ model, with parameters $R_0 = 1.05$ fm and $R_D = 3.00$ fm. These values represent the optimal set of parameters obtained from the χ^2-minimisation procedure described in the "Fine tuning" subsection. The data (full markers) are from [67]. The ratio between simulation and data is shown in the bottom panel.

4.2.2 EIC

We now turn to predictions for the Electron–Ion Collider (EIC), a future facility that will collide electrons with high-energy protons and nuclei [99]. A key advantage of deep inelastic scattering (DIS) experiments at the EIC is the possibility to vary the resolution scale of the probe, which is determined by the virtuality of the exchanged photon, Q^2. In deep inelastic scattering by selecting events with different Q^2 thresholds, one can investigate light-nuclei production as a function of the momentum transfer, thereby gaining insight into both the hadronization mechanism and the partonic structure of the proton. In the following, we present predictions for deuteron and antideuteron production at the EIC for two distinct Q^2 intervals.

The variable Q^2 is defined as the negative squared four-momentum transferred by the exchanged virtual photon, $Q^2 = -q^2$. Larger values of Q^2 correspond to shorter distance scales, allowing one to resolve the proton's partonic substructure with increasing precision.

The following results are obtained from a sample of simulated ep collisions with a proton beam energy of $130\ \mathrm{GeV}$ and an electron beam energy of 10 GeV that correspond to $\sqrt{s} = 72$ GeV. A total of 10^9 events is generated with PYTHIA and processed through the afterburner.

Since the DIS cross section decreases rapidly with increasing Q^2, the effective integrated luminosity corresponding to 10^9 simulated events depends on the chosen Q^2 threshold. Table 4.2 reports the integrated cross sections above different Q^2 thresholds together with the corresponding expected number of events, computed assuming an integrated luminosity of $\mathcal{L} = 5.33\ \mathrm{fb}^{-1}$, corresponding to the first year of EIC data taking. As expected, the event yield decreases significantly when increasing the Q^2 threshold, reflecting the rapid reduction of the cross section in this kinematic region. In Figs. 4.14 and 4.15, the pseudorapidity distribution of produced D is found to be larger than that of $\overline{D}$. In the forward region (the proton-going direction), a clear asymmetry between nuclei and antinuclei production is observed, which originates from the baryon-number transport from the incoming proton. The red dotted lines in Figs. 4.14 and 4.15 indicate the pseudorapidity coverage of the future ePIC dual RICH (dRICH) detector [99], which could be used to identify $\overline{D}$ in future analyses.

Q^2 [GeV^2]	Cross section $[\mathrm{mb}]$	number of events
$Q^2 > 1$	1.827×10^{-1}	9.7×10^{11}
$Q^2 > 5$	2.340×10^{-2}	1.2×10^{11}
$Q^2 > 10$	1.029×10^{-3}	5.5×10^{9}
$Q^2 > 20$	4.938×10^{-4}	2.6×10^{9}

Table 4.2: Cross sections above different Q^2 thresholds and the corresponding expected number of events, assuming an integrated luminosity of $L = 5.33\,\mathrm{fb}^{-1}$, corresponding to the first year of EIC data taking.

From Figs. 4.14 and 4.15, it is possible to estimate the number of deuterons and antideuterons expected in the first year of EIC data taking. For $Q^2 > 1\ \mathrm{GeV}^2$, rescaling from the simulated luminosity to $\mathcal{L} = 5.33\,\mathrm{fb}^{-1}$ corresponds to approximately 6.7×10^7 deuteron events and 2.8×10^6 antideuteron events in the full pseudorapidity range. Within the dRICH acceptance ($1.5 < |\eta| < 3.5$), the expected yields are approximately 6.01×10^5 deuterons and 1.26×10^5 antideuterons.
For $Q^2 > 20\ \mathrm{GeV}^2$, the same rescaling gives approximately 2.45×10^5 deuteron events and 2.6×10^4 antideuteron events in the full pseudorapidity range. Within the dRICH acceptance, the expected yields are approximately 4.1×10^4 deuterons and 1.2×10^4 antideuterons.

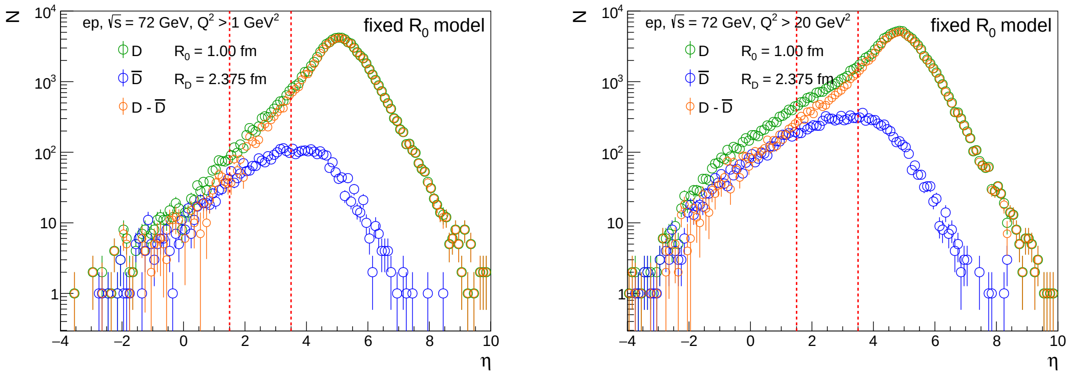

(a)

(b)

Figure 4.14: Pseudorapidity distributions of D (green), $\overline{D}$ (blue), and their difference (orange) for ep collisions simulated with a proton beam energy of 130 GeV and an electron beam energy of 10 GeV, corresponding to $\mathcal{L} = 5.33\,\mathrm{fb}^{-1}$. Events are generated with PYTHIA with photon virtuality (a) $Q^2 > 1$ GeV^2 and (b) $Q^2 > 20$ GeV^2, followed by the afterburner (R_0 fixed) with parameters $R_0 = 1.00$ fm and $R_D = 2.375$ fm. The red dotted lines indicate the ePIC dRICH acceptance, $1.5 < |\eta| < 3.5$.

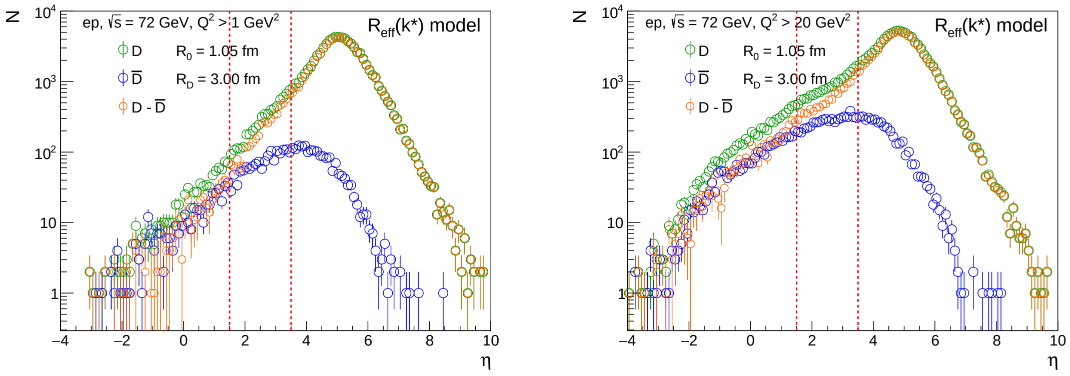

(a)

(b)

Figure 4.15: Same as Fig. 4.14, but using the $R_{\text{eff}}(k^*)$ model, with parameters $R_0 = 1.05$ fm and $R_D = 3.00$ fm.

In Figs. 4.16, the predicted B_2 distributions are shown as a function of p_T/A within the dRICH acceptance region $1.5 < \eta < 3.5$ for ep collisions at $\sqrt{s} = 72$ GeV, considering two intervals of photon virtuality: (a) $Q^2 > 1\,\mathrm{GeV}^2$ and (b) $Q^2 > 20\,\mathrm{GeV}^2$. The results are obtained within the afterburner coalescence model using a source radius $R_0 = 1.00$ fm and a deuteron radius $R_D = 2.375$ fm. Figure 4.17 shows the corresponding distribu-

tions obtained with the fixed kinetic energy implementation of the model, assuming $R_0 = 1.05$ fm and $R_D = 3.00$ fm.
In the low-virtuality case ($Q^2 > 1\,\mathrm{GeV}^2$), B_2 decreases rapidly at small p_T/A, reaches a minimum around 0.6–0.8 GeV$/c$, and then exhibits a mild rise toward higher transverse momenta. For $Q^2 > 20\,\mathrm{GeV}^2$, the behavior changes: after a minimum at intermediate p_T/A, a more pronounced increase of B_2 is observed at large transverse momentum.

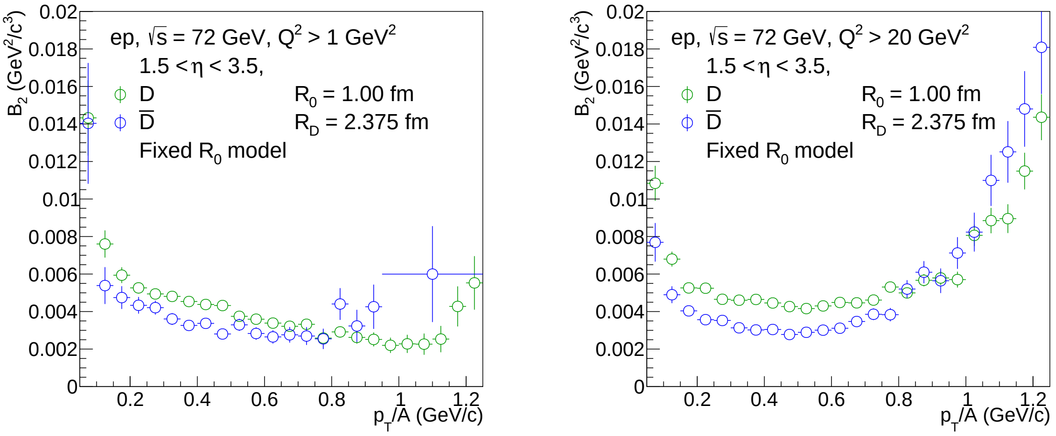

(a) (b)

Figure 4.16: B_2 as a function of p_T/A within the dRICH acceptance region. The simulation is based on 10^9 ep collisions with a proton beam energy of 130 GeV and an electron beam energy of 10 GeV. Events are generated with PYTHIA with photon virtuality (a) $Q^2 > 1$ GeV^2 and (b) $Q^2 > 20$ GeV^2, followed by the afterburner using the model with fixed R_0 with parameters $R_0 = 1.00$ fm and $R_D = 2.375$ fm.

Up to this point, a prediction for (anti)deuteron production has been presented. However, it is equally important to investigate the feasibility of their detection. In Fig. 4.18, the distribution of the number of deuterons is shown as a function of pseudorapidity η and transverse momentum p_T within the dRICH configuration, corresponding to an acceptance region of $1.5 < \eta < 3.5$, as indicated on the vertical axis. Since the dRICH detector relies on Cherenkov radiation, the threshold curve for Cherenkov emission is given by

$$\eta = \operatorname{arcsinh}\left(\frac{p_{th}}{p_T}\right), \tag{4.7}$$

where p_{th} is the threshold momentum for Cherenkov emission, defined as

$$p_{th} = \frac{m}{\sqrt{n^2 - 1}}, \tag{4.8}$$

with m being the particle mass (deuteron or proton) and n the refractive index of the radiator medium. Figure 4.18 shows two threshold curves: one for deuterons (red line)

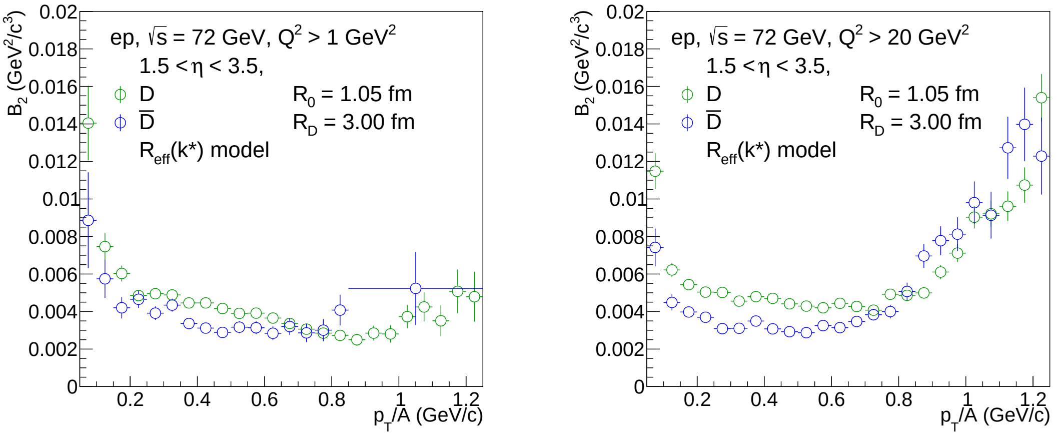

(a) (b)

Figure 4.17: B_2 as a function of p_T/A within the dRICH acceptance region. The simulation is based on 10^9 ep collisions with a proton beam energy of 130 GeV and an electron beam energy of 10 GeV. Events are generated with PYTHIA with photon virtuality (a) $Q^2 > 1$ GeV^2 and (b) $Q^2 > 20$ GeV^2, followed by the afterburner using the $R_{\text{eff}}(k^*)$ model, with parameters $R_0 = 1.05$ fm and $R_D = 3.00$ fm.

and one for protons (black line), for two different refractive indices (top and bottom panels), $n = 1.02$ and $n = 1.03$, which correspond to the limiting values of the refractive index of the dRICH radiator [100]. If a deuteron lies above its Cherenkov threshold curve, it will emit Cherenkov radiation and can therefore be detected. Similarly, protons (or any lighter particles) above their corresponding threshold will also produce Cherenkov radiation. A key feature is the separation between the proton and deuteron threshold curves. In the region between the black and red lines, deuterons can be identified through a veto technique: if no Cherenkov radiation is observed, the particle must be heavier than a proton. In this kinematic region, the most probable candidate is the deuteron. Although heavier nuclei such as ^{3}He could also satisfy this condition, their production rate is approximately three orders of magnitude lower than that of deuterons, making their contribution statistically negligible. The main limitation arises from protons lying below their Cherenkov threshold curve, as they do not emit Cherenkov radiation and may therefore contaminate the deuteron sample. In Fig. 4.18, only the case with $Q^2 > 20$ GeV^2 and coalescence modeled using the fixed R_0 approach is shown, but the same Cherenkov threshold curves and identification strategy can be applied to other Q^2 selections and to the $R_{\text{eff}}(k^*)$ model.

From Fig. 4.18, it is also possible to determine a lower limit on p_T/A for (anti)deuterons entering the B_2 analysis (with $A = 2$), arising from the experimental acceptance in p_T/A. In particular, considering $\eta = 3.5$, the minimum transverse momentum required

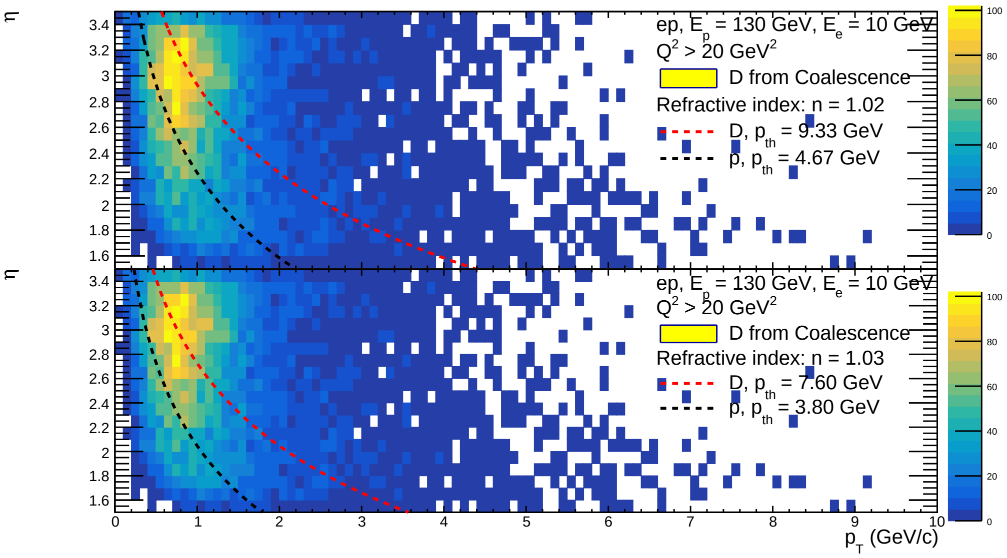

Figure 4.18: Number of deuterons produced via coalescence as a function of pseudorapidity (η) and transverse momentum (p_T) within the dRICH configuration for a $Q^2 > 20$ GeV^2. The dashed lines indicate the Cherenkov detection thresholds for deuterons (red dashed line) and protons (black dashed line). The top panel shows the Cherenkov threshold curves for a refractive index $n = 1.02$ [99], while the bottom panel corresponds to $n = 1.03$. The corresponding momentum thresholds for Cherenkov emission are also displayed.

for deuteron Cherenkov emission is approximately $p_T \simeq 0.75$ GeV, which corresponds to a minimum detectable transverse momentum per nucleon of $p_T/A \approx 0.38$ GeV.

Conclusions

The aim of this thesis was to develop a model for the description of light (anti)nucleus formation in high-energy collisions, consistently treating both coalescence and nucleon–nucleon (N–N) interactions. For this purpose, a model was implemented and coupled through an afterburner to PYTHIA8 event samples, allowing the study of proton–proton and electron–proton collisions within the same theoretical and computational setup.

The coalescence mechanism was formulated in two equivalent approaches: a wave-function-based formalism, where the formation probability is computed through the scalar product between a Gaussian source and the nuclear bound-state wave function, and a Wigner-function formalism based on the phase-space overlap of the source and bound-state distributions. In parallel, N–N interactions were incorporated through a semiclassical energy-conservation prescription, ensuring consistency between the initial kinematics provided by the event generator and the effective source radius entering the calculation. The framework was extended iteratively to describe the formation of nuclei and antinuclei up to $A = 4$, including the treatment of photon emission associated with the transition from a correlated nucleon pair to a bound state.

The model was first applied to proton–proton collisions at $\sqrt{s} = 13.6$ TeV. Transverse-momentum spectra of $\overline{p}$, $\overline{D}$, $\overline{T}$, $^3\overline{\mathrm{He}}$, and $^4\overline{\mathrm{He}}$ were obtained and compared to ALICE measurements. The coalescence parameters B_2 and B_3 were extracted from the simulated spectra. A grid-based χ^2 minimisation procedure was performed to constrain the source radius R_0 and the deuteron radius R_D, providing best-fit values, uncertainties, and correlation coefficients. The results show a clear anticorrelation between the two parameters and demonstrate that both model implementations reproduce the experimental B_2 distribution within uncertainties. The B_3 observable, although not directly used in the tuning procedure, was found to be qualitatively consistent with the available data, supporting the robustness of the iterative coalescence approach.

The associated photon production from (anti)deuteron formation was investigated, showing that the γ–$\bar{d}$ kinematics can be exploited to reconstruct the pre-coalescence $\bar{p}$–$\bar{n}$ relative-momentum distribution. This result highlights the possibility of accessing information on the initial nucleon correlations that are otherwise hidden once the bound state is formed. Furthermore, the interplay between coalescence and final-state interactions was studied through two-particle correlation functions $C(k^*)$. By comparing scenarios with coalescence switched on and off, a suppression of low-k^* $\bar{p}$–$\bar{n}$ pairs was observed, directly quantifying the depletion induced by bound-state formation. This effect provides a conceptual benchmark for future femtoscopic studies involving light nuclei and offers a direct handle on the competition between clustering and final-state interactions.

The model was subsequently tested against electron–proton collision data. At a center-of-mass energy of $\sqrt{s} = 318$ GeV, the simulated B_2 distributions for D and $\overline{D}$ were compared to ZEUS data, showing compatibility within the explored kinematic range and preserving the expected symmetry between matter and antimatter at midrapidity. Building on this validation, predictions were provided for the future Electron–Ion Collider. Pseudorapidity-dependent yields of deuterons and antideuterons were obtained for different photon-virtuality selections, together with B_2 distributions within the acceptance of the future ePIC dual RICH (dRICH) detector. Using the design refractive indices of the dRICH radiators, the Cherenkov threshold curves were evaluated, showing that deuteron identification is feasible in specific kinematic regions within the detector acceptance and allowing the determination of the corresponding lower limits in p_T/A for experimental analyses.

In conclusion, the significance of this work lies in the establishment of a coherent and flexible framework capable of describing light-(anti)nucleus formation across different collision systems and kinematic regimes. By linking coalescence probabilities, nucleon correlations, and measurable observables such as B_2, B_3, and $C(k^*)$, the present study contributes to a deeper understanding of the mechanisms governing the formation of loosely bound states in high-energy collisions.

Appendix A

Appendix

A.1 Antinuclei Distributions Before Reweighting

In Fig. A.1 the spectra with and without the reweight are shown compared to data with the respective ratios. In the very low transverse momentum region ($p_{\mathrm{T}} = 0.6$–$0.8\ \mathrm{GeV}/c$), both Data/Reweighted simulation and Data/not reweighted simulation deviate significantly from unity, by approximately 30–40% and 35–45%, respectively. In the interval 1–$3\ \mathrm{GeV}/c$, the Data/Reweighted simulation ratio remains within approximately 10–20% of unity (typically around 0.8–0.9), while Data/not reweighted simulation shows a comparable but slightly larger deviation, of order 15–20%. In this range, the reweighted simulation provides a marginally better description of the data. The difference becomes more pronounced at higher p_{T}. Between 3 and $5\ \mathrm{GeV}/c$, Data/Reweighted simulation stays within about 15–20% of unity, whereas Data/not reweighted simulation deviates by roughly 20–25% below 1. Above $6\ \mathrm{GeV}/c$, the trends clearly separate: the Data/Reweighted simulation ratio remains within about 20% of unity up to $\sim 8\ \mathrm{GeV}/c$ and increases to a deviation of roughly $+20$–30% in the highest p_{T} bin. In contrast, Data/not reweighted simulation decreases to about -40% already around $7\ \mathrm{GeV}/c$ and reaches deviations of the order of -50% at the highest p_{T} values (~ 9–$10\ \mathrm{GeV}/c$). The ratio Reweighted simulation/not reweighted simulation directly quantifies the size of the reweighting effect. It is within 10% of unity up to about 2–$3\ \mathrm{GeV}/c$, increases to 10–15% in the 3–$5\ \mathrm{GeV}/c$ range, and becomes substantial above $6\ \mathrm{GeV}/c$, where the reweighted spectra are reduced by roughly 30–50% relative to the not reweighted ones at the highest p_{T}. Overall, the Data/Reweighted simulation ratio is systematically closer to unity than Data/not reweighted simulation, especially at intermediate and high p_{T}. While the not reweighted simulation deviates by up to $\sim 50\%$ at large p_{T}, the reweighted spectra remain within about 20–30% of unity over most of the measured range. This demonstrates that the reweighting procedure significantly improves the agreement between data and simulation, particularly at high transverse momentum. this hold also for Fig. A.2.

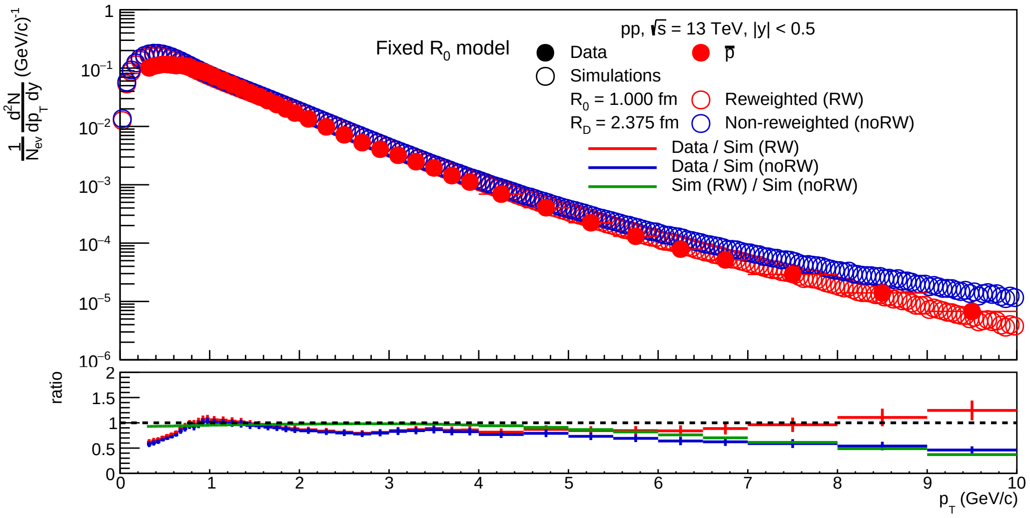

Figure A.1: Transverse momentum (p_T) distributions of $\overline{p}$ at midrapidity ($|y| < 0.5$). Simulated distributions (open markers) are obtained from 10^9 pp collisions at $\sqrt{s} = 13.6$ TeV generated with PYTHIA, followed by the afterburner with fixed R_0 model, with parameters $R_0 = 1.00$ fm and $R_D = 2.375$ fm. The results are shown before (blue) and after (red) the reweighting procedure. Experimental data (full markers) are from ALICE [132, 22]. The bottom panel shows the ratio of data to simulation before and after the reweighting, as well as the ratio between the simulations before and after the reweighting.

A.2 Hessian Method

Since the χ^2 is evaluated on a discrete grid of points in the parameter space (R_D, R_0), the minimum value χ^2_{min} is identified as the smallest χ^2 among all grid points. The corresponding parameter values are denoted as $\hat{R}_D$ and $\hat{R}_0$, i.e.:

$$(\hat{R}_D, \hat{R}_0) = \arg \min_{R_D, R_0} \chi^2(R_D, R_0), \qquad \chi^2_{\text{min}} = \chi^2(\hat{R}_D, \hat{R}_0). \tag{A.1}$$

In the vicinity of the minimum, the χ^2 function can be approximated by a second-order Taylor expansion:

$$\chi^2(\theta) \approx \chi^2_{\text{min}} + \frac{1}{2}(\theta - \hat{\theta})^T H(\theta - \hat{\theta}), \tag{A.2}$$

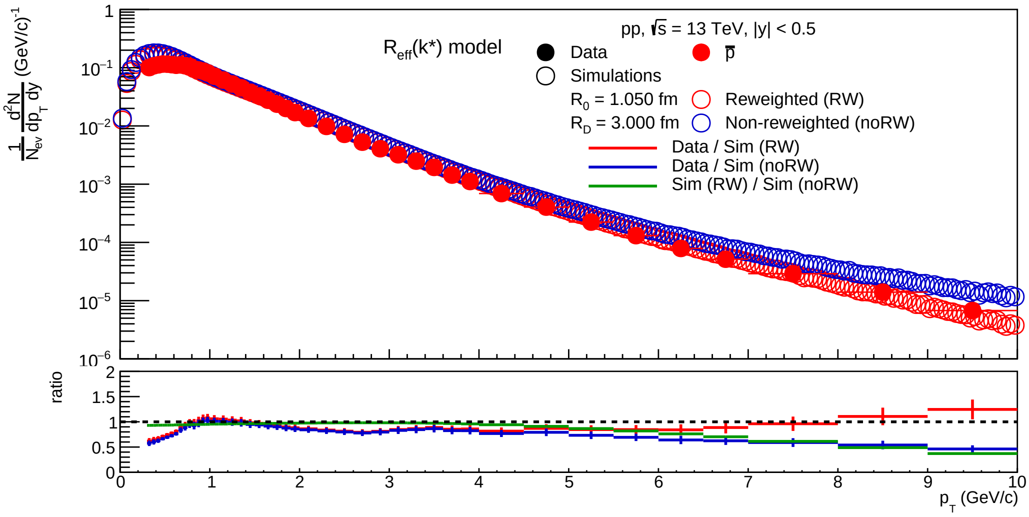

Figure A.2: Transverse momentum (p_T) distributions of $\overline{p}$ at midrapidity ($|y| < 0.5$). The simulated distributions (open markers) are obtained from 10^9 pp collisions at $\sqrt{s} = 13.6$ TeV generated with PYTHIA, followed by the afterburner using the fixed R_{eff} model, with parameters $R_0 = 1.05$ fm and $R_D = 3.00$ fm. The results are shown before (blue) and after (red) the reweighting procedure. Experimental data (full markers) are from ALICE [132, 22]. The bottom panel shows the ratio of data to simulation before and after the reweighting, as well as the ratio between the simulations before and after the reweighting.

where $\theta = (R_D, R_0)^T$, $\hat{\theta} = (\hat{R}_D, \hat{R}_0)^T$, and H is the Hessian matrix evaluated at the minimum:

$$H = \begin{pmatrix} H_{11} & H_{12} \\ H_{12} & H_{22} \end{pmatrix} = \begin{pmatrix} \dfrac{\partial^2 \chi^2}{\partial R_D^2} & \dfrac{\partial^2 \chi^2}{\partial R_D \partial R_0} \\ \dfrac{\partial^2 \chi^2}{\partial R_0 \partial R_D} & \dfrac{\partial^2 \chi^2}{\partial R_0^2} \end{pmatrix}_{\hat{\theta}} . \tag{A.3}$$

Since the χ^2 is only known at discrete grid points, the second derivatives are computed numerically using finite difference formulas. Let ΔR_D and ΔR_0 be the grid steps along the R_D and R_0 directions, respectively. The diagonal elements of the Hessian are given by:

$$H_{11} \approx \frac{\chi^2(\hat{R}_D + \Delta R_D, \hat{R}_0) - 2\chi^2_{\text{min}} + \chi^2(\hat{R}_D - \Delta R_D, \hat{R}_0)}{(\Delta R_D)^2}, \tag{A.4}$$

$$H_{22} \approx \frac{\chi^2(\hat{R}_D, \hat{R}_0 + \Delta R_0) - 2\chi^2_{\text{min}} + \chi^2(\hat{R}_D, \hat{R}_0 - \Delta R_0)}{(\Delta R_0)^2}. \tag{A.5}$$

The off-diagonal element is computed using a mixed second-order derivative formula:

$$\begin{aligned} H_{12} \approx \frac{1}{4\Delta R_D \Delta R_0} \big[& \chi^2(\hat{R}_D + \Delta R_D, \hat{R}_0 + \Delta R_0) \\ & - \chi^2(\hat{R}_D + \Delta R_D, \hat{R}_0 - \Delta R_0) \\ & - \chi^2(\hat{R}_D - \Delta R_D, \hat{R}_0 + \Delta R_0) \\ & + \chi^2(\hat{R}_D - \Delta R_D, \hat{R}_0 - \Delta R_0) \big]. \end{aligned} \tag{A.6}$$

Once the Hessian matrix is determined, the covariance matrix Σ is obtained as its inverse:

$$\Sigma = H^{-1} = \frac{1}{\det H} \begin{pmatrix} H_{22} & -H_{12} \\ -H_{12} & H_{11} \end{pmatrix}, \tag{A.7}$$

where the determinant is given by:

$$\det H = H_{11} H_{22} - H_{12}^2. \tag{A.8}$$

The statistical uncertainties on the parameters R_D and R_0 are then extracted from the diagonal elements of the covariance matrix:

$$\sigma_{R_D} = \sqrt{\Sigma_{11}} = \sqrt{\frac{H_{22}}{\det H}}, \qquad \sigma_{R_0} = \sqrt{\Sigma_{22}} = \sqrt{\frac{H_{11}}{\det H}}. \tag{A.9}$$

Finally, the correlation coefficient between R_D and R_0 is given by:

$$\rho = \frac{\Sigma_{12}}{\sigma_{R_D} \sigma_{R_0}} = \frac{-H_{12}}{\sqrt{H_{11} H_{22}}}. \tag{A.10}$$

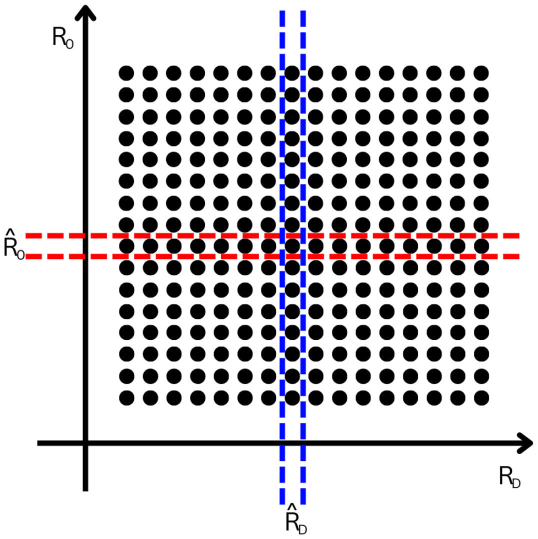

Figure A.3: Example of the χ^2 grid as a function of R_D and R_0. The projection of $\chi^2(R_0)$ at the best-fit value $\hat{R}_D$ (the value of R_D that minimises χ^2) is shown between the blue lines, while the projection of $\chi^2(R_D)$ at the best-fit value $\hat{R}_0$ (the value of R_0 that minimises χ^2) is shown between the red lines.

A.3 Fit Method

As shown in Fig. A.3, starting from the χ^2 grid, projections are obtained by fixing R_D (leaving R_0 as a free parameter) and R_0 (leaving R_D as a free parameter) at the values that minimise χ^2, denoted as $\hat{R}_D$ and $\hat{R}_0$, respectively. In this way, two one-dimensional curves are obtained and fitted with the function:

$$f_{R_i} = \chi^2_{\min} \left(1 + (x \leq \hat{R}_i) \frac{(x - \hat{R}_i)^2}{\sigma_L^2} + (x > \hat{R}_i) \frac{(x - \hat{R}_i)^2}{\sigma_R^2} \right), \qquad i = 0, D \quad \text{(A.11)}$$

The fitting results are shown in Fig. A.4 and Fig. A.5, and the corresponding parameter values are also reported in Tab. 4.1.

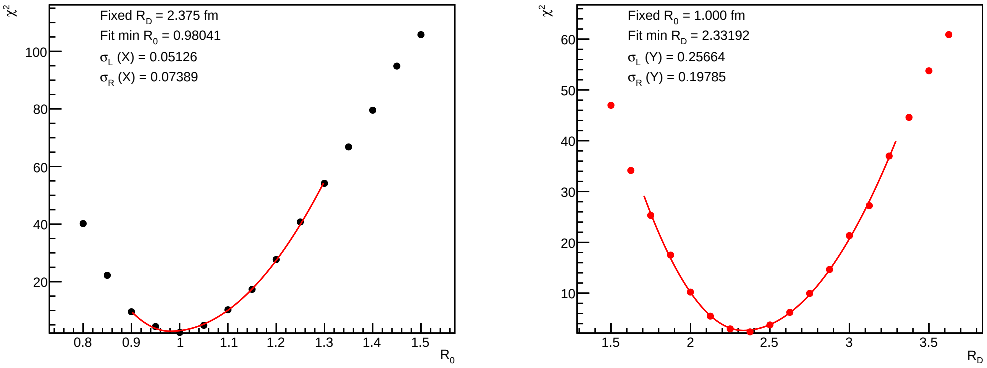

Figure A.4: Fitting results obtained with the model with fixed R_0.

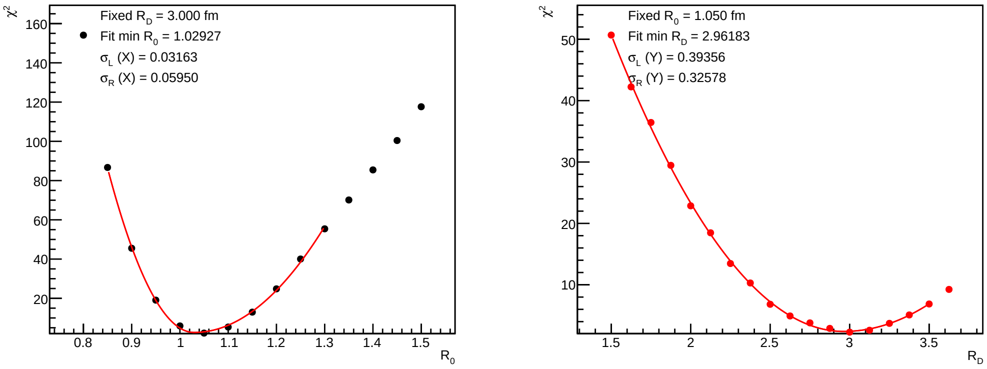

Figure A.5: Fitting results obtained with the fixed R_{eff} model.

Bibliography

[1] Schuster, Arthur. “Potential Matter.—A Holiday Dream”. In: *Nature* 58.1503 (1898), p. 367. doi: `10.1038/058367a0`. url: `https://doi.org/10.1038/058367a0`.

[2] Paul Adrien Maurice Dirac. “The quantum theory of the electron”. In: *Proceedings of the Royal Society of London. Series A, Containing Papers of a Mathematical and Physical Character* 117.778 (Feb. 1928), pp. 610–624.

[3] Mark Thomson. *Modern particle physics*. New York: Cambridge University Press, Oct. 2013. isbn: 978-1-107-03426-6, 978-1-139-52536-7. doi: `10.1017/CBO9781139525367`.

[4] C. D. Anderson. “The Positive Electron”. In: *Phys. Rev.* 43 (1933), pp. 491–494. doi: `10.1103/PhysRev.43.491`.

[5] O. Chamberlain et al. “Observation of Anti-protons”. In: *Phys. Rev.* 100 (1955), pp. 947–950. doi: `10.1103/PhysRev.100.947`.

[6] C. S. Wu et al. “Experimental Test of Parity Conservation in β Decay”. In: *Phys. Rev.* 105 (1957), pp. 1413–1414. doi: `10.1103/PhysRev.105.1413`.

[7] Thomas Massam et al. “Experimental observation of antideuteron production”. In: *Nuovo Cimento* 39 (1965), pp. 10–14. doi: `10.1007/BF02814251`. url: `https://cds.cern.ch/record/345976`.

[8] D. E. Dorfan et al. “Search for Massive Particle”. In: *Phys. Rev. Lett.* 14 (1965), p. 999. doi: `10.1103/PhysRevLett.14.999`.

[9] D. E. Dorfan et al. “Observation of antideuterons”. In: *Phys. Rev. Lett.* 14 (1965), pp. 1003–1006. doi: `10.1103/PhysRevLett.14.1003`.

[10] Yu.M. Antipov *et al*. “Observation of antihelium-3”. In: *Nuclear Physics B* 31.2 (1971), pp. 235–252. issn: 0550-3213. doi: `https://doi.org/10.1016/0550-3213(71)90228-8`. url: `https://www.sciencedirect.com/science/article/pii/0550321371902288`.

[11] N. K. Vishnevsky et al. “Observation of antitritium”. In: *Yad. Fiz.* 20 (1974), pp. 694–708.

[12] V. I. Kolesnikov. "Anti-nuclei and nuclei production in Pb+Pb collisions at CERN SPS energies". In: *J. Phys. Conf. Ser.* 110 (2008). Ed. by Roger Barlow, p. 032010. doi: `10.1088/1742-6596/110/3/032010`. arXiv: `0710.5118 [nucl-ex]`.

[13] M. Harrison, T. Ludlam, and S. Ozaki. "RHIC project overview". In: *Nucl. Instrum. Meth. A* 499 (2003), pp. 235–244. doi: `10.1016/S0168-9002(02)01937-X`.

[14] K. Adcox et al. "Formation of dense partonic matter in relativistic nucleus-nucleus collisions at RHIC: Experimental evaluation by the PHENIX collaboration". In: *Nucl. Phys. A* 757 (2005), pp. 184–283. doi: `10.1016/j.nuclphysa.2005.03.086`. arXiv: `nucl-ex/0410003`.

[15] John Adams et al. "Experimental and theoretical challenges in the search for the quark gluon plasma: The STAR Collaboration's critical assessment of the evidence from RHIC collisions". In: *Nucl. Phys. A* 757 (2005), pp. 102–183. doi: `10.1016/j.nuclphysa.2005.03.085`. arXiv: `nucl-ex/0501009`.

[16] C. Adler et al. "Anti-deuteron and anti-He-3 production in s(NN)**(1/2) = 130-GeV Au+Au collisions". In: *Phys. Rev. Lett.* 87 (2001). [Erratum: Phys.Rev.Lett. 87, 279902 (2001)], p. 262301. doi: `10.1103/PhysRevLett.87.262301`. arXiv: `nucl-ex/0108022`.

[17] H. Agakishiev et al. "Observation of the antimatter helium-4 nucleus". In: *Nature* 473 (2011). [Erratum: Nature 475, 412 (2011)], p. 353. doi: `10.1038/nature10079`. arXiv: `1103.3312 [nucl-ex]`.

[18] B. Alper et al. "Large angle production of stable particles heavier than the proton and a search for quarks at the cern intersecting storage rings". In: *Phys. Lett. B* 46 (1973), pp. 265–268. doi: `10.1016/0370-2693(73)90700-4`.

[19] British-Scandinavian-MIT Collaboration. "Production of deuterons and antideuterons in proton-proton collisions at the CERN ISR". In: *Lettere al Nuovo Cimento* 21.6 (1978), pp. 189–194. doi: `10.1007/BF02822248`. url: `https://doi.org/10.1007/BF02822248`.

[20] Shreyasi Acharya et al. "Production of deuterons, tritons, ^{3}He nuclei and their antinuclei in pp collisions at $\sqrt{s}$ = 0.9, 2.76 and 7 TeV". In: *Phys. Rev. C* 97.2 (2018), p. 024615. doi: `10.1103/PhysRevC.97.024615`. arXiv: `1709.08522 [nucl-ex]`.

[21] E. Abbas et al. "Mid-rapidity anti-baryon to baryon ratios in pp collisions at $\sqrt{s}$ = 0.9, 2.76 and 7 TeV measured by ALICE". In: *Eur. Phys. J. C* 73 (2013), p. 2496. doi: `10.1140/epjc/s10052-013-2496-5`. arXiv: `1305.1562 [nucl-ex]`.

[22] Shreyasi Acharya et al. "Production of light (anti)nuclei in pp collisions at $\sqrt{s}$ = 13 TeV". In: *JHEP* 01 (2022), p. 106. doi: `10.1007/JHEP01(2022)106`. arXiv: `2109.13026 [nucl-ex]`.

[23] Shreyasi Acharya et al. “Measurement of the production and elliptic flow of (anti)nuclei in Xe-Xe collisions at sNN=5.44 TeV”. In: *Phys. Rev. C* 110.6 (2024), p. 064901. doi: `10.1103/PhysRevC.110.064901`. arXiv: `2405.19826 [nucl-ex]`.

[24] Shreyasi Acharya et al. “Light (anti)nuclei production in Pb-Pb collisions at sNN=5.02 TeV”. In: *Phys. Rev. C* 107.6 (2023), p. 064904. doi: `10.1103/PhysRevC.107.064904`. arXiv: `2211.14015 [nucl-ex]`.

[25] Jaroslav Adam et al. “Production of light nuclei and anti-nuclei in pp and Pb-Pb collisions at energies available at the CERN Large Hadron Collider”. In: *Phys. Rev. C* 93.2 (2016), p. 024917. doi: `10.1103/PhysRevC.93.024917`. arXiv: `1506.08951 [nucl-ex]`.

[26] Shreyasi Acharya et al. “Measurement of deuteron spectra and elliptic flow in Pb–Pb collisions at $\sqrt{s_{\mathrm{NN}}}$ = 2.76 TeV at the LHC”. In: *Eur. Phys. J. C* 77.10 (2017), p. 658. doi: `10.1140/epjc/s10052-017-5222-x`. arXiv: `1707.07304 [nucl-ex]`.

[27] Gerhard Ecker. “Quantum chromodynamics”. In: *2005 European School of High-Energy Physics*. Apr. 2006. arXiv: `hep-ph/0604165`.

[28] Frank Wilczek. “Asymptotic freedom: From paradox to paradigm”. In: *Proc. Nat. Acad. Sci.* 102 (2005), pp. 8403–8413. doi: `10.1103/RevModPhys.77.857`. arXiv: `hep-ph/0502113`.

[29] Siegfried Bethke. “World Summary of alpha(s) (2011)”. In: *Nucl. Phys. B Proc. Suppl.* 222-224 (2012). Ed. by Guenter Grindhammer et al., pp. 94–100. doi: `10.1016/j.nuclphysbps.2012.03.010`.

[30] George Chapline and Michael Nauenberg. “Asymptotic Freedom and the Baryon-Quark Phase Transition”. In: *Phys. Rev. D* 16 (1977), p. 450. doi: `10.1103/PhysRevD.16.450`.

[31] R. Machleidt and D. R. Entem. “Chiral effective field theory and nuclear forces”. In: *Phys. Rept.* 503 (2011), pp. 1–75. doi: `10.1016/j.physrep.2011.02.001`. arXiv: `1105.2919 [nucl-th]`.

[32] Dean Lee. “Lattice simulations for few- and many-body systems”. In: *Prog. Part. Nucl. Phys.* 63 (2009), pp. 117–154. doi: `10.1016/j.ppnp.2008.12.001`. arXiv: `0804.3501 [nucl-th]`.

[33] K. S. Krane. *Introductory Nuclear Physics*. John Wiley & Sons, 1991.

[34] Peter J. Mohr, David B. Newell, and Barry N. Taylor. “CODATA Recommended Values of the Fundamental Physical Constants: 2014”. In: *Rev. Mod. Phys.* 88.3 (2016), p. 035009. doi: `10.1103/RevModPhys.88.035009`. arXiv: `1507.07956 [physics.atom-ph]`.

[35] Robert B. Wiringa, V. G. J. Stoks, and R. Schiavilla. "An Accurate nucleon-nucleon potential with charge independence breaking". In: *Phys. Rev. C* 51 (1995), pp. 38–51. doi: `10.1103/PhysRevC.51.38`. arXiv: `nucl-th/9408016`.

[36] Shreyasi Acharya et al. "The ALICE experiment: a journey through QCD". In: *Eur. Phys. J. C* 84.8 (2024), p. 813. doi: `10.1140/epjc/s10052-024-12935-y`. arXiv: `2211.04384 [nucl-ex]`.

[37] Jaroslav Adam et al. "Production of light nuclei and anti-nuclei in pp and Pb-Pb collisions at energies available at the CERN Large Hadron Collider". In: *Phys. Rev. C* 93.2 (2016), p. 024917. doi: `10.1103/PhysRevC.93.024917`. arXiv: `1506.08951 [nucl-ex]`.

[38] C. Van Der Leun and C. Alderliesten. "The deuteron binding energy". In: *Nucl. Phys. A* 380 (1982), pp. 261–269. doi: `10.1016/0375-9474(82)90105-1`.

[39] J. E. Purcell and C. G. Sheu. "Nuclear Data Sheets for A = 3". In: *Nucl. Data Sheets* 130 (2015), pp. 1–20. doi: `10.1016/j.nds.2015.11.001`.

[40] I. Angeli and K. P. Marinova. "Table of experimental nuclear ground state charge radii: An update". In: *Atom. Data Nucl. Data Tabl.* 99.1 (2013), pp. 69–95. doi: `10.1016/j.adt.2011.12.006`.

[41] Meng Wang et al. "The AME 2020 atomic mass evaluation (II). Tables, graphs and references". In: *Chin. Phys. C* 45.3 (2021), p. 030003. doi: `10.1088/1674-1137/abddaf`.

[42] Francesca Bellini and Alexander Philipp Kalweit. "Testing production scenarios for (anti-)(hyper-)nuclei and exotica at energies available at the CERN Large Hadron Collider". In: *Phys. Rev. C* 99.5 (2019), p. 054905. doi: `10.1103/PhysRevC.99.054905`. arXiv: `1807.05894 [hep-ph]`.

[43] Anton Andronic et al. "Decoding the phase structure of QCD via particle production at high energy". In: *Nature* 561.7723 (2018), pp. 321–330. doi: `10.1038/s41586-018-0491-6`. arXiv: `1710.09425 [nucl-th]`.

[44] Szabolcs Borsanyi et al. "QCD Crossover at Finite Chemical Potential from Lattice Simulations". In: *Phys. Rev. Lett.* 125.5 (2020), p. 052001. doi: `10.1103/PhysRevLett.125.052001`. arXiv: `2002.02821 [hep-lat]`.

[45] F. Becattini. "An Introduction to the Statistical Hadronization Model". In: *International School on Quark-Gluon Plasma and Heavy Ion Collisions: past, present, future*. Jan. 2009. arXiv: `0901.3643 [hep-ph]`.

[46] R. Hagedorn. "Statistical thermodynamics of strong interactions at high-energies". In: *Nuovo Cim. Suppl.* 3 (1965), pp. 147–186.

[47] P. Braun-Munzinger et al. “Thermal equilibration and expansion in nucleus-nucleus collisions at the AGS”. In: *Phys. Lett. B* 344 (1995), pp. 43–48. doi: `10.1016/0370-2693(94)01534-J`. arXiv: `nucl-th/9410026`.

[48] G. E. Brown, J. Stachel, and G. M. Welke. “Pions from resonance decay in Brookhaven relativistic heavy ion collisions”. In: *Phys. Lett. B* 253 (1991), pp. 19–22. doi: `10.1016/0370-2693(91)91356-Z`.

[49] A. Bazavov et al. “Chiral crossover in QCD at zero and non-zero chemical potentials”. In: *Physics Letters B* 795 (2019), pp. 15–21. issn: 0370-2693. doi: `https://doi.org/10.1016/j.physletb.2019.05.013`. url: `https://www.sciencedirect.com/science/article/pii/S0370269319303223`.

[50] A. Bazavov et al. “Equation of state in (2+1)-flavor QCD”. In: *Phys. Rev. D* 90 (2014), p. 094503. doi: `10.1103/PhysRevD.90.094503`. arXiv: `1407.6387 [hep-lat]`.

[51] A. Andronic et al. “Production of light nuclei, hypernuclei and their antiparticles in relativistic nuclear collisions”. In: *Phys. Lett. B* 697 (2011), pp. 203–207. doi: `10.1016/j.physletb.2011.01.053`. arXiv: `1010.2995 [nucl-th]`.

[52] Shreyasi Acharya et al. “Measurements of Chemical Potentials in Pb-Pb Collisions at sNN=5.02 TeV”. In: *Phys. Rev. Lett.* 133.9 (2024), p. 092301. doi: `10.1103/PhysRevLett.133.092301`. arXiv: `2311.13332 [nucl-ex]`.

[53] Volodymyr Vovchenko, Benjamin Dönigus, and Horst Stoecker. “Multiplicity dependence of light nuclei production at LHC energies in the canonical statistical model”. In: *Phys. Lett. B* 785 (2018), pp. 171–174. doi: `10.1016/j.physletb.2018.08.041`. arXiv: `1808.05245 [hep-ph]`.

[54] Vytautas Vislavicius and Alexander Kalweit. “Multiplicity dependence of light flavour hadron production at LHC energies in the strangeness canonical suppression picture”. In: (Oct. 2016). arXiv: `1610.03001 [nucl-ex]`.

[55] Natasha Sharma et al. “Light-nuclei production in pp and pA collisions in the baryon canonical ensemble approach”. In: *Phys. Rev. C* 107.5 (2023), p. 054903. doi: `10.1103/PhysRevC.107.054903`. arXiv: `2210.15617 [nucl-th]`.

[56] Jean Cleymans et al. “Multiplicity dependence of (multi)strange baryons in the canonical ensemble with phase shift corrections”. In: *Phys. Rev. C* 103.1 (2021), p. 014904. doi: `10.1103/PhysRevC.103.014904`. arXiv: `2009.04844 [hep-ph]`.

[57] Volodymyr Vovchenko and Horst Stoecker. “Thermal-FIST: A package for heavy-ion collisions and hadronic equation of state”. In: *Comput. Phys. Commun.* 244 (2019), pp. 295–310. doi: `10.1016/j.cpc.2019.06.024`. arXiv: `1901.05249 [nucl-th]`.

[58] Volodymyr Vovchenko, Benjamin Dönigus, and Horst Stoecker. “Canonical statistical model analysis of p-p , p -Pb, and Pb-Pb collisions at energies available at the CERN Large Hadron Collider”. In: *Phys. Rev. C* 100.5 (2019), p. 054906. doi: `10.1103/PhysRevC.100.054906`. arXiv: `1906.03145 [hep-ph]`.

[59] P. Koch, Berndt Muller, and Johann Rafelski. “Strangeness in Relativistic Heavy Ion Collisions”. In: *Phys. Rept.* 142 (1986), pp. 167–262. doi: `10.1016/0370-1573(86)90096-7`.

[60] Johann Rafelski. “Strange anti-baryons from quark-gluon plasma”. In: *Physics Letters B* 262.2 (1991), pp. 333–340. issn: 0370-2693. doi: `https://doi.org/10.1016/0370-2693(91)91576-H`. url: `https://www.sciencedirect.com/science/article/pii/037026939191576H`.

[61] S. T. Butler and C. A. Pearson. “Deuterons from High-Energy Proton Bombardment of Matter”. In: *Phys. Rev.* 129 (1963), pp. 836–842. doi: `10.1103/PhysRev.129.836`.

[62] Joseph I. Kapusta. “Mechanisms for deuteron production in relativistic nuclear collisions”. In: *Phys. Rev. C* 21 (1980), pp. 1301–1310. doi: `10.1103/PhysRevC.21.1301`.

[63] Rudiger Scheibl and Ulrich W. Heinz. “Coalescence and flow in ultrarelativistic heavy ion collisions”. In: *Phys. Rev. C* 59 (1999), pp. 1585–1602. doi: `10.1103/PhysRevC.59.1585`. arXiv: `nucl-th/9809092`.

[64] Stanislaw Mrowczynski. “Production of light nuclei at colliders – coalescence vs. thermal model”. In: *Eur. Phys. J. ST* 229.22-23 (2020), pp. 3559–3583. doi: `10.1140/epjst/e2020-000067-0`. arXiv: `2004.07029 [nucl-th]`.

[65] M. Kachelriess, S. Ostapchenko, and J. Tjemsland. “On nuclear coalescence in small interacting systems”. In: *Eur. Phys. J. A* 57.5 (2021), p. 167. doi: `10.1140/epja/s10050-021-00469-w`. arXiv: `2012.04352 [hep-ph]`.

[66] A. Aktas et al. “Measurement of anti-deuteron photoproduction and a search for heavy stable charged particles at HERA”. In: *Eur. Phys. J. C* 36 (2004), pp. 413–423. doi: `10.1140/epjc/s2004-01978-x`. arXiv: `hep-ex/0403056`.

[67] S. Chekanov et al. “Measurement of (anti)deuteron and (anti)proton production in DIS at HERA”. In: *Nucl. Phys. B* 786 (2007), pp. 181–205. doi: `10.1016/j.nuclphysb.2007.06.022`. arXiv: `0705.3770 [hep-ex]`.

[68] S. Nagamiya et al. “Production of Pions and Light Fragments at Large Angles in High-Energy Nuclear Collisions”. In: *Phys. Rev. C* 24 (1981), pp. 971–1009. doi: `10.1103/PhysRevC.24.971`.

[69] Shreyasi Acharya et al. “Measurement of deuteron spectra and elliptic flow in Pb–Pb collisions at $\sqrt{s_{\mathrm{NN}}}$ = 2.76 TeV at the LHC”. In: *Eur. Phys. J. C* 77.10 (2017), p. 658. doi: `10.1140/epjc/s10052-017-5222-x`. arXiv: `1707.07304 [nucl-ex]`.

[70] Francesca Bellini et al. “Examination of coalescence as the origin of nuclei in hadronic collisions”. In: *Phys. Rev. C* 103.1 (2021), p. 014907. doi: `10.1103/PhysRevC.103.014907`. arXiv: `2007.01750 [nucl-th]`.

[71] Kfir Blum et al. “Cosmic rays, antihelium, and an old navy spotlight”. In: *Phys. Rev. D* 96.10 (2017), p. 103021. doi: `10.1103/PhysRevD.96.103021`. arXiv: `1704.05431 [astro-ph.HE]`.

[72] Jaroslav Adam et al. “Centrality dependence of pion freeze-out radii in Pb-Pb collisions at $\sqrt{s}_{NN} =$ 2.76 TeV”. In: *Phys. Rev. C* 93.2 (2016), p. 024905. doi: `10.1103/PhysRevC.93.024905`. arXiv: `1507.06842 [nucl-ex]`.

[73] Shreyasi Acharya et al. “Measurement of the production of (anti)nuclei in p–Pb collisions at sNN=8.16TeV”. In: *Phys. Lett. B* 846 (2023), p. 137795. doi: `10.1016/j.physletb.2023.137795`. arXiv: `2212.04777 [nucl-ex]`.

[74] Małgorzata Anna Janik. “Overview of recent femtoscopy measurements with ALICE”. In: *13th Workshop on Particle Correlations and Femtoscopy*. Nov. 2018. arXiv: `1811.02828 [hep-ex]`.

[75] Michael Annan Lisa et al. “Femtoscopy in relativistic heavy ion collisions”. In: *Ann. Rev. Nucl. Part. Sci.* 55 (2005), pp. 357–402. doi: `10.1146/annurev.nucl.55.090704.151533`. arXiv: `nucl-ex/0505014`.

[76] S. Pratt. “Pion Interferometry of Quark-Gluon Plasma”. In: *Phys. Rev. D* 33 (1986), pp. 1314–1327. doi: `10.1103/PhysRevD.33.1314`.

[77] Kenji Morita et al. “Probing $\Omega\Omega$ and $p\Omega$ dibaryons with femtoscopic correlations in relativistic heavy-ion collisions”. In: *Phys. Rev. C* 101.1 (2020), p. 015201. doi: `10.1103/PhysRevC.101.015201`. arXiv: `1908.05414 [nucl-th]`.

[78] L. Fabbietti, V. Mantovani Sarti, and O. Vazquez Doce. “Study of the Strong Interaction Among Hadrons with Correlations at the LHC”. In: *Ann. Rev. Nucl. Part. Sci.* 71 (2021), pp. 377–402. doi: `10.1146/annurev-nucl-102419-034438`. arXiv: `2012.09806 [nucl-ex]`.

[79] Shreyasi Acharya et al. “p-p, p-Λ and Λ-Λ correlations studied via femtoscopy in pp reactions at $\sqrt{s}$ = 7 TeV”. In: *Phys. Rev. C* 99.2 (2019), p. 024001. doi: `10.1103/PhysRevC.99.024001`. arXiv: `1805.12455 [nucl-ex]`.

[80] Michael Annan Lisa and Scott Pratt. “Femtoscopically Probing the Freeze-out Configuration in Heavy Ion Collisions”. In: *Relativistic Heavy Ion Physics*. Ed. by R. Stock. 2010. doi: `10.1007/978-3-642-01539-7_21`. arXiv: `0811.1352 [nucl-ex]`.

[81] Shreyasi Acharya et al. “Search for a common baryon source in high-multiplicity pp collisions at the LHC”. In: *Phys. Lett. B* 811 (2020). [Erratum: Phys.Lett.B 861, 139233 (2025)], p. 135849. doi: `10.1016/j.physletb.2020.135849`. arXiv: `2004.08018 [nucl-ex]`.

[82] D. L. Mihaylov et al. “A femtoscopic Correlation Analysis Tool using the Schrödinger equation (CATS)”. In: *Eur. Phys. J. C* 78.5 (2018), p. 394. doi: `10.1140/epjc/s10052-018-5859-0`. arXiv: `1802.08481 [hep-ph]`.

[83] Henk Polinder, Johann Haidenbauer, and Ulf-G. Meissner. “Hyperon-nucleon interactions: A Chiral effective field theory approach”. In: *Nucl. Phys. A* 779 (2006), pp. 244–266. doi: `10.1016/j.nuclphysa.2006.09.006`. arXiv: `nucl-th/0605050`.

[84] J. Haidenbauer, U. G. Meißner, and A. Nogga. “Hyperon–nucleon interaction within chiral effective field theory revisited”. In: *Eur. Phys. J. A* 56.3 (2020), p. 91. doi: `10.1140/epja/s10050-020-00100-4`. arXiv: `1906.11681 [nucl-th]`.

[85] Michael Korsmeier, Fiorenza Donato, and Nicolao Fornengo. “Prospects to verify a possible dark matter hint in cosmic antiprotons with antideuterons and antihelium”. In: *Phys. Rev. D* 97.10 (2018), p. 103011. doi: `10.1103/PhysRevD.97.103011`. arXiv: `1711.08465 [astro-ph.HE]`.

[86] Mattia Di Mauro et al. “Nailing Down the Theoretical Uncertainties of D^{-} Spectrum Produced from Dark Matter”. In: *Phys. Rev. Lett.* 135.13 (2025), p. 131002. doi: `10.1103/w6n5-vs4d`. arXiv: `2411.04815 [astro-ph.HE]`.

[87] Shreyasi Acharya et al. “Multiplicity dependence of (anti-)deuteron production in pp collisions at $\sqrt{s}$ = 7 TeV”. In: *Phys. Lett. B* 794 (2019), pp. 50–63. doi: `10.1016/j.physletb.2019.05.028`. arXiv: `1902.09290 [nucl-ex]`.

[88] Shreyasi Acharya et al. “Multiplicity dependence of light (anti-)nuclei production in p-Pb collisions at $\sqrt{s_{NN}}$ = 5.02 TeV”. In: *Phys. Lett. B* 800 (2020), p. 135043. doi: `10.1016/j.physletb.2019.135043`. arXiv: `1906.03136 [nucl-ex]`.

[89] Shreyasi Acharya et al. “Production of light (anti)nuclei in pp collisions at $\sqrt{s} = 5.02$ TeV”. In: *Eur. Phys. J. C* 82.4 (2022), p. 289. doi: `10.1140/epjc/s10052-022-10241-z`. arXiv: `2112.00610 [nucl-ex]`.

[90] S. Schael et al. “Deuteron and anti-deuteron production in e+ e- collisions at the Z resonance”. In: *Phys. Lett. B* 639 (2006), pp. 192–201. doi: `10.1016/j.physletb.2006.06.043`. arXiv: `hep-ex/0604023`.

[91] R. Abdul Khalek et al. “Snowmass 2021 White Paper: Electron Ion Collider for High Energy Physics”. In: (Mar. 2022). arXiv: `2203.13199 [hep-ph]`.

[92] K. Aamodt et al. “The ALICE experiment at the CERN LHC”. In: *JINST* 3 (2008), S08002. doi: `10.1088/1748-0221/3/08/S08002`.

[93] B Abelev et al. “Upgrade of the ALICE Experiment: Letter Of Intent”. In: *J. Phys. G* 41 (2014), p. 087001. doi: `10.1088/0954-3899/41/8/087001`.

[94] Shreyasi Acharya et al. “ALICE upgrades during the LHC Long Shutdown 2”. In: *JINST* 19.05 (2024), P05062. doi: `10.1088/1748-0221/19/05/P05062`. arXiv: `2302.01238 [physics.ins-det]`.

[95] Ibrahim Jaser Abualrob et al. “Time resolution of the ALICE Time-Of-Flight detector with the first Run 3 pp collisions at $\sqrt{\mathrm{s}} = 13.6\,\mathrm{TeV}$”. In: (Nov. 2025). arXiv: `2511.10311 [physics.ins-det]`.

[96] Andrea Rossi. “Alice Alignment, Tracking and Physics Performance Results”. In: *PoS* VERTEX2010 (2010), p. 017. doi: `10.22323/1.113.0017`. arXiv: `1101.3491 [physics.ins-det]`.

[97] M. De Palma et al. *ALEPH: Technical Report 1983*. Tech. rep. CERN-LEPC-83-2, LEPC-P1. Apr. 1983.

[98] Uwe Holm. “The ZEUS detector: Status report 1993”. In: (Feb. 1993). doi: `10.3204/PUBDB-2017-12635`.

[99] R. Abdul Khalek et al. “Science Requirements and Detector Concepts for the Electron-Ion Collider: EIC Yellow Report”. In: *Nucl. Phys. A* 1026 (2022), p. 122447. doi: `10.1016/j.nuclphysa.2022.122447`. arXiv: `2103.05419 [physics.ins-det]`.

[100] Luisa Rosa Maria Occhiuto et al. “The dRICH detector at the future ePIC experiment”. In: *PoS* EPS-HEP2025 (2026), p. 513. doi: `10.22323/1.485.0513`.

[101] P. von Doetinchem et al. “Cosmic-ray antinuclei as messengers of new physics: status and outlook for the new decade”. In: *JCAP* 08 (2020), p. 035. doi: `10.1088/1475-7516/2020/08/035`. arXiv: `2002.04163 [astro-ph.HE]`.

[102] Andrew W. Strong, Igor V. Moskalenko, and Vladimir S. Ptuskin. “Cosmic-ray propagation and interactions in the Galaxy”. In: *Ann. Rev. Nucl. Part. Sci.* 57 (2007), pp. 285–327. doi: `10.1146/annurev.nucl.57.090506.123011`. arXiv: `astro-ph/0701517`.

[103] Marius Potgieter. “Solar Modulation of Cosmic Rays”. In: *Living Rev. Solar Phys.* 10 (2013), p. 3. doi: `10.12942/lrsp-2013-3`. arXiv: `1306.4421 [physics.space-ph]`.

[104] N. Fornengo, L. Maccione, and A. Vittino. “Dark matter searches with cosmic antideuterons: status and perspectives”. In: *JCAP* 09 (2013), p. 031. doi: `10.1088/1475-7516/2013/09/031`. arXiv: `1306.4171 [hep-ph]`.

[105] K. Sakai et al. “Search for Antideuterons of Cosmic Origin Using the BESS-Polar II Magnetic-Rigidity Spectrometer”. In: *Phys. Rev. Lett.* 132.13 (2024), p. 131001. doi: `10.1103/PhysRevLett.132.131001`.

[106] M. Aguilar et al. “The Alpha Magnetic Spectrometer (AMS) on the international space station: Part II — Results from the first seven years”. In: *Phys. Rept.* 894 (2021), pp. 1–116. doi: `10.1016/j.physrep.2020.09.003`.

[107] F. Nozzoli, F. Dimiccoli, and P. Zuccon. “Perspectives of dark matter indirect search with ADHD in space”. In: *J. Phys. Conf. Ser.* 1548.1 (2020), p. 012035. doi: `10.1088/1742-6596/1548/1/012035`.

[108] Rene A. Ong et al. “The GAPS Experiment to Search for Dark Matter using Low-energy Antimatter”. In: *PoS* ICRC2017 (2018), p. 914. doi: `10.22323/1.301.0914`. arXiv: `1710.00452 [astro-ph.IM]`.

[109] Maurizio Spurio. *Probes of Multimessenger Astrophysics. Charged cosmic rays, neutrinos, γ-rays and gravitational waves*. Astronomy and Astrophysics Library. Springer, 2018. isbn: 978-3-319-96853-7, 978-3-319-96854-4. doi: `10.1007/978-3-319-96854-4`.

[110] Annika H. G. Peter. “Dark Matter: A Brief Review”. In: *arXiv e-prints*, arXiv:1201.3942 (Jan. 2012), arXiv:1201.3942. doi: `10.48550/arXiv.1201.3942`. arXiv: `1201.3942 [astro-ph.CO]`.

[111] V. C. Rubin. “Dark matter in spiral galaxies”. In: *Scientific American* 248 (June 1983), pp. 96–106. doi: `10.1038/scientificamerican0683-96`.

[112] Leszek Roszkowski, Enrico Maria Sessolo, and Sebastian Trojanowski. “WIMP dark matter candidates and searches—current status and future prospects”. In: *Rept. Prog. Phys.* 81.6 (2018), p. 066201. doi: `10.1088/1361-6633/aab913`. arXiv: `1707.06277 [hep-ph]`.

[113] Andrey E. Egorov et al. “Dark matter searches by the planned gamma-ray telescope GAMMA-400”. In: *JCAP* 11 (2020), p. 049. doi: `10.1088/1475-7516/2020/11/049`. arXiv: `2005.09032 [astro-ph.HE]`.

[114] Deepak Kumar. “Search for dark matter produced in association with a Higgs boson decaying to a pair of bottom quarks in proton proton collisions at p s 13 TeV using CMS 2017 and 2018 data”. PhD thesis. Indian Institute of Science Bangalore, Centre for High Energy Physics, India, Bangalore, Indian Inst. Sci., 2023.

[115] E. Aprile et al. “The XENONnT dark matter experiment”. In: *Eur. Phys. J. C* 84.8 (2024), p. 784. doi: `10.1140/epjc/s10052-024-12982-5`. arXiv: `2402.10446 [physics.ins-det]`.

[116] S. W. Barwick et al. “Measurements of the cosmic ray positron fraction from 1-GeV to 50-GeV”. In: *Astrophys. J. Lett.* 482 (1997), pp. L191–L194. doi: `10.1086/310706`. arXiv: `astro-ph/9703192`.

[117] W. Menn et al. “The PAMELA space experiment”. In: *Adv. Space Res.* 51 (2013), pp. 209–218. doi: `10.1016/j.asr.2011.06.030`.

[118] Francesca R. Spada. “Antimatter and Dark Matter search in space with AMS-02”. In: *34th International Conference on High Energy Physics*. Oct. 2008. arXiv: `0810.3831 [hep-ex]`.

[119] C. Patrignani et al. “Review of Particle Physics”. In: *Chin. Phys. C* 40.10 (2016), p. 100001. doi: `10.1088/1674-1137/40/10/100001`.

[120] S. Orito et al. “Precision measurement of cosmic ray anti-proton spectrum”. In: *Phys. Rev. Lett.* 84 (2000), pp. 1078–1081. doi: `10.1103/PhysRevLett.84.1078`. arXiv: `astro-ph/9906426`.

[121] O. Adriani et al. “PAMELA results on the cosmic-ray antiproton flux from 60 MeV to 180 GeV in kinetic energy”. In: *Phys. Rev. Lett.* 105 (2010), p. 121101. doi: `10.1103/PhysRevLett.105.121101`. arXiv: `1007.0821 [astro-ph.HE]`.

[122] M. Aguilar et al. “Antiproton Flux, Antiproton-to-Proton Flux Ratio, and Properties of Elementary Particle Fluxes in Primary Cosmic Rays Measured with the Alpha Magnetic Spectrometer on the International Space Station”. In: *Phys. Rev. Lett.* 117.9 (2016), p. 091103. doi: `10.1103/PhysRevLett.117.091103`.

[123] K. Abe et al. “The results from BESS-Polar experiment”. In: *Adv. Space Res.* 60 (2017), pp. 806–814. doi: `10.1016/j.asr.2016.11.004`.

[124] Kenichi Sakai et al. “New result of Antideuteron search in BESS-Polar II”. In: *PoS* ICRC2021 (2021), p. 123. doi: `10.22323/1.395.0123`.

[125] T. et al. Bess-polar experiment Yoshida. “BESS-polar experiment”. In: *Advances in Space Research* 33.10 (Jan. 2004), pp. 1755–1762. doi: `10.1016/j.asr.2003.05.017`.

[126] M. Simon, A. Molnar, and S. Roesler. “A New Calculation of the Interstellar Secondary Cosmic-Ray Antiprotons”. In: *apj* 499.1 (May 1998), pp. 250–257. doi: `10.1086/305606`.

[127] Samuel J. Ting. *Latest Results from the AMS Experiment on the International Space Station*. CERN Colloquium. Invited talk, CERN, Geneva, Switzerland. 2018.

[128] M. Aguilar et al. "The Alpha Magnetic Spectrometer (AMS) on the International Space Station. I: Results from the test flight on the space shuttle". In: *Phys. Rept.* 366 (2002). [Erratum: Phys.Rept. 380, 97–98 (2003)], pp. 331–405. doi: `10.1016/S0370-1573(02)00013-3`.

[129] Luisa Arruda, Fernando Barao, and Rui Pereira. "Particle identification with the AMS-02 RICH detector: D/p and anti-D/anti-p separation". In: (Jan. 2008). arXiv: `0801.3243 [astro-ph]`.

[130] Maximilian Mahlein et al. "A realistic coalescence model for deuteron production". In: *Eur. Phys. J. C* 83.9 (2023), p. 804. doi: `10.1140/epjc/s10052-023-11972-3`. arXiv: `2302.12696 [hep-ex]`.

[131] Christian Bierlich et al. "A comprehensive guide to the physics and usage of PYTHIA 8.3". In: *SciPost Phys. Codeb.* 2022 (2022), p. 8. doi: `10.21468/SciPostPhysCodeb.8`. arXiv: `2203.11601 [hep-ph]`.

[132] Shreyasi Acharya et al. "Production of light-flavor hadrons in pp collisions at $\sqrt{s} = 7$ and $\sqrt{s} = 13$ TeV". In: *Eur. Phys. J. C* 81.3 (2021), p. 256. doi: `10.1140/epjc/s10052-020-08690-5`. arXiv: `2005.11120 [nucl-ex]`.

[133] S. Acharya et al. "(Anti-)deuteron production in pp collisions at $\sqrt{s} = 13$ TeV". In: *Eur. Phys. J. C* 80.9 (2020), p. 889. doi: `10.1140/epjc/s10052-020-8256-4`. arXiv: `2003.03184 [nucl-ex]`.

Acknowledgments

Il mio primo grande ringraziamento va alla Prof.ssa Bellini, non solo dal punto di vista accademico ma anche e soprattutto umano, per essere sempre stata disponibile ad aiutarmi, insegnarmi e guidarmi durante questo percorso. Un altro grande ringraziamento va al Dr. Francesco Noferini, con il quale mi sono trovato molto bene e che, con la sua guida, pazienza e supporto, è stato fondamentale durante tutto il lavoro di tesi. Vorrei ringraziare anche tutto il gruppo ALICE-ePIC Bologna per avermi accolto fin da subito e fatto sentire parte del gruppo. Il ringraziamento più importante va ai miei genitori, Daniela e Giorgio, che mi hanno sempre sostenuto e permesso di seguire la mia strada, a mio fratello Tommaso, alla Lella, allo zio Giuliano, alla nonna Renata, alla nonna Maria e a tutta la mia famiglia. Infine vorrei ringraziare tutti i miei amici, nuovi, vecchi e ritrovati: grazie per avermi sopportato e per aver reso speciali questi anni.